



Michigan Technological University
Create the Future Digital Commons @ Michigan Tech

Dissertations, Master's Theses and Master's
Reports - Open

Dissertations, Master's Theses and Master's
Reports

2011

Analytical investigation of squeeze film dampers

Mehmet Murat Altuğ Biçak
Michigan Technological University

Follow this and additional works at: <https://digitalcommons.mtu.edu/etds>



Part of the [Mechanical Engineering Commons](#)

Copyright 2011 Mehmet Murat Altuğ Biçak

Recommended Citation

Biçak, Mehmet Murat Altuğ, "Analytical investigation of squeeze film dampers", Dissertation, Michigan Technological University, 2011.

<https://doi.org/10.37099/mtu.dc.etds/351>

Follow this and additional works at: <https://digitalcommons.mtu.edu/etds>



Part of the [Mechanical Engineering Commons](#)

ANALYTICAL INVESTIGATION OF SQUEEZE FILM DAMPERS

By

MEHMET MURAT ALTUĞ BIÇAK

A DISSERTATION

Submitted in partial fulfillment of the requirements for the degree of

DOCTOR OF PHILOSOPHY

(Mechanical Engineering-Engineering Mechanics)

MICHIGAN TECHNOLOGICAL UNIVERSITY

2011

Copyright © Mehmet Murat Altuğ Bıçak 2011

This dissertation, "Analytical Investigation of Squeeze Film Dampers," is hereby approved in partial fulfillment of the requirements for the degree of DOCTOR OF PHILOSOPHY IN MECHANICAL ENGINEERING-ENGINEERING MECHANICS.

Department of Mechanical Engineering-Engineering Mechanics

Signatures:

Dissertation Advisor _____
Dr. Mohan D.Rao

Committee Member _____
Dr. Ossama Abdelkhalik

Committee Member _____
Dr. Chris E. Passerello

Committee Member _____
Dr. Jindong Tan

Department Chair _____
Dr. William Predebon

Date _____

To my parents

Niyazi, Fazilet Bıçak

Keşke bugünleri görebilseydin...

Contents

Dedication	iii
List of Figures	vii
List of Tables	ix
Preface	xi
Acknowledgments	xii
Nomenclature	xiii
Abstract	xvi
1 Introduction	1
2 Objective	7
3 Mathematical formulation of governing equations	8
3.1 Fluid modeling	8
3.1.1 Applicability of Reynolds equation	12
3.1.2 Extension of applicability considering viscothermal effects	14
3.1.3 Extension of applicability considering non-flat surfaces	15
3.2 Structure modeling	15
4 Linear analysis	18
4.1 Solution procedure	21
4.2 Exact solutions for simple cases	24
4.2.1 Rectangular plates	25
4.2.2 Skew plates	25
4.3 Solutions for complex geometries	27
4.3.1 Structure domain	28
4.3.2 Fluid domain	31

4.3.3	Coupled Eigenvalue problem	33
4.3.4	Simple cases and validation of FEA	36
4.3.5	Example : Condenser microphone with stationary backplate	39
5	Nonlinear analysis	43
5.1	Solution using Green's function	43
5.2	Calculation of squeeze film stiffness and damping	46
5.3	Examples	47
5.3.1	Exact solution for clamped boundary conditions (CCCC)	48
5.3.2	Case: CFCC	49
5.3.3	Case: FCFC and FSFS	50
5.3.4	Case: FFFC	51
5.3.5	Case: CFFC	51
5.4	Comparison of cases	52
5.4.1	Linear (First harmonic) comparisons	52
5.4.2	Nonlinear (Second harmonic) comparisons	56
6	Experimental investigation of SFD	60
6.1	Correlation of FEA model	61
6.2	Nonlinear region	64
6.3	SFD against viscoelastic treatments	66
7	Conclusions and future work	68
	Bibliography	71
A	Appendices	78
A.1	Exact solutions of coupled rectangular domain	78
A.1.1	CCCC	78
A.1.2	CCFC	79
A.1.3	CCFF	81
A.1.4	CFFF	83
A.1.5	CFCF	85
A.2	Gnu Octave Scripts	87
A.2.1	Fluid stiffness matrix \mathbf{K}_f calculation	87
A.2.2	Fluid mass matrix \mathbf{M}_f calculation	89

A.2.3	Fluid forcing matrix \mathbf{Q}_f calculation	90
A.2.4	Structural stiffness matrix \mathbf{K} calculation	91
A.2.5	Structural mass matrix \mathbf{M} calculation	93
A.2.6	Structural forcing matrix \mathbf{Q} calculation	94
A.2.7	Eigen solution of coupled problem	96
A.3	Second harmonic nonlinear solution	97
A.3.1	Case CCCC	97
A.3.2	Case CFCC	98
A.3.3	Case FCFC	99
A.3.4	Case FSFS	100
A.3.5	Case CFFC	101
A.3.6	Case FFFC	102
A.4	Thermal conductivities	104

List of Figures

1.1	Squeeze (left) and sucking (right) motion of the trapped fluid due to the oscillation of boundaries	4
4.1	Physical (a) and computational (b) domains	18
4.2	Real and imaginary parts of the first and second eigenvalues for the rectangular CCCC plate with Neumann fluid boundary conditions .	26
4.3	Plate and squeeze film fluid domain	27
4.4	Coupled field with forces	28
4.5	Kirchoff plate element geometry coupled with pressure field	29
4.6	Effect of the film thickness, the fluid viscosity and the ambient pressure	37
4.7	Frequency response function	39
4.8	Microphone backplate	40
4.9	Nondimensional real pressure distribution underneath the microphone diaphragm	41
4.10	Nondimensional imaginary pressure distribution underneath the microphone diaphragm	42
4.11	Frequency response of microphone diaphragm	42
5.1	Normalized spring force for different boundary conditions of a square plate. (a) constant uniform deflection obtained by Darling et al. [23], (b) present study.	53
5.2	Normalized damping force for different boundary conditions of a square plate. (a) constant uniform deflection obtained by Darling et al. [23], (b) present study.	54
5.3	Frequency shift (a) and damping ratio (b) for various boundary conditions of the square plate	55
5.4	The midpoint ($x, y = 0.5m$) absolute pressure variation	56
5.5	Total force acting to the plate for CCCC case, real part of $a_1 = Re(a_1)$ (a), imaginary part of $a_1 = Im(a_1)$ (b), $Re(a_2)$ (c), $Im(a_2)$ (d)	57
5.6	Total force acting to the plate for CFCC case, $Re(a_1)$ (a), $Im(a_1)$ (b), $Re(a_2)$ (c), $Im(a_2)$ (d)	58

5.7	Total force acting to the plate for FCFC case, $Re(a_1)$ (a), $Im(a_1)$ (b), $Re(a_2)$ (c), $Im(a_2)$ (d)	59
6.1	Reference problem experimental setup	60
6.2	Physical plate with welded attached plate	61
6.3	Comparison of frequency response functions	63
6.4	First (left), second modes (right) and normalized pressure distribution underneath the plate (p/p_a), where p_a : Ambient Pressure = 101325 N/m^2)	63
6.5	Experimental setup	64
6.6	Nonlinear response of the square plate exposed to sinusoidal excitation	65
6.7	Impact noise measurement testing	66
6.8	Comparison of SFD against viscoelastic damping treatments (Topleft: untreated plate, toprighth: viscoelastic film, bottomleft: viscoelastic damper, bottomright:SFD)	67
A.1	Real and imaginary parts of the first (left) and second (right) eigenvalues for the rectangular CCCC plate with Dirichlet fluid boundary conditions	79
A.2	Real and imaginary parts of the first and second eigenvalues for the rectangular CFCC plate	81
A.3	Real and imaginary parts of the first and second eigenvalues for the rectangular CCFF plate	83
A.4	Real and imaginary parts of the first and second eigenvalues for the rectangular CFFF plate	85
A.5	Real and imaginary parts of the first and second eigenvalues for the rectangular CFCF plate	87

List of Tables

3.1	Effective viscosity derivation functions by several studies	10
3.2	Knudsen number and the corresponding flow regimes	11
4.1	Selection of λ_m considering four possible boundary conditions . . .	22
4.2	Squeeze film eigenvalues with Neumann boundary conditions	23
4.3	Damped eigenvalues for the first mode of square CCCC plate with closed boundary conditions (Vacuum : 35.436)	24
4.4	Damped eigenvalues for the second mode of CCCC plate with closed boundary conditions (Vacuum:72.312)	25
4.5	Damped eigenvalues for the first mode of square CFCF plate ($\alpha = \pi/3$, Vacuum : 27.606)	26
4.6	Damped eigenvalues for the first mode of square CFCF plate ($\alpha = \pi/3$, Vacuum : 30.933)	27
4.7	Eigenfrequencies (Hz) of rectangular clamped plate on air film . . .	38
4.8	Natural frequencies (Hz) and damping ratios of clamped-free-free-free rectangular plate for various fluid film thicknesses	38
5.1	Mode Shapes	48
6.1	Comparison of simulation and experiment for corner and center supported SFD plate	62
A.1	Damped eigenvalues for the first mode of square CCCC plate with open boundary conditions (Vacuum : 35.436)	78
A.2	Damped eigenvalues for the second mode of CCCC plate with open boundary conditions (Vacuum:72.312)	78
A.3	Damped eigenvalues for the first mode of square CCFC plate with closed-closed-open-closed boundary conditions (Vacuum : 23.96) . .	80
A.4	Damped eigenvalues for the second mode of CCFC plate with closed-closed-open-closed boundary conditions (Vacuum:40.02)	80
A.5	Damped eigenvalues for the first mode of square CFCF plate with closed-open-closed-open boundary conditions (Vacuum : 22.223) . .	82
A.6	Damped eigenvalues for the second mode of square CFCF plate with closed-open-closed-open boundary conditions (Vacuum : 26.556) . .	82
A.7	Damped eigenvalues for the first mode of square CFFF plate with closed-open-open-open boundary conditions (Vacuum : 3.4864) . . .	84

A.8	Damped eigenvalues for the second mode of square FFFC plate with open-open-open-closed boundary conditions (Vacuum : 8.5443) . . .	84
A.9	Damped eigenvalues for the first mode of square CCFF plate (Vac- uum : 6.9365)	86
A.10	Damped eigenvalues for the second mode of square CCFF plate (Vacuum : 23.948)	86
A.11	Thermal conductivities of several materials	104

Preface

This dissertation is submitted for the degree of Doctor of Philosophy at the Michigan Technological University. The research described herein was conducted under the supervision of Professor Mohan D. Rao in the department of Mechanical Engineering-Engineering Mechanics, Michigan Technological University.

Part of this work has been presented in the following publications:

- M.M.A. Bicak and M.D. Rao, Analytical modeling of squeeze film damping for rectangular elastic plates using Green's functions, Journal of Sound and Vibration, Volume 329, Issue 22, 25 October 2010, Pages 4617-4633. (Principle investigator)
- M.M.A. Bicak and M.D. Rao, Coupled Squeeze Film Analysis by Reissner-Mindlin Plate Elements, Journal of Vibration and Control, 2010, *in press*. (Principle investigator)
- M.M.A. Bicak and M.D. Rao, Squeeze Film Damping of Fully Coupled Rectangular and Skew Plates, American Institute of Aeronautics and Astronautics Journal, *submitted*. (Principle investigator)

Acknowledgments

I would like to express my sincere gratitude to Professor Mohan D. Rao not only for his guidance and support throughout my studies, but also for his personal advice as a mentor. He believed in me the day I entered his office and in patiently saw through unproductive times with great understanding. Without his inspiration and direction, this work wouldn't be realized.

I would like to thank all my committee members Assistant Professor Ossama Abdelkhalik, Professor Chris E. Passerello and Associate Professor Jindong Tan for their advice and comments during my studies.

Many thanks to senior design team members, J. R. Makos, B. J. Mason, J. D. Myers, R. S. Prohaska and I. B. Soule who were involved in vibration and acoustical measurements.

I would like to thank my parents especially to my father for his encouragement, vision and right decisions that he made after my mother passed away. I would like to thank to my sister for her endless support and being a mentor when I need.

I would like to finally thank to my wife Burcu, for her patience and understanding. I would probably have spent more time on putting this work together without her support.

Nomenclature

α_r	Rate of momentum transfer rate from gas particles to the structure boundary walls due to the collision
β	Skewness angle
β_a	Aspect ratio which is defined as L_x/L_y
δ	Nondimensional deflection parameter.
γ	Ratio of specific heats
γ_{1-7}	Skewness related parameters
λ	Mean free path of molecules
λ_m	Fluid domain boundary characteristic orthogonal function in ξ direction
J	Jacobian matrix
K,M	Global stiffness and mass matrix of structural domain
m_e,k_e	Mass and stiffness matrix for quadrilateral structural plate element
Q	Fluid film-structure coupling forcing matrix for structural domain
μ	Dynamic viscosity of fluid
μ_{eff}	Effective viscosity
Ω	Nondimensional frequency
ω	Oscillation frequency of vibration
Ω_s	Structure domain
$\Phi(x,y)$	Deflection shape of the structure
ρ	Plate density
ρ_a	Ambient fluid density

ρ_f	Fluid density
σ	Squeeze number per unit area
θ	Structure domain boundary characteristic orthogonal polynomial in η direction
θ_x, θ_y	Rotation of structure around x and y axis
ϱ	Shear energy correction factor
ς	Function of Knudsen number used in calculation of effective viscosity
ϑ	Structure domain boundary characteristic orthogonal polynomial in ξ direction
ξ, η	Computational domain axes
ζ_n	Fluid domain boundary characteristic orthogonal function in η direction
$a_n(x, y)$	Nondimensional time invariant pressure for n^{th} harmonic
c_a	Ambient speed of sound in fluid
D	Flexural rigidity of the plate
E	Young's modulus
h	Fluid film thickness
h_0	Undisturbed constant film gap thickness
$h_i(x, y)$	Initial gap thickness function
h_t	Plate thickness
j	$\sqrt{-1}$
K_n	Knudsen number, ratio of the mean free path of molecules to the film thickness
L_x, L_y	Skew domain edge lengths in x and y directions

p	Pressure
P_a	Ambient pressure
q	Load distribution on the plate
Re^*	Modified Reynolds number
T_a	Ambient temperature
u	Transversal deflection of the plate
u_f	Fluid flow velocity
ν	Poisson's ratio
s	shear wave number

Abstract

Squeeze film damping effects naturally occur if structures are subjected to loading situations such that a very thin film of fluid is trapped within structural joints, interfaces, etc. An accurate estimate of squeeze film effects is important to predict the performance of dynamic structures.

Starting from linear Reynolds equation which governs the fluid behavior coupled with structure domain which is modeled by Kirchhoff plate equation, the effects of nondimensional parameters on the damped natural frequencies are presented using boundary characteristic orthogonal functions. For this purpose, the nondimensional coupled partial differential equations are obtained using Rayleigh-Ritz method and the weak formulation, are solved using polynomial and sinusoidal boundary characteristic orthogonal functions for structure and fluid domain respectively.

In order to implement present approach to the complex geometries, a two dimensional isoparametric coupled finite element is developed based on Reissner-Mindlin plate theory and linearized Reynolds equation. The coupling between fluid and structure is handled by considering the pressure forces and structural surface velocities on the boundaries. The effects of the driving parameters on the frequency response functions are investigated.

As the next logical step, an analytical method for solution of squeeze film damping based upon Green's function to the nonlinear Reynolds equation considering elastic plate is studied. This allows calculating modal damping and stiffness force rapidly for various boundary conditions. The nonlinear Reynolds equation is divided into multiple linear non-homogeneous Helmholtz equations, which then can be solvable using the presented approach. Approximate mode shapes of a rectangular elastic plate are used, enabling calculation of damping ratio and frequency shift as well as complex resistant pressure. Moreover, the theoretical results are correlated and compared with experimental results both in the literature and in-house experimental procedures including comparison against viscoelastic dampers.

1 Introduction

Damping is defined as any effect that reduces the amplitudes of vibration oscillations in an oscillatory system. Several types of damping present inherently in mechanical systems. These are

- Material internal damping
 - Thermoelastic [1]
 - Magnetoelastic [2]
 - Internal damping (Dislocation, relaxation of grain and point defect boundaries, thermal hysteresis, ferromagnetic hysteresis, deformation hysteresis, etc. [3])
- Structure - Structure interaction related damping at joint and interfaces (Coulomb friction [4], contact damping [5])
- Fluid - Structure interaction related damping
 - Flow related damping (Drag related damping, fluid flow related damping i.e. wind, etc.)
 - Acoustics related damping (Acoustoelastic effects [6], acoustical radiation effects [7])
- External damping mechanisms
 - Using passive dampers
 - * Unconstrained or constrained viscoelastic materials, viscosity related damping i.e. dash-pots, electric or magnetic field effects (Eddy Current [8], Electrical field [9], Magnetic effects [10])
 - Using active dampers
 - * Electro and magneto rheological dampers [11, 12]

The material internal damping results from microscopic and macroscopic processes which include many mechanisms such as thermoelasticity, magnetoelasticity, dislocation, cracks, hysteresis due to thermal, ferromagnetic and deformation effects. Relative motion of structures which have common points of contact or joints produces energy dissipation such as in Coulomb friction, sliding, interface and contact damping. Fluid - structure damping is caused by dynamic interactions of structure with surrounding fluid. For instance, a structure moving in a fluid is subjected to the drag forces or a structure with large surfaces which loses its energy by the acoustical radiation. External damping arises from mechanical energy dissipation due to opposite forces acting on the structure by magnetic or electric field effects. The contactless brake technology [13] based on Eddy current and magnetic fields is a good example to the external damping mechanism. Moreover, the external damping can be separated into two subsections as passive and active dampers. In active damper case, the damping is controlled externally (usually electronic devices) to achieve specific goal. Electro and magneto rheological dampers fall in this category and they're implemented in many commercial products such as in Audi A1 car [14]. Tuned mass dampers [15], are passive dampers that absorb energy at a certain frequency and make the attached structure stationary at this particular frequency. There are many types of the tuned mass dampers [16]. For example, tuned mass dampers which have variable resonant frequencies fall into active dampers category.

In order to reduce structural vibration or vibration based noise problem, passive damping treatment and design change are the ones considered first. The feedback from the customers usually drives the problem, because of the design change cost, the products vibration problem is handled using passive treatments usually, such as adding viscoelastic dampers, adding foam materials, etc. If the problem is caused by a particular frequency, it can also be solved using tuned mass dampers such as in helicopter blades, or tall buildings vibration suppression cases [17]. Let us consider a particular problem, such as vibration based noise problem of a machine which has large surfaces. Adding viscoelastic materials may be costly or impossible due to the operational environment property such as elevated temperature. Moreover, the design change is nearly impossible since the machine is already been in operation. Adding softer material for the resilient support can block the vibrations transmission through the floor, but can't help with the vibration of lateral surfaces.

The extra damping can be implemented by attaching a thin plate using welding or any other fastening procedure to the lateral surfaces with a small air gap. For the structures such as large automotive panels or in helicopter blades [18, 19], this technique is not only very efficient, but also absorbs the impact energy when collision takes place. Another important issue is to add particular materials to the trapped fluid, which also affects viscosity of the fluid. It is also possible to put viscoelastic or piezo materials for passive and active control of surface vibration.

Squeeze film damping (SFD) which is the topic of this dissertation occurs when a structure moves in close proximity to another surface, in effect alternately stretching and squeezing any fluid that may be present in the space between the moving structures. Reynolds published the squeeze film effect in his famous study [20] on lubrication. This effect was an important mechanism for the generation of pressure in a lubricating film together with the wedge effect. Surprisingly, he also mentioned the squeeze film effect on animal joints over 120 years ago. The squeezed fluid can act as a mass, spring and damper, having a significant effect on the dynamics of the oscillating structures. The primary goal of a fluid film damping system is to limit the vibration of a given structure by dissipating the energy to the fluid within the film. However, in micro-electromechanical (MEMS) and micro-opto-electromechanical systems, the SFD impacts the operating behavior such as in micro-switches, micro-sensors, micro-accelerometers, telescope mirrors [21], etc. From a vibrational point of view, the SFD is very useful and cost-effective solution to most vibration and vibration-caused noise reduction problems.

Let us consider two closely separated structures which are shown in Figure 1.1. If the structures A and B move relative to each other, the trapped fluid between these structures gets squeezed out. Conversely, the fluid is sucked into the gap if both structures move apart from each other in opposite directions. The increase (squeezing) and decrease (sucking) of fluid pressure, create a flow which removes the energy of structures. If the speed of the structure displacements is small i.e. frequency of oscillations is low, the fluid finds enough time to leak and fails to be compressed considerably. In other case, when the structure oscillates with a high frequency, the fluid fails to escape and gets compressed which can be depicted as a cushioning effect which is usually called load capacity of fluid films [22].

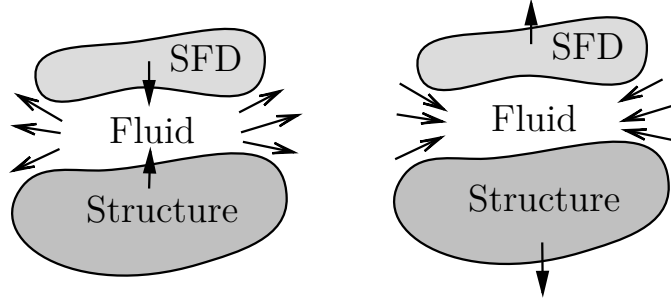


Figure 1.1: Squeeze (left) and sucking (right) motion of the trapped fluid due to the oscillation of boundaries

Extensive literature has already been developed for the SFD effect relating to fluid film lubrication [22] including compressibility, which has application in air bearing and levitation systems. The squeeze film analysis of the fluid is covered by three classes of models, the standard Helmholtz equation model, the low reduced frequency model and the Navier-Stokes model.

Darling et al. [23] used *Green's functions* to calculate stiffness and mass effects of the squeeze fluid film on a rigid plate based on the linearized Reynolds equation which is first studied by Langlois [22] to obtain damping and spring forces using a strip plate. The rigid movement approximation of the plate in the study of Darling et al. [23], is valid at frequencies which are well below the first natural frequency. However, the results of this study which facilitate the calculation of theoretical stiffness and damping forces is being used widely used [24, 25]. Starr [26] noticed the nonlinear effects based on amplitude from [27] and gave an approximate formula for the calculation of nonlinear damping force based on constant deformation of an oscillating plate. Bicak et al. [24] further calculated the linear and nonlinear stiffness and damping forces as well as frequency shifts and damping ratios considering the elastic motion of the plates. However, these studies considered one way coupling only i.e. the velocity of the rigid or elastic plate is applied as the forcing term to the linearized Reynolds equation.

Ingard et al. [28] used the wave equation approach under the small amplitude assumption. Using the wave equation and statistical energy analysis, Chow et al. [29] predicted the damping well above the critical frequency of the thick plate. However, the loss factor calculations for the statistical energy analysis are based

on the impedance approach which needs the pressure distribution to be calculated in advance.

Maidanik et al. [30] used the simplified Navier-Stokes equation approach with the incompressible fluid assumption. However, the validity of this assumption is restricted to very low frequencies. Onsay [31] and Fox et al. [32] developed fully coupled models including viscothermal effects. Beltman [6] considered viscothermal effects by the full linearized Navier-Stokes problem and low reduced frequency model and investigated a spherical resonator [33]. Basten et al. [34] applied the low reduced frequency solution of Beltman et al. [6] to calculate the acoustoelastic behavior of double-wall panels. Readers should refer to references [6] and [34] for an extensive literature review. Moreover, Beltman [33] developed a viscothermal acoustic finite element which models the effects of inertia, viscosity, compressibility and thermal conductivity. Akrouit et al. [35] applied this development to two laminated glass plates enclosing a thin viscothermal fluid cavity. Lei et al. [36] developed a three-dimensional viscous finite element model for the analysis of the acoustic fluid-structure interaction systems including the cochlear-based transducers which consists of a three-dimensional viscous acoustic fluid medium interacting with a two-dimensional flat structure domain. Karra et al. [37] used a modal approach to determine the vibro-acoustic system's response which shows the importance of the viscothermal effects in the case of thin fluid layers.

Full Navier-Stokes equations solutions are also studied by Mohite et al. [38], Pandey et al. [39], Gabriele et al. [40] for two dimensional structures whereas Lundblad et al. [41] and Ostasevicius et al. [42] studied Navier-Stokes equations with one dimensional structures. However, the main focus of these studies are the inertial and perforation effects of the structures only on the fluid domain which is considered as compressible. Other studies, such as Refs. [43, 44] approached to the squeeze film damping problem focusing on fluid domain only and thermal gradients within the fluid domain are included in the solution.

The present work presents a comprehensive analytical and experimental study of the SFD with entrapped fluid performed at the Michigan Technological University Noise and Modal Analysis laboratory. The topics are organized into several sections starting from fully coupled structure-fluid linear model for the prediction of the shifted and damped natural frequencies and mode shapes to nonlinear one

way coupled fluid-structure modeling . Section 4 provides an extensive analytical modeling of SFDs coupled with parallel skew plates. Several techniques, such as boundary characteristic orthogonal functions, Rayleigh-Ritz methods, etc. are used in this section. The main focus of section 4 is to predict and describe of the squeeze fluid film effect in fully coupled structure-fluid systems. In this section, several look-up tables and isopleth graphs which allows to predict natural frequency and mode shape of coupled systems, are presented considering many boundary configurations for both fluid and structural cases. As a step towards the modeling and predicting the operating behavior, section 4.3 describes the implementation of coupled finite element model to investigate the SFD effects on complex geometries. Moreover, the scripts needed to obtain finite element matrices are developed in GNU Octave [45] and presented in Appendix A.2 which could be later used by readers. The nonlinear one way coupled SFD damping effects are also investigated as a next logical step in Section 5. The harmonic solution of the nonlinear Reynolds equation is presented in this section. The general solution problem of the nonlinear Reynolds equation is divided into each harmonic subproblem. It is also shown that each harmonic problem is dependent upon the solutions of previous harmonics. Using the general solution of the Helmholtz equation, each harmonic solution can be found. Particular solutions of the non-homogeneous Helmholtz equation require the input mode shape which can be calculated using biharmonic plate problem. Moreover, damping ratio and frequency shift are calculated considering various types of boundary conditions. Based on these results, the optimum boundary condition configuration is found for maximum, minimum damping and frequency shifts.

As a step towards the predicting the performances of SFD, the experimental investigation and validation of both linear and nonlinear cases are presented in Section 6. The SFD performance is investigated based on air as the fluid. Moreover, the noise abatement of the SFDs attached on a casting finishing machine is also investigated. The performance of SFD is compared against many conventional damping systems in terms of noise reduction.

The final section 7 sums the conclusions from the each section of the present study and provides recommendations for further investigations.

2 Objective

The main objective of the present research is to identify and quantify the effects of squeeze film dampers on dynamical structures in linear and nonlinear regimes. Extensive analytical investigations are carried out for the calculation of SFD performances. Moreover, many look-up tables and isopleth plots are generated to determine the natural frequency and damping ratios of simple geometries rigorously. These tables include several different boundary condition cases. A coupled finite element model is developed based on a fully coupled finite element to investigate the SFD performances on complex geometries.

3 Mathematical formulation of governing equations¹

The governing mathematical equations are separated into fluid and structure parts. Step by step derivations are avoided since this generic derivations which are cited in the sections can be found in literature.

3.1 Fluid modeling

The fluid flow in a continuum regime is governed by the continuity equation and Navier-Stokes [46, 47] momentum equations which are valid for unsteady, compressible and viscous flow. For a small air-gap separating the two plates, the squeeze film flow is predominantly two dimensional (e.g., in the $x - y$ plane). Under following assumptions

- No external forces act on the film
- No inertial effects
- The structure oscillates with small amplitude and the main flow is driven by pressure gradients in the x and y directions.
- No slip flow occurs at the planar boundaries
- No variation of pressure across the fluid film
- The flow is laminar; no vortex flow and no turbulence occur anywhere in the film
- Fully developed flow is considered within the gap

¹The materials contained in this section partly and section 4.3 have been accepted for publication in Journal of Vibration and Control as M.M.A. Bicak and M.D. Rao, Coupled Squeeze Film Analysis by Reissner-Mindlin Plate Elements, Journal of Vibration and Control, 2010. The other materials contained in this section and linear analysis section 4 have been submitted to AIAA Journal as M.M.A. Bicak and M.D. Rao, Squeeze Film Damping of Fully Coupled Rectangular and Skew Plates, American Institute of Aeronautics and Astronautics Journal.

- Different assumptions can also be considerable for specific type of fluid. For air, flow is assumed to be isothermal, i.e. the pressure is proportional with the density

The nonlinear Reynolds equation [20] is

$$\nabla \left(\frac{ph^3}{12\mu} \nabla p \right) = \frac{\partial}{\partial t} (ph) \quad (3.1)$$

where ∇p is the gradient of the pressure, h is the thickness of the film, and μ is the fluid viscosity. The mean free path of the fluid concept gains more importance and can't be ignored at low ambient pressure or in very closely separated fluid films. In this case, molecular interaction forces on the thin film surfaces need to be taken into account. The fluid in continuum flow regime is governed by Navier-Stokes equations, whereas it's governed by Boltzmann transportation equation [48] in molecular flow regime. The regimes between these two regimes, both equations start to degenerate and fail to provide experimentally correlated results without modification and special treatments [49]. These modifications generally include tuning of the viscosity to fulfill specific requirements and it was first developed by Knudsen [50] in the early 1900s using the theory of rarefied gas flows. The effective viscosity is expressed using a simple fraction formula [51]

$$\mu_{eff} = \frac{\mu}{1 + \varsigma} \quad (3.2)$$

where ς is the function dependent on Knudsen number (K_n) defined as $K_n = \lambda/h$, where λ is the mean free path of molecules. The assumption of isothermal flow can't be hold in some cases. For instance, the energy is assumed to be transferred instantly to the bounding structure by molecular collisions of fluid. However, the dissipation of the excess energy inside fluid is proportional to the thermal conductivity ratio of the mediums. The thermal connectivity for several materials is presented in Table A.11. For example, if the coupled system consists the copper plate and air as the fluid, the isothermal assumption is valid since the ratio of thermal connectivity is very large. However, in rubber-air case, the ratio is around 6 which means the excess molecular energy in fluid will not be dissipated by the bounding structure as fast as in copper-air system.

Table 3.1
Effective viscosity derivation functions by several studies

Derived from	Ref.	ς function
Empirical equation based on experimental data	[50]	$\varsigma = \frac{K_n}{0.1474} \left(1 - \frac{0.588}{K_n + 3.095} \right)$
	[52]	$\varsigma = 6K_n(1 + K_n)$
	[53]	$\varsigma = \frac{K_n}{0.7}$
Navier-Stokes equations	[54]	$\varsigma = 6K_n$
	[55]	$\varsigma = K_n \left(\frac{12-6\alpha_r}{\alpha_r} + \frac{8}{3}K_n \right), 0 \leq \alpha_r \leq 1$
	[56]	$\varsigma = 6\alpha_r K_n$
Boltzmann transport equation	[57]	$\varsigma = \frac{6Q_f(\sqrt{\pi}/2K_n)}{\sqrt{\pi}/2K_n} - 1$
	[51]	$\varsigma = 9.638K_n^{1.159}$

There are several derivations of effective viscosity in the literature. Table 3.1 shows the effective viscosity function and the origin of the derivation.

where α_r is the rate of momentum transfer from gas particles to the structure walls due to the collision and Q_f function which is obtained by [57]. There are mainly three origins while obtaining ς function, using experimental curve fit, Navier-Stokes equations and Boltzmann transport equation. More information about the comparison of effective viscosity performances for each case can be found in Ref. [51].

The Reynolds equation is applicable only in the continuum flow regime which can be extended to cover other flow regimes using one of the effective viscosity calculations in Table 3.1, the relationship between the Knudsen number and flow regimes is shown at Table 3.2.

Under the assumption of harmonically varying gap thickness with the frequency of ω (rad/sec), the following equation is defined,

Table 3.2

Knudsen number and the corresponding flow regimes

Knudsen number (K_n)	Flow Regime
$K_n < 0.01$	Continuum
$0.01 < K_n < 0.1$	Slip
$0.1 < K_n < 10$	Transitional
$K_n > 10$	Molecular

$$h(x, y, t) = h_0 \left(1 + u(x, y) e^{j\omega t} \right) = h_0 \left(1 + \delta \Phi(x, y) e^{j\omega t} \right) \quad (3.3)$$

where h_0 is the undisturbed film thickness, Φ is the function of x, y which is the deflection shape of the structure and δ is a constant which is smaller than 1. Since equation (3.1) is nonlinear, harmonics of ω will appear in the pressure solution. So the pressure can be assumed as,

$$p(x, y, t) = P_a \left(1 + \sum_{n=1}^{\infty} a_n(x, y) e^{jn\omega t} \right) \quad (3.4)$$

where P_a is the ambient pressure and $a_n(x, y)$ is the coefficient for the n^{th} frequency, which is also complex.

If equations (3.3) and (3.4) are put into Eq. (3.1), it can be rewritten as,

$$\begin{aligned} \frac{\partial}{\partial x} \sum_{k=1}^{\infty} \sum_{n=k}^{\infty} \Upsilon \frac{\partial a_{n-k+1}}{\partial x} e^{jn\omega t} + \frac{\partial}{\partial y} \sum_{k=1}^{\infty} \sum_{n=k}^{\infty} \Upsilon \frac{\partial a_{n-k+1}}{\partial y} e^{jn\omega t} = \\ \frac{1}{\sigma} \sum_{n=1}^{\infty} nj\omega (a_n + a_{n-1} \delta \Phi) e^{jn\omega t} \end{aligned} \quad (3.5)$$

where

$$\Upsilon = a_{n-1} + 3\delta\Phi a_{n-2} + 3\delta^2\Phi^2 a_{n-3} + \delta^3\Phi^3 a_{n-4} \quad (3.6)$$

and

$$a_0 = 1, \quad a_n = 0 \quad \text{for } n < 0 \quad (3.7)$$

The first three harmonics of the Eq. (3.5) can be written as in equations (3.8)-(3.10) respectively as

$$\frac{\partial^2 a_1}{\partial x^2} + \frac{\partial^2 a_1}{\partial y^2} = j\sigma (a_1 + \delta\Phi) \quad (3.8)$$

$$\frac{\partial}{\partial x} \left[\frac{\partial a_2}{\partial x} + (a_1 + 3\delta\Phi) \frac{\partial a_1}{\partial x} \right] + \frac{\partial}{\partial y} \left[\frac{\partial a_2}{\partial y} + (a_1 + 3\delta\Phi) \frac{\partial a_1}{\partial y} \right] = 2j\sigma (a_2 + a_1\delta\Phi) \quad (3.9)$$

$$\begin{aligned} & \frac{\partial}{\partial x} \left[\frac{\partial a_3}{\partial x} + (3\delta\Phi + a_1) \frac{\partial a_2}{\partial x} + (3\delta^2\Phi^2 + a_1 3\delta\Phi + a_2) \frac{\partial a_1}{\partial x} \right] + \\ & \frac{\partial}{\partial y} \left[\frac{\partial a_3}{\partial y} + (3\delta\Phi + a_1) \frac{\partial a_2}{\partial y} + (3\delta^2\Phi^2 + a_1 3\delta\Phi + a_2) \frac{\partial a_1}{\partial y} \right] = \\ & 3j\sigma (a_3 + a_2\delta\Phi) \end{aligned} \quad (3.10)$$

where σ is the squeeze number per unit area,

$$\sigma = \frac{12\mu_{eff}\omega}{h_0^2 P_a} \quad (3.11)$$

In order to get squeeze number which is reported in the literature [25], [58], Eq. (3.11) should be multiplied by total area of the fluid domain area.

3.1.1 Applicability of Reynolds equation

The derivation of Reynolds equation which is first obtained by Langlois [22] in 1962 is based on Navier-Stokes equations and hydrodynamics equations. The modified Reynolds number which must be smaller than unity dictates the validity of the assumptions in the derivation of Reynolds equation.

The Reynolds equation is not valid for high frequencies since it is not including inertial terms. The measure of applicability of the Reynolds equation can be found

by comparing inertial forces with viscous forces per volume [59] which is named as the modified Reynolds Re^* in the literature,

$$Re^* = \frac{\text{inertial force}}{\text{viscous force}} = \frac{\rho_f u \left(\partial u_f / \partial n \right)}{\mu (\partial^2 u / \partial z^2)} \quad (3.12)$$

where u_f is the fluid flow velocity in the direction of n and ρ_f is the fluid density. Assuming the Poiseuille velocity profile along the gap and the direction n as the x axis, following formula can be obtained for the fluid flow velocity

$$u_f = \frac{hz (\partial p / \partial x)}{2\mu} \left(1 - \frac{z}{h} \right) \quad (3.13)$$

where z is the direction along the gap. Since the maximum absolute flow velocity will occur at the center along the gap, Eq. (3.12) will be reduced to

$$Re^* = \rho_f \frac{h^4}{64\mu^2} \left(\partial^2 p / \partial x^2 \right) \quad (3.14)$$

Considering the direction as y axis also, the total modified Reynolds number in both directions is,

$$Re^* = \rho_f \frac{h^4}{64\mu^2} \left(\frac{\partial^2 p}{\partial x^2} + \frac{\partial^2 p}{\partial y^2} \right) \quad (3.15)$$

Using Eq. (3.8), and dropping the dimensionless quantities, the previous equation turns into

$$Re^* = \rho_f \frac{h^4}{64\mu^2} \sigma \ll 1 \quad (3.16)$$

where σ is the squeeze number per unit area,

$$\sigma = \frac{12\mu_{eff}\omega}{h_0^2 P_a} \quad (3.17)$$

The modified Reynolds number Re^* should be smaller than unity for any point inside the fluid domain of interest. The modified Reynolds number formula considering the journal bearings can be found in Ref. [59].

3.1.2 Extension of applicability considering viscothermal effects

In order to extend the applicability of current approach, viscothermal effects should be included. In this case, the derivation of governing equations includes temperature and density distribution over the region [6] as,

$$\tilde{T} = T_a \left(1 + T(x, y, z) e^{j\omega t} \right) \quad (3.18)$$

$$\tilde{\rho} = \rho_a \left(1 + \rho(x, y, z) e^{j\omega t} \right) \quad (3.19)$$

Using these approximations together with ideal gas assumption for the fluid, Beltman [6] obtained the following nondimensional narrow gap equation

$$\nabla^2 p + \frac{\omega^2}{c_{eff}^2} p = -\frac{\rho_a \omega^2}{B(s)} u \quad (3.20)$$

where

$$c_{eff}^2 = \frac{c_a^2}{\gamma} B(s) n(s\sigma) \quad (3.21)$$

$$B(s) = 2 \left(\frac{1 - \cosh(s\sqrt{j})}{s\sqrt{j} \sinh(s\sqrt{j})} \right) + 1 \quad (3.22)$$

$$n(s\sigma) = \left(1 - \left(1 - \gamma^{-1} \right) B(s\sigma) \right)^{-1} \quad (3.23)$$

and c_a is the ambient speed of sound in the fluid, γ is the . Moreover, s is the shear wave number which is given as

$$s = h_0 \sqrt{\frac{\rho_a}{\mu}} \omega \quad (3.24)$$

Eq. (3.20) can be reduced to Reynolds equations for low values of the shear wave number.

3.1.3 Extension of applicability considering non-flat surfaces

Previously defined equations (3.8), (3.20) are derived considering flat parallel surfaces. However, in real physical system this assumption usually broken. In order to extend the applicability of present approach, the harmonically varying gap thickness assumption Eq. (3.3) should be revised such that

$$h(x, y, t) = h_0 \left(h_i(x, y) + u(x, y) e^{j\omega t} \right) \quad (3.25)$$

where $h_i = h_i(x, y)$ is the initial gap thickness. If Eq. (3.25) used instead of Eq. (3.3) in the derivation of Reynolds equation, the following modified Reynolds equation considering nonparallel gaps can be obtained,

$$h_i^2 \left(h_i \frac{d^2 p}{dx^2} + h_i \frac{d^2 p}{dy^2} + 3 \frac{dh_i}{dx} \frac{dp}{dx} + 3 \frac{dh_i}{dy} \frac{dp}{dy} \right) = j\sigma (h_i p + h) \quad (3.26)$$

Eq. (3.26) is a nonlinear partial differential equation which is more complicated than standard Reynolds equation (3.8).

3.2 Structure modeling

If a structure has one or two dimensions which are much smaller than other remaining dimensions, its dynamical behavior can be modeled using dimensionally reduced elasticity models. Otherwise, the structure should be modeled by three dimensional elasticity theory. The reduced elasticity models include two dimensional membrane, plate, shell theories as well as one dimensional beam, cable, and string theories. In present study, the structure of interest assumed to be modeled using two dimensional elasticity models. These models include Kirchhoff and Reissner-Mindlin plate theories.

The first model of thin plate bending was developed by Kirchhoff [60]. It is known as the Kirchhoff plate model which is an extension of Euler-Bernoulli beam theory to thin plates. Under following assumptions

- Thickness of the plate is small compared with plate's other dimensions

- Plate's undeformed mid-surface remain straight and normal to the deformed mid-surface after deformation
- Rotatory inertia effects are negligible.

Equation of motion for bending vibrations of a plate is given by

$$D\nabla^4 u(x, y, t) + \rho h_t \frac{\partial^2 u(x, y, t)}{\partial t^2} = q(x, y, t) \quad (3.27)$$

where u is the transversal deflection of the plate, $D = Eh_t^3/12(1 - v^2)$ is the flexural rigidity of the plate, E is Young's modulus, h_t is the plate thickness, v is Poisson's ratio, ρ is the density, q is the load distribution and $\nabla^4 = \nabla^2 \nabla^2$ is the biharmonic operator.

In Reissner-Mindlin plate theory [61, 62] which includes both bending and transverse shear deformations, the total kinetic (U_s) and potential (T_s) energy expressions for a plate is

$$U_s = \frac{1}{2} \int_{\Omega_s} \frac{h_t^3}{12} (\chi^T \mathbf{D}_b \chi) d\Omega_s + \frac{1}{2} \int_{\Omega_s} \varrho h_t (\gamma^T \mathbf{D}_s \gamma) d\Omega_s \quad (3.28)$$

$$T_s = \frac{1}{2} \int_{\Omega_s} h_t \rho \left(h_t \frac{\partial u}{\partial t} + \frac{h_t^3}{12} \frac{\partial \theta_x}{\partial t} + \frac{h_t^3}{12} \frac{\partial \theta_y}{\partial t} \right) d\Omega_s \quad (3.29)$$

with

$$\chi = \begin{bmatrix} -\partial \theta_y / \partial x \\ \partial \theta_x / \partial y \\ \partial \theta_x / \partial x - \partial \theta_y / \partial y \end{bmatrix} \quad \gamma = \begin{bmatrix} \theta_y + \partial u / \partial x \\ -\theta_x + \partial u / \partial y \end{bmatrix} \quad (3.30)$$

in which

$$\mathbf{D}_b = \frac{E}{1 - v^2} \begin{bmatrix} 1 & v & 0 \\ v & 1 & 0 \\ 0 & 0 & \frac{1-v}{2} \end{bmatrix} \quad \mathbf{D}_s = \frac{E}{2(1+v)} \begin{bmatrix} 1 & 0 \\ 0 & 1 \end{bmatrix} \quad (3.31)$$

is the constitutive equation for the plane stress and shear where Ω_s is the structure domain, θ_x and θ_y are the rotations around x and y axis respectively, ϱ is the shear energy correction factor which will be taken as 5/6 throughout the study. The derivation of structure related equations can be found in many textbooks [63].

4 Linear analysis

In this section, damped vibrations of Kirchhoff skew plates coupled with squeeze film fluid in linear regime are presented. The eigenvalue problem which is obtained by applying the weak formulation and Rayleigh-Ritz method for the coupled fluid structure systems [64], is solved using the boundary characteristic orthogonal polynomials (BCOPs) [65]. Many different cases are investigated based on the polynomial and sinusoidal types of BCOPs for structural and fluid domains respectively. Moreover, the isopleth plots based on the nondimensional parameters for several different cases are presented. For this purpose, a physical skew domain which is presented in Figure 4.1a is considered.

The physical skew domain which is presented in Figure 4.1, can be defined by three parameters L_x , L_y and β . A transformation is used to map the physical domain into a computational domain which is shown in Figure 4.1b as

$$x = L_x\xi + L_y\eta\cos\beta \quad (4.1)$$

$$y = L_y\eta\sin\beta \quad (4.2)$$

where ξ, η are the computational domain axes.

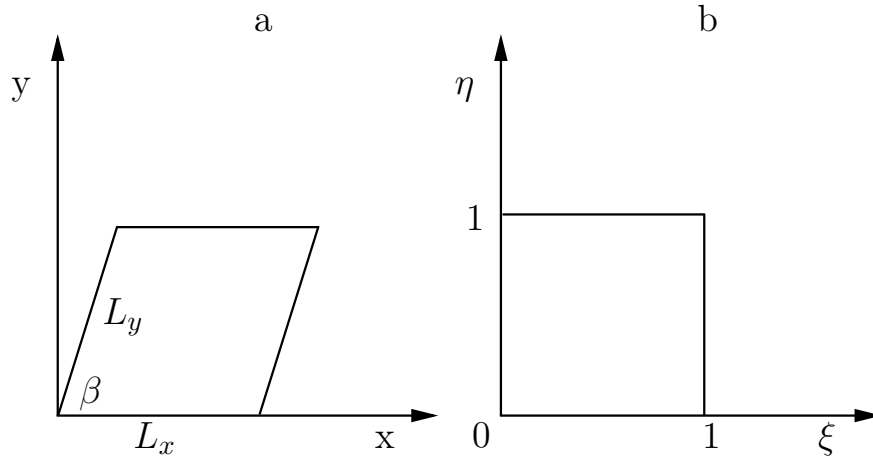


Figure 4.1: Physical (a) and computational (b) domains

Considering the following approximations,

$$u = \sum_i^n c_i \phi_i \quad (4.3)$$

$$q = \sum_i^m d_i \psi_i \quad (4.4)$$

which satisfy the following orthogonality conditions,

$$\int_0^1 \int_0^1 \phi_i \phi_j d\xi d\eta = \begin{cases} 1 & i = j \\ 0 & i \neq j \end{cases} \quad (4.5)$$

$$\int_0^1 \int_0^1 \psi_i \psi_j d\xi d\eta = \begin{cases} 1 & i = j \\ 0 & i \neq j \end{cases} \quad (4.6)$$

the following nondimensional equations can be obtained using Rayleigh-Ritz method in coupled fluid-structure systems [64] with weak formulation for fluid domain under homogeneous boundary conditions as,

$$\mathbf{K}\mathbf{s} - \Omega^2 \mathbf{M}\mathbf{s} = \epsilon \mathbf{G}\mathbf{f} \quad (4.7)$$

$$\mathbf{K}_f \mathbf{f} + j\kappa\Omega (\mathbf{M}_f \mathbf{f} + \mathbf{U}\mathbf{s}) = \mathbf{0} \quad (4.8)$$

where the nondimensional parameters are

$$\Omega = \omega L_x^2 \sqrt{\frac{\rho h}{D}} \quad (4.9)$$

$$\epsilon = \frac{P_a L_x^4}{h_0 D} \quad (4.10)$$

$$\kappa = \frac{12\mu_{eff}}{P_a h_0^2} \sqrt{\frac{D}{\rho h_t}} \quad (4.11)$$

and $\mathbf{s} = \{ c_1 \ c_2 \ \dots \ c_{n-1} \ c_n \}^T$, $\mathbf{f} = \{ d_1 \ d_2 \ \dots \ d_{m-1} \ d_m \}^T$.

The elements of \mathbf{K} , \mathbf{M} , \mathbf{G} , \mathbf{K}_f , \mathbf{M}_f and \mathbf{U} matrices can be obtained as

$$\begin{aligned} \mathbf{K}(i,j) = \int_0^1 \int_0^1 \left\{ \frac{\partial^2 \phi_i}{\partial \xi^2} \frac{\partial^2 \phi_j}{\partial \xi^2} + \gamma_1 \left(\frac{\partial^2 \phi_i}{\partial \xi \partial \eta} \frac{\partial^2 \phi_j}{\partial \xi^2} + \frac{\partial^2 \phi_i}{\partial \xi^2} \frac{\partial^2 \phi_j}{\partial \xi \partial \eta} \right) \right. \\ \left. + \gamma_2 \left(\frac{\partial^2 \phi_i}{\partial \eta^2} \frac{\partial^2 \phi_j}{\partial \xi^2} + \frac{\partial^2 \phi_i}{\partial \xi^2} \frac{\partial^2 \phi_j}{\partial \eta^2} \right) + \gamma_3 \frac{\partial^2 \phi_i}{\partial \xi \partial \eta} \frac{\partial^2 \phi_j}{\partial \xi \partial \eta} \right. \\ \left. + \gamma_4 \left(\frac{\partial^2 \phi_i}{\partial \eta^2} \frac{\partial^2 \phi_j}{\partial \xi \partial \eta} + \frac{\partial^2 \phi_i}{\partial \xi \partial \eta} \frac{\partial^2 \phi_j}{\partial \eta^2} \right) + \gamma_5 \frac{\partial^2 \phi_i}{\partial \eta^2} \frac{\partial^2 \phi_j}{\partial \eta^2} \right\} d\xi d\eta \quad (4.12) \end{aligned}$$

$$\mathbf{M}(i,j) = \int_0^1 \int_0^1 \phi_i \phi_j d\xi d\eta \quad (4.13)$$

$$\mathbf{G}(i,j) = \int_0^1 \int_0^1 \phi_i \psi_j d\xi d\eta \quad (4.14)$$

$$\mathbf{K}_f(i,j) = \int_0^1 \int_0^1 \left\{ \gamma_6 \psi_i \frac{\partial^2 \psi_j}{\partial \xi \partial \eta} + \gamma_7 \left(\frac{\partial \psi_i}{\partial \xi} \frac{\partial \psi_j}{\partial \xi} + \beta_a^2 \frac{\partial \psi_i}{\partial \eta} \frac{\partial \psi_j}{\partial \eta} \right) \right\} d\xi d\eta \quad (4.15)$$

$$\mathbf{M}_f(i,j) = \int_0^1 \int_0^1 \psi_i \psi_j d\xi d\eta \quad (4.16)$$

$$\mathbf{U}(i,j) = \int_0^1 \int_0^1 \psi_i \phi_j d\xi d\eta \quad (4.17)$$

where the skewness and aspect ratio related terms are

$$\begin{aligned} \gamma_1 &= -2\beta_a \cos \beta \\ \gamma_2 &= \beta_a^2 (v \sin^2 \beta + \cos^2 \beta) \\ \gamma_3 &= 2\beta_a^2 (1 + \cos^2 \beta - v \sin^2 \beta) \\ \gamma_4 &= -2\beta_a^3 \cos \beta \\ \gamma_5 &= \beta_a^4 \\ \gamma_6 &= 2\beta_a \cos \beta / \sin^2 \beta \\ \gamma_7 &= 1 / \sin^2 \beta \end{aligned} \quad (4.18)$$

and

$$\beta_a = \frac{L_x}{L_y} \quad (4.19)$$

4.1 Solution procedure

The structural approximation function ϕ can be selected as the well known boundary characteristic orthogonal polynomials [65, 66]. In this section, BCOPs have been used for determining the damped natural frequencies of the skew plate. More information about the BCOPs can be found in references [65, 67]. The BCOPs satisfy essential boundary conditions at the boundaries $(\xi, \eta = 0, 1)$. The properties of BCOPs can be listed as [67],

- They satisfy boundary conditions
- They are complete
- They don't violate the natural boundary conditions inherently.

The two dimensional BCOPs are expressed as the multiplication of one dimensional BCOPs as

$$\phi = \vartheta(\xi)\theta(\eta) \quad (4.20)$$

The recurrence relation for each direction can be obtained using Gram-Schmidt orthogonalization process [65] as,

$$\vartheta_{i+1}(\xi) = \{\xi - e_i\}\vartheta_i - e_{i-1}\vartheta_{i-1} \quad (4.21)$$

where

$$\vartheta_{-1} = 0 \quad (4.22)$$

Table 4.1

Selection of λ_m considering four possible boundary conditions

λ_m	$\psi(1, \eta) = 0$	$\frac{\partial \psi(1, \eta)}{\partial \xi} = 0$
$\psi(0, \eta) = 0$	$\sin(m\pi\xi)$	$\sin\left(\frac{2m-1}{2}\pi\xi\right)$
$\frac{\partial \psi(0, \eta)}{\partial \xi} = 0$	$\cos\left(\frac{2m-1}{2}\pi\xi\right)$	$\cos(m\pi\xi)$

$$e_m = \frac{\int_0^1 \xi \vartheta_m \vartheta_m d\xi}{\int_0^1 \vartheta_m \vartheta_m d\xi} \quad (4.23)$$

and

$$\vartheta_1 = \xi^a (1 - \xi)^b \quad (4.24)$$

The power coefficients a and b are determined considering boundary conditions for $\xi = 0$ and $\xi = 1$. For instance, selection of $a = 2$ will force the side $\xi = 0$ to be clamped, $a = 1$ to be simply supported and $a = 0$ to be free.

The fluid domain approximation function ψ is expressed as

$$\psi_i(\xi, \eta) = \lambda_m(\xi) \zeta_n(\eta) \quad (4.25)$$

The functions λ_m and ζ_n are selected to satisfy fluid domain Dirichlet or Neumann boundary conditions. Table 4.1 which can be used for ζ_n by interchanging ξ and m with η and n shows possible selection functions of λ_m .

After the construction of ϕ and ψ based on the boundary conditions of the problem, \mathbf{K} , \mathbf{M} , \mathbf{G} , \mathbf{K}_f , \mathbf{M}_f and \mathbf{U} matrices can be generated and Eqs. (4.7)-(4.8) can be written in matrix form as

$$\begin{bmatrix} \mathbf{K}_f + j\Omega\kappa\mathbf{M}_f & j\Omega\kappa\mathbf{U} \\ -\epsilon\mathbf{G} & \mathbf{K}_s - \Omega^2\mathbf{M}_s \end{bmatrix} \begin{Bmatrix} \mathbf{f} \\ \mathbf{s} \end{Bmatrix} = \begin{Bmatrix} \mathbf{0} \\ \mathbf{0} \end{Bmatrix} \quad (4.26)$$

or in compact form

$$\Upsilon \Phi = \mathbf{0} \quad (4.27)$$

The non-trivial solution of the equation is

$$\det(\Upsilon) = 0 \quad (4.28)$$

Using the determinant property of partitioned matrices, the determinant can be also expressed as

$$\det(\Upsilon) = \det(\mathbf{K}_f + j\Omega\kappa\mathbf{M}_f) \det\left(\mathbf{K}_s - \Omega^2\mathbf{M}_s + \epsilon\mathbf{G}(\mathbf{K}_f + j\Omega\kappa\mathbf{M}_f)^{-1}j\Omega\kappa\mathbf{U}\right) \quad (4.29)$$

if orthonormalized polynomials are used to construct \mathbf{s} and \mathbf{f} , Eq. (4.29) can be rewritten considering structure related natural frequencies as

$$\det\left(\mathbf{K}_s - \Omega^2\mathbf{I} + j\Omega\kappa\epsilon\mathbf{G}(\mathbf{K}_f + j\Omega\kappa\mathbf{I})^{-1}\mathbf{U}\right) = 0 \quad (4.30)$$

The solution of the problem i.e. obtaining the eigenvalues and eigenvectors, can be realized using Eq. (4.30) or generic eigenvalue problem based on the state space technique. However, due to the presence of fluid domain eigenvalues, the structure related eigenvalues can be close to fluid domain eigenvalues which would make the structure related eigenvalue extraction procedure difficult. In order to overcome this problem, Eq. (4.30) can be solved by using structure eigenvalues as the initial value for the root solution. In this case, few iterations would be enough to obtain complex eigenvalues.

Table 4.2
Squeeze film eigenvalues with Neumann boundary conditions

Mode No	Analytical[33]	Present study
1	$317.1 + 32.3j$	$317.2 + 32.34j$
2	$651.4 + 44.8j$	$651.8 + 44.79j$
3	$651.4 + 44.8j$	$651.9 + 44.91j$
4	$730.9 + 47.2j$	$731.4 + 47.28j$

4.2 Exact solutions for simple cases

The results are partitioned into two sections. In the first section, rectangular plates ($\beta = \pi/2$) with various boundary conditions are investigated. The effects of nondimensional ϵ and κ parameters on the eigenvalues are also presented. There are 21 possible combinations of boundary conditions for the rectangular ($\beta = \pi/2$) structural domain, whereas only 6 different boundary condition combinations exist for fluid domain. In this study, plates with only free and clamped boundary conditions are investigated, more cases including simply-supported boundary conditions can be found in Ref. [68]. The following results are obtained using Gnu Maxima [69] and Gnu Octave [45] software considering 7 BCOPs in each direction resulting 49 BCOPs for the plate and 49 fluid BCOPs in total. Gnu Maxima which is a descendant of a software developed at the Massachusetts Institute of Technology, can handle symbolic and numerical calculations.

In order to validate the fluid domain solution, the complex eigenvalues of the square fluid domain ($L_x = 0.5m$) with Neumann boundary conditions are calculated and compared in Table 4.2 against the analytical values obtained with the acousto-elastic theoretical results including viscothermal effects [33]. The results are in good agreement with the theoretical results.

Table 4.3
Damped eigenvalues for the first mode of square CCCC plate with closed
boundary conditions (Vacuum : 35.436)

$\log \epsilon \kappa$	$\log \kappa = -5$	-4	-3	-2
-5	35.99	35.99	35.99	35.99
-3	36.69	36.06	35.99	35.99
-1	71.41	42.31	36.69	36.06
1	$-0.06 \pm 101.74j$	$-0.06 \pm 98.33j$	$-0.05 \pm 71.41j$	$-0.03 \pm 42.31j$
2	$-0.63 \pm 102.07j$	$-0.63 \pm 101.74j$	$-0.63 \pm 98.33j$	$-0.49 \pm 71.43j$
3	$-6.29 \pm 101.99j$	$-6.29 \pm 101.97j$	$-6.29 \pm 101.65j$	$-6.29 \pm 98.33j$

Table 4.4

Damped eigenvalues for the second mode of CCCC plate with closed boundary conditions (Vacuum:72.312)

$\log \epsilon \kappa$	$\log \kappa = -5$	-4	-3	-2
-5	73.40	73.40	73.40	73.40
-3	73.40	73.40	73.40	73.40
-1	73.40	73.40	73.40	73.40
1	$-0.24 \pm 73.40j$	$-0.24 \pm 73.40j$	$-0.24 \pm 73.40j$	$-0.24 \pm 73.41j$
2	$-2.43 \pm 73.38j$	$-2.43 \pm 73.38j$	$-2.43 \pm 73.40j$	$-2.42 \pm 73.55j$
3	$-25.81 \pm 71.15j$	$-25.82 \pm 71.17j$	$-25.91 \pm 71.34j$	$-26.73 \pm 73.21j$

4.2.1 Rectangular plates

The structural boundary conditions for the plate edges are represented by four letters. For example, CFCF stands for Clamped-Free-Clamped-Free plate for left ($\xi = 0$), bottom ($\eta = 0$), right ($\xi = 1$) and upper edge ($\eta = 1$). Many different cases are investigated in this section, for the sake of integrity both isopleth graphs and tables are presented. To replicate the results Poisson ratio should be taken as 0.3.

The eigenvalues of the first two modes for the CCCC plate with closed fluid boundaries (Neumann) are presented at Tables 4.3-4.4, and the CCCC plate with open fluid boundaries (Dirichlet) are presented at Tables A.1-A.2 in Appendix A.1. The nondimensional resonant frequencies are also presented in the tables.

The other cases are presented at Tables A.3-A.4 for the CCFC case, Tables A.5-A.6 for the CFCF case, Tables A.7-A.8 for the CFFF case and Tables A.9-A.10 for the CCFF case. Moreover, the isopleth graphs of the CCCC with Neumann and Dirichlet boundary conditions, the CCFC case, the CFCF case, the CFFF case and the CCFF case are presented in Figure 4.2 and Figures, A.1, A.2, A.3, A.4 and A.5 in appendix respectively.

4.2.2 Skew plates

In this section, the first two damped eigenvalues of a skewed CFCF plate ($\alpha = \pi/3$) are examined at Tables 4.5-4.6 and respectively.

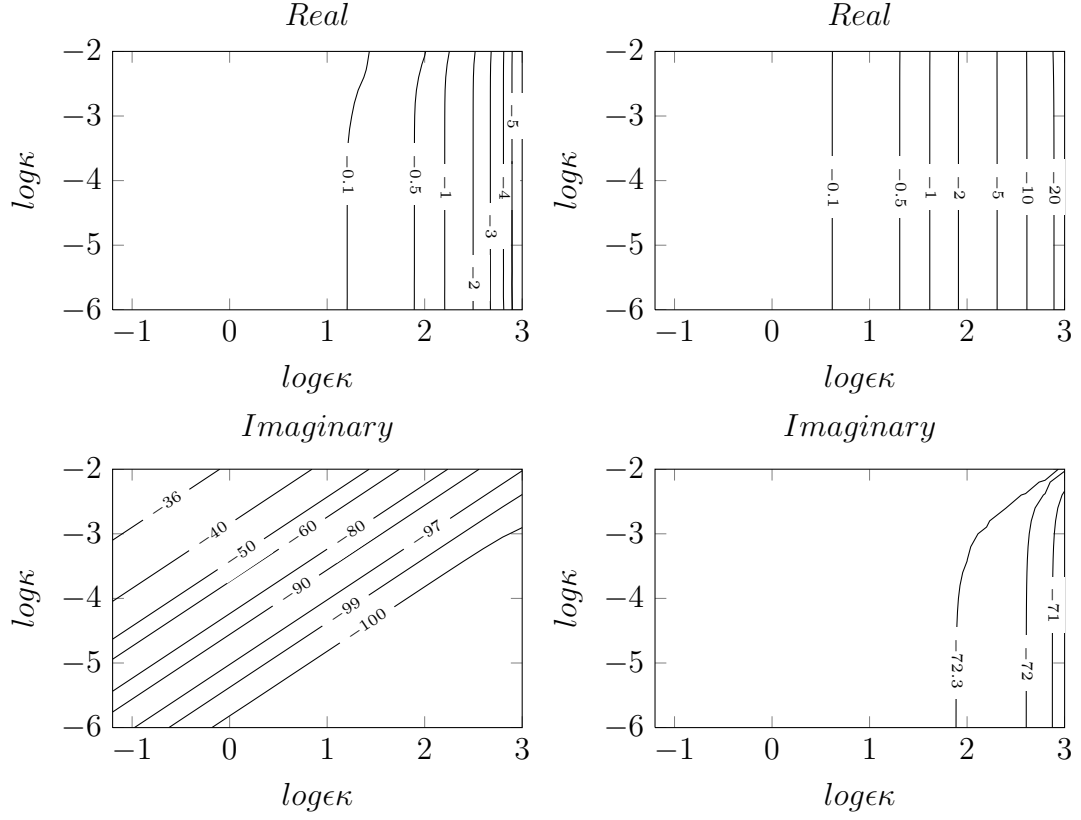


Figure 4.2: Real and imaginary parts of the first and second eigenvalues for the rectangular CCCC plate with Neumann fluid boundary conditions

Table 4.5

Damped eigenvalues for the first mode of square CFCF plate ($\alpha = \pi/3$, Vacuum : 27.606)

$\log \epsilon \kappa$	$\log \kappa = -5$	-4	-3	-2
-5	27.21	27.21	27.21	27.21
-3	27.21	27.21	27.21	27.21
-1	27.21	27.21	27.21	27.21
1	$-0.25 \pm 27.21j$	$-0.25 \pm 27.21j$	$-0.25 \pm 27.21j$	$-0.25 \pm 27.22j$
2	$-2.54 \pm 27.14j$	$-2.54 \pm 27.14j$	$-2.54 \pm 27.14j$	$-2.55 \pm 27.16j$
3	$-26.93 \pm 6.37j$	$-26.94 \pm 6.32j$	$-26.99 \pm 6.23j$	$-27.45 \pm 5.20j$

Table 4.6

Damped eigenvalues for the first mode of square CFCF plate ($\alpha = \pi/3$, Vacuum : 30.933)

$\log \epsilon \kappa$	$\log \kappa = -5$	-4	-3	-2
-5	30.04	30.04	30.04	30.04
-3	30.04	30.04	30.04	30.04
-1	30.04	30.04	30.04	30.04
1	$-0.07 \pm 30.04j$	$-0.07 \pm 30.04j$	$-0.07 \pm 30.04j$	$-0.07 \pm 30.04j$
2	$-0.65 \pm 29.99j$	$-0.65 \pm 29.99j$	$-0.65 \pm 29.99j$	$-0.65 \pm 29.99j$
3	$-5.67 \pm 29.29j$	$-5.67 \pm 29.29j$	$-5.67 \pm 29.29j$	$-5.68 \pm 29.30j$

4.3 Solutions for complex geometries

The results of the previous section can only be applicable to the simple geometries. As a step towards the predicting the dynamic behavior of SFD in rectangular and skew domains, the analytical investigation is further taken to cover complex geometries. For this case, the Reissner-Mindlin plate theory [61, 62] and Reynolds equation are used to develop a coupled finite element which has the capability of modeling coupled dynamic behavior of plates.

A typical plate - squeeze film system is presented in Figure 4.3. The base of the plate is treated as rigid. The fluid film pressure underneath the plate changes due to the surface oscillation of the plate causes fluid to be squeezed or sucked which in turn alters the plate oscillations and fluid film forces on the plate. The two way interaction forces are shown in Figure 4.4.

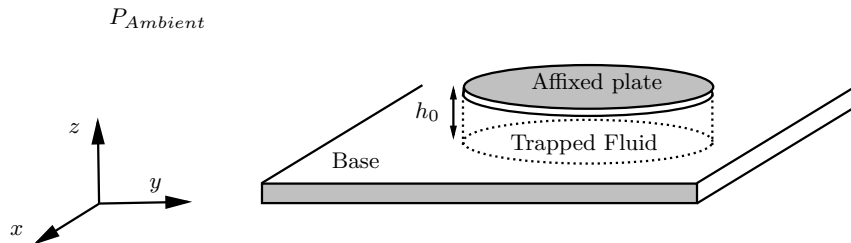


Figure 4.3: Plate and squeeze film fluid domain

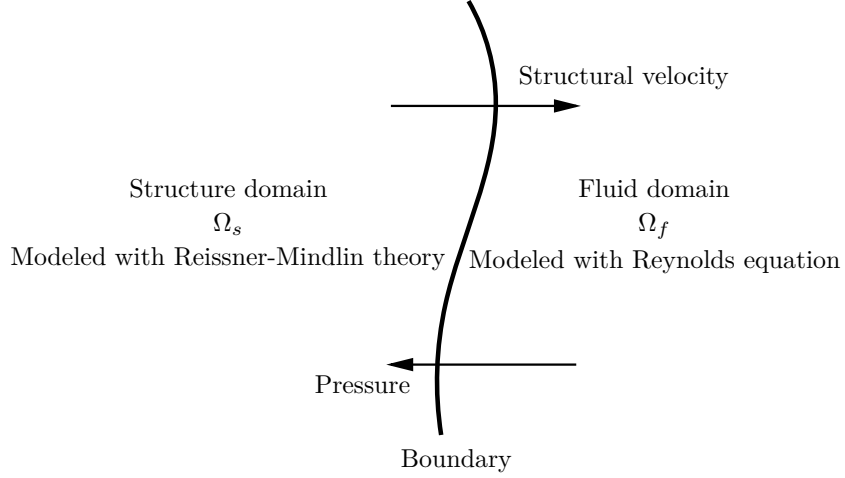


Figure 4.4: Coupled field with forces

A single pressure variable is enough to describe the dynamical behavior of the fluid. The coupling between fluid and structural domains is accomplished by considering the interface forces. This approach is widely employed since the total number of variables involved in the simulation becomes smaller.

4.3.1 Structure domain

Considering the energy expressions are given at Eqs. (3.28)-(3.29), the plate is discretized using four noded isoparametric quadrilateral plate elements with transversal and rotational deformations as shown in the Figure 4.5. The element has 12 degrees of freedom (DOF), i.e., one displacement u and two rotations θ_x and θ_y at each node. Using the nodal values, the displacement and structural rotations can be approximated within an element as

$$u = \sum_{i=1}^4 N_i u_i \quad , \quad \theta_x = \sum_{i=1}^4 N_i \theta_{xi} \quad , \quad \theta_y = \sum_{i=1}^4 N_i \theta_{yi} \quad (4.31)$$

where N_i represents the shape functions associated with i^{th} node and defined as follows

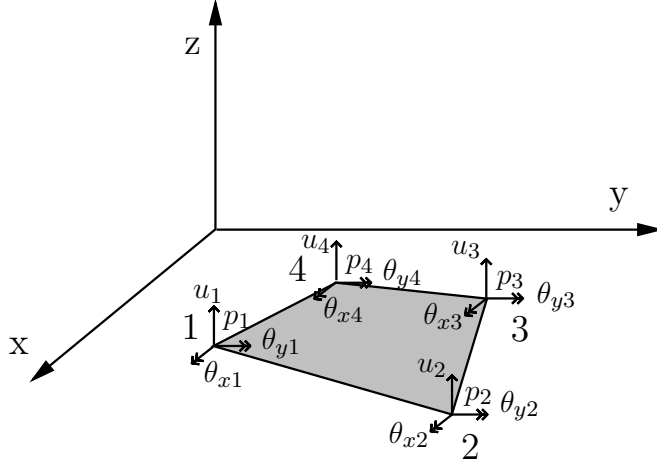


Figure 4.5: Kirchhoff plate element geometry coupled with pressure field

$$N_i = \frac{1}{4} (1 + \xi_i \xi) (1 + \eta_i \eta) \quad (4.32)$$

Now, the nodal degrees of freedom are,

$$\mathbf{u}_e = \left\{ u_1 \quad \theta_{x1} \quad \theta_{y1} \quad u_2 \quad \theta_{x2} \quad \theta_{y2} \quad u_3 \quad \theta_{x3} \quad \theta_{y3} \quad u_4 \quad \theta_{x4} \quad \theta_{y4} \right\}^T \quad (4.33)$$

where T denotes the transpose of a matrix.

The consistent plate element mass matrix of the four noded structure finite element can be written as

$$\mathbf{m}_e = \int_{\Omega_{se}} \rho \mathbf{N}^T \begin{bmatrix} h_t & 0 & 0 \\ 0 & h_t^3/12 & 0 \\ 0 & 0 & h_t^3/12 \end{bmatrix} \mathbf{N} d\Omega_{se} \quad (4.34)$$

where Ω_{se} represents the domain of the element and

$$\mathbf{N} = \begin{bmatrix} N_1 & 0 & 0 & \dots & N_4 & 0 & 0 \\ 0 & N_1 & 0 & \dots & 0 & N_4 & 0 \\ 0 & 0 & 0 & \dots & 0 & 0 & N_4 \end{bmatrix} \quad (4.35)$$

The bending stiffness matrix for the element can be obtained from the following relation assuming a linear elastic material with the stress-strain relation $\sigma = \mathbf{D}_b \epsilon$, and a strain-displacement relation $\epsilon = \mathbf{B} \mathbf{d}$ as,

$$\mathbf{k}_e = \int_{\Omega_{se}} \frac{h_t^3}{12} \mathbf{B}^T \mathbf{D}_b \mathbf{B} d\Omega_{se} + \int_{\Omega_{se}} \kappa h_t \mathbf{B}_s^T \mathbf{D}_s \mathbf{B}_s d\Omega_{se} \quad (4.36)$$

where \mathbf{B} and \mathbf{B}_s represent the differentiations of the shape function \mathbf{N} , as indicated in Eq.(3.30). More information of the derivation of the element matrices can be found at Ref. [70]. The calculation of derivatives w.r.t. physical coordinates needs calculation of Jacobian matrix \mathbf{J} as follows

$$\begin{Bmatrix} \partial/\partial\xi \\ \partial/\partial\eta \end{Bmatrix} = \mathbf{J} \begin{Bmatrix} \partial/\partial x \\ \partial/\partial y \end{Bmatrix} \quad \mathbf{J} = \begin{bmatrix} \partial x/\partial\xi & \partial y/\partial\xi \\ \partial x/\partial\eta & \partial y/\partial\eta \end{bmatrix} \quad (4.37)$$

The numerical integration is straightforward and handled using 2 x 2 Gauss-Legendre quadrature for bending and 1x1 for shear.

The finite element semi-discretized equation for the dynamics of the plate structure can now be written in the familiar form given below. The familiar form of the semi-discretized finite element equation which governs the plate structure dynamical behavior can be written given below. The internal material damping is not considered in the following equation of motion for the plate.

$$\mathbf{M}\ddot{\mathbf{u}} + \mathbf{K}\mathbf{u} = \mathbf{Q}^T \mathbf{p} \quad (4.38)$$

where \mathbf{K} , \mathbf{M} are the globally assembled stiffness and mass matrices respectively, and \mathbf{u} is the displacement vector. The second time derivative is represented by a superposed double dot. The fluid film-structure coupling is represented by the term $\mathbf{Q}^T \mathbf{p}$, where \mathbf{p} is the vector of the fluid film pressure. The element-wise version of the coupling matrix \mathbf{Q} is given by

$$\mathbf{Q}_e = \int_{\Omega_{se}} \mathbf{N}^T \mathbf{N}_f d\Omega_{se} \quad (4.39)$$

where the structure and fluid domain shape functions are represented by \mathbf{N} and \mathbf{N}_f respectively. Gnu Octave scripts are developed to obtain these matrices are

presented in Appendix A.2.5 for mass matrix \mathbf{M} , in Appendix A.2.4 for stiffness matrix \mathbf{K} and in Appendix A.2.6 for coupling matrix \mathbf{Q} .

4.3.2 Fluid domain

The fluid film is discretized using four noded quadrilateral elements as shown in the Figure 4.5. The element has only four DOF, i.e., pressure p at each node. The pressure within an element are approximated using their nodal values as given by

$$p = \sum_{i=1}^4 N_{fi} p_i \quad (4.40)$$

where N_{fi} represents the shape functions associated with i^{th} node and defined as Eq. (4.32).

Now, the nodal degrees of freedom are,

$$\mathbf{p}_e = \left\{ p_1 \quad p_2 \quad p_3 \quad p_4 \right\}^T \quad (4.41)$$

Using weak formulation and introducing the finite element approximations the Eq. (3.8) reduces to the following equation:

$$\mathbf{M}_f \dot{\mathbf{p}} + \mathbf{K}_f \mathbf{p} = \mathbf{Q}_f^T \dot{\mathbf{u}} \quad (4.42)$$

where \mathbf{M}_f and \mathbf{K}_f are the globally assembled mass and stiffness matrices for the fluid domain, respectively. The time derivative is represented by a superposed dot. The element-wise mass and stiffness matrices can be obtained from the following relations:

$$\mathbf{m}_{fe} = \frac{h_0}{P_a} \int_{\Omega_{fe}} \mathbf{N}_f^T \mathbf{N}_f d\Omega_{fe} \quad (4.43)$$

$$\mathbf{k}_{fe} = \frac{h_0^3}{12\mu_{eff}} \int_{\Omega_{fe}} \left(\frac{\partial \mathbf{N}_f^T}{\partial x} \frac{\partial \mathbf{N}_f}{\partial x} + \frac{\partial \mathbf{N}_f^T}{\partial y} \frac{\partial \mathbf{N}_f}{\partial y} \right) d\Omega_{fe} \quad (4.44)$$

The coupling matrix \mathbf{Q}_f transfers the velocities of the structure to the fluid domain and can be obtained by globally assembling the following the element-wise coupling matrix \mathbf{Q}_{fe}

$$\mathbf{Q}_{fe} = \int_{\Omega_{fe}} \mathbf{N}_f^T \mathbf{N} d\Omega_{fe} \quad (4.45)$$

The boundary conditions for the fluid can be

- Open to ambient pressure $p = 0$
- Pressure gradient is zero, or closed end $\frac{\partial p}{\partial n} = 0$

Due to the boundary conditions stated above, the weak formulation of the Eq. (3.8) doesn't include any boundary integration terms. The numerical integration of Eqs. (4.43) and (4.44) is handled using 2x2 Gauss-Legendre quadrature.

Gnu Octave scripts are developed to obtain above matrices are presented in Appendix A.2.2 for mass matrix \mathbf{M}_f , in Appendix A.2.1 for stiffness matrix \mathbf{K}_f and in Appendix A.2.3 for coupling matrix \mathbf{Q}_f .

If the gap thickness is variant within fluid domain, a more complex should be used to model the initial gap variation which is presented in Eq. (3.26). In this case, the Reynolds equation becomes more complex and may be nonlinear based on the initial gap distribution $h_i(x, y)$. The fluid element mass and stiffness matrices turn into the following forms which include non-uniform gap thickness.

$$\mathbf{k}_{fe} = \frac{h_0^3}{12\mu_{eff}} \int_{\Omega_{fe}} \left[h_i^3 \left(\frac{\partial \mathbf{N}_f^T}{\partial x} \frac{\partial \mathbf{N}_f}{\partial x} + \frac{\partial \mathbf{N}_f^T}{\partial y} \frac{\partial \mathbf{N}_f}{\partial y} \right) - 3h_i^2 \left(\frac{\partial h_i}{\partial x} \mathbf{N}_f^T \frac{\partial \mathbf{N}_f}{\partial x} + \frac{\partial h_i}{\partial y} \mathbf{N}_f^T \frac{\partial \mathbf{N}_f}{\partial y} \right) \right] d\Omega_{fe} \quad (4.46)$$

$$\mathbf{m}_{fe} = \frac{h_0}{P_a} \int_{\Omega_{fe}} h_i \mathbf{N}_f^T \mathbf{N}_f d\Omega_{fe} \quad (4.47)$$

4.3.3 Coupled Eigenvalue problem

The coupled eigenvalue equations can be obtained by combining Eqs. (4.38) and (4.42) as follows:

$$\begin{bmatrix} \mathbf{M} & \mathbf{0} & \mathbf{0} \\ \mathbf{0} & \mathbf{I} & \mathbf{0} \\ \mathbf{0} & \mathbf{0} & \mathbf{M}_f \end{bmatrix} \begin{Bmatrix} \ddot{\mathbf{u}} \\ \dot{\mathbf{u}} \\ \dot{\mathbf{p}} \end{Bmatrix} + \begin{bmatrix} \mathbf{0} & \mathbf{K} & -\mathbf{Q}^T \\ -\mathbf{I} & \mathbf{0} & \mathbf{0} \\ -\mathbf{Q}_f^T & \mathbf{0} & \mathbf{K}_f \end{bmatrix} \begin{Bmatrix} \dot{\mathbf{u}} \\ \mathbf{u} \\ \mathbf{p} \end{Bmatrix} = \begin{Bmatrix} \mathbf{0} \\ \mathbf{0} \\ \mathbf{0} \end{Bmatrix} \quad (4.48)$$

where \mathbf{I} and $\mathbf{0}$ represents identity and zero matrices with proper size respectively. The above equation can be rewritten in a compact form as

$$\mathbf{M}_G \dot{\mathbf{x}} + \mathbf{K}_G \mathbf{x} = \mathbf{0} \quad (4.49)$$

Unlike banded structural and fluid domain mass and stiffness matrices, the solution and implementation of resulting denser matrices need larger data storage and longer cpu time.

The generalized eigenvalue problem is to determine the nontrivial solutions of the Eq. (4.49) is given by introducing

$$\mathbf{x} = \varphi e^{\lambda t} \quad (4.50)$$

as follows

$$(\mathbf{K}_G + \lambda \mathbf{M}_G) \varphi = \mathbf{0} \quad (4.51)$$

The solution of the above generalized eigenvalue problem is straightforward and can be handled using standard numerical techniques. These techniques include basic subspace iteration algorithm or more advanced projection methods such as least squares Arnoldi algorithms, Lanczos algorithms, etc. [71]. However, one of the main disadvantages of this approach is the rearrangement of the matrices to form \mathbf{K}_G and \mathbf{M}_G which also causes a longer solution time due to complex eigenvalues. To overcome this issue, the following simple method is proposed. Assuming the harmonic motion of the angular frequency ω , the structure displacements and the fluid pressures can be expressed as

$$\begin{aligned}\mathbf{u} &= \mathbf{u}_0 e^{j\omega t} \\ \mathbf{p} &= \mathbf{p}_0 e^{j\omega t}\end{aligned}\tag{4.52}$$

Eq. (4.48) can be rewritten using following

$$\mathbf{p}_0 = j\omega \left(\mathbf{K}_f + j\omega \mathbf{M}_f \right)^{-1} \mathbf{Q}_f^T \mathbf{u}_0 \tag{4.53}$$

The following equation can be obtained by substituting Eq. 4.53 into the Eq. (4.38) in which results

$$\left(\mathbf{K} - \omega^2 \mathbf{M} - j\omega \mathbf{Q}^T \left(\mathbf{K}_f + j\omega \mathbf{M}_f \right)^{-1} \mathbf{Q}_f^T \right) \mathbf{u}_0 = \mathbf{0} \tag{4.54}$$

The above equation, on pre and post multiplication with ϕ_i^T and ϕ_i , can be rewritten in the following form

$$\left(\omega_i^2 - \omega^2 - j\omega \phi_i^T \mathbf{Q}^T \left(\mathbf{K}_f + j\omega \mathbf{M}_f \right)^{-1} \mathbf{Q}_f^T \phi_i \right) \mathbf{u}_0 = \mathbf{0} \tag{4.55}$$

or in compact form as $\mathbf{A} \mathbf{u}_0 = \mathbf{0}$ where ω_i and ϕ_i are the i^{th} natural frequency and the mass normalized eigenvector of the following pure structural equation

$$\mathbf{K} \mathbf{u}_0 = \omega^2 \mathbf{M} \mathbf{u}_0 \tag{4.56}$$

The nontrivial solutions of Eq. (4.55) can be found by investigation the roots of $\det(\mathbf{A}) = 0$ which can be solved by using the iterative conjugate gradient method for ω . Then the corresponding damped eigenvector can be found by putting complex natural frequency solution to the Eq. (4.55). Once the damped eigenvector is obtained the pressure distribution can be calculated using Eq. (4.53) by replacing ω and \mathbf{u}_0 by obtained damped eigenvalue and eigenvector solution.

The frequency response function of the coupled system for a particular harmonically varying external force \mathbf{f}_{ext} can be obtained using Eq. (4.54) as

$$\left(\mathbf{K} - \omega^2 \mathbf{M} - j\omega \mathbf{Q}^T \left(\mathbf{K}_f + j\omega \mathbf{M}_f \right)^{-1} \mathbf{Q}_f^T \right) \mathbf{u}_0 = \mathbf{f}_{ext} \tag{4.57}$$

Another important special case is to use two plates. The vibration and noise of an oscillating surface can be suppressed by adding another plate to create a fluid film between two plates. This also enables blocking of sound and provides extra noise suppression. However, the pumping fluid motion inside the film may create a high frequency noise. Addition of the SFD to the main structure can be modeled using previous approach as

$$\mathbf{M}_{ct} \begin{Bmatrix} \ddot{\mathbf{u}} \\ \dot{\mathbf{u}} \\ \dot{\mathbf{p}} \\ \ddot{\mathbf{u}}_b \\ \dot{\mathbf{u}}_b \end{Bmatrix} + \begin{bmatrix} \mathbf{0} & \mathbf{K} & -\mathbf{Q}^T & \mathbf{0} & \mathbf{0} \\ -\mathbf{I} & \mathbf{0} & \mathbf{0} & \mathbf{0} & \mathbf{0} \\ -\mathbf{Q}_f^T & \mathbf{0} & \mathbf{K}_f & \mathbf{Q}_{bf}^T & \mathbf{0} \\ \mathbf{0} & \mathbf{0} & \mathbf{Q}_b^T & \mathbf{0} & \mathbf{K}_b \\ \mathbf{0} & \mathbf{0} & \mathbf{0} & -\mathbf{I} & \mathbf{0} \end{bmatrix} \begin{Bmatrix} \dot{\mathbf{u}} \\ \mathbf{u} \\ \mathbf{p} \\ \dot{\mathbf{u}}_b \\ \mathbf{u}_b \end{Bmatrix} = \begin{Bmatrix} \mathbf{0} \\ \mathbf{0} \\ \mathbf{0} \\ \mathbf{0} \\ \mathbf{0} \end{Bmatrix} \quad (4.58)$$

where \mathbf{u}_b is the base structural displacement vector, \mathbf{M}_b , \mathbf{K}_b are the mass and stiffness matrices of the base structure, \mathbf{Q}_b and \mathbf{Q}_{bf} are the coupling matrices between base structure and the fluid film, and coupled mass matrix

$$\mathbf{M}_{ct} = \text{diag} \left\{ \mathbf{M} \quad \mathbf{I} \quad \mathbf{M}_f \quad \mathbf{M}_b \quad \mathbf{I} \right\} \quad (4.59)$$

It is important to note that an additional term is added to fluid film equation due to difference between base structure and SFD velocities. Above equation implies that the base and SFD vibrations can be suppressed using a single fluid film. Enhancement of the vibration damping is directly related to the difference between velocities of oscillating surfaces.

The coupling matrices \mathbf{Q}_f and \mathbf{Q}_{bf} are the same matrices when the base structure is also modeled using same shape functions as in SFD model since the base and the SFD shares identical boundary with the fluid film. In a particular case where the base and SFD possess same velocity magnitudes and directions, the fluid domain coupling terms cancel each other and the fluid film domain doesn't provide an extra damping or stiffness to the plates.

4.3.4 Simple cases and validation of FEA

In this section, some specific results for FEM computations of fluid–structure interaction are given using the formulation described in this section previously. To illustrate the fluid-structure behavior, a simple 2 DOF coupled system which has the following matrices is selected.

$$\begin{aligned} \mathbf{K} &= \begin{bmatrix} 10 & 5 \\ 5 & 10 \end{bmatrix} & \mathbf{M} &= \begin{bmatrix} 3 & 0 \\ 0 & 3 \end{bmatrix} \\ \mathbf{K}_f &= \frac{h_0^3}{12\mu} \begin{bmatrix} 4 & -1 \\ -1 & 4 \end{bmatrix} & \mathbf{M}_f &= \frac{h_0}{P_a} \begin{bmatrix} 2 & 1 \\ 1 & 2 \end{bmatrix} \\ \mathbf{Q} &= \begin{bmatrix} 2 & 1 \\ 1 & 0.2 \end{bmatrix} & \mathbf{Q}_f &= \begin{bmatrix} 1 & -1 \\ -1 & 7 \end{bmatrix} 10^{-2} \end{aligned} \quad (4.60)$$

The effects of the fluid film thickness, the ambient pressure and viscosity are shown in Figure 4.6. The effect of film thickness on the receptance is obtained with various film thickness values starting from $10^{-2}m$ to $10^{-5}m$. The decrease of the gap thickness and the increase on the viscosity increase damping levels as expected. The effect of the ambient pressure change ($P_a = 100Pa - 1MPa$) doesn't provide an extra damping without considering its effect on other parameters such as viscosity and fluid density.

Next, a rectangular plate-fluid system considered for the verification study. The plate is 49cm wide 24.5cm height, with a thickness of 1mm. The plate is clamped at the edges. The box is made of aluminum and material properties are

$$E = 70 \times 10^9 N/m^2, \quad \rho = 2710 kg/m^3 \text{ and } \nu = 0.3 \quad (4.61)$$

The properties of the air in the gap under standard atmospheric conditions are

$$P_a = 101325 N/m^2 \text{ and } \mu = 1.82 \times 10^{-5} Ns/m^2 \quad (4.62)$$

The damped eigenfrequencies of the plate were calculated with a mesh of 514 plate elements and compared both with measurement results obtained by Beltman [6] and analytical results according to the formula given by Blevins [72] in vacuum.

The results are shown in Table 4.7. In this table, first column represents the number of half wave lengths in the x and the y directions.

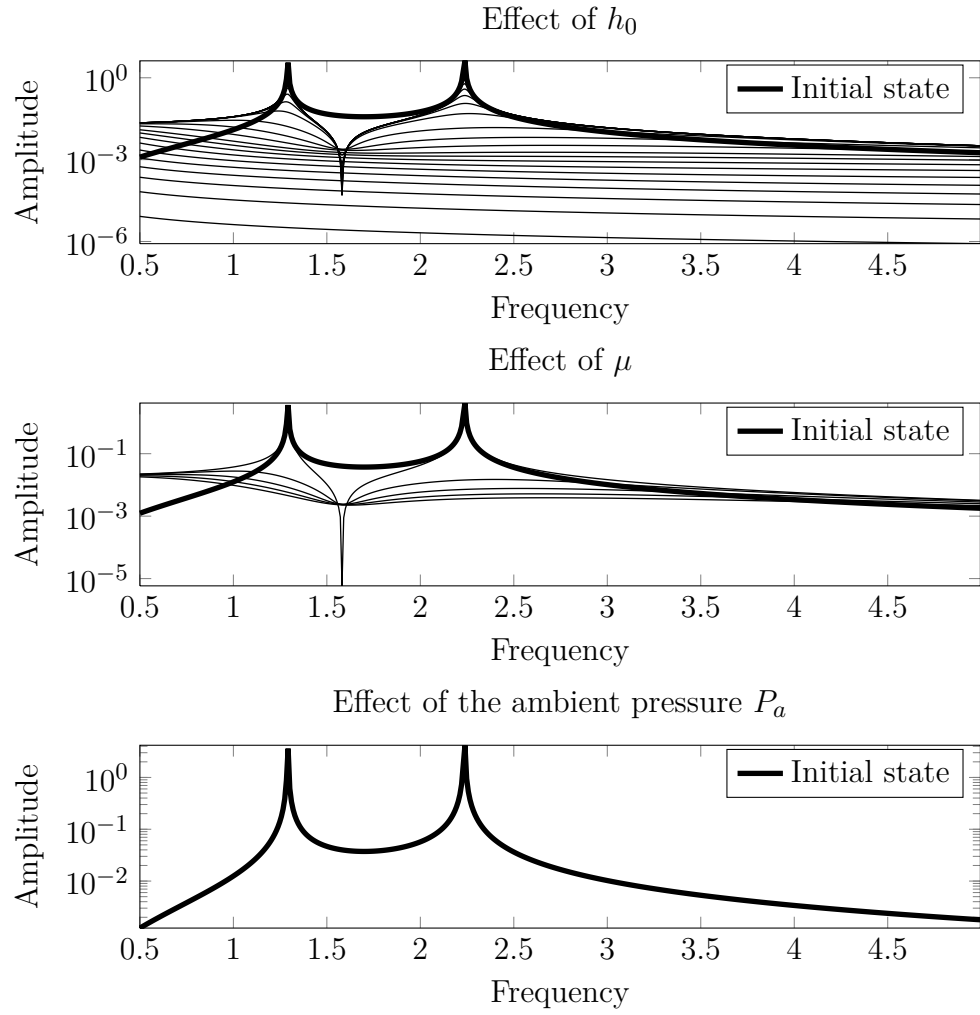


Figure 4.6: Effect of the film thickness, the fluid viscosity and the ambient pressure

Table 4.7
Eigenfrequencies (Hz) of rectangular clamped plate on air film

Mode	Analytical [72]	Measurement [6]	Present study
1,1	100.6	96.2	96.36
2,1	130.4	130.1	130.2
3,1	183.4	181.8	182.9
4,1	259.7	253.8	255.4
1,2	261.7	247.4	257.1
2,2	291.2	280.8	284.3
3,2	341.0	322.6	335.2

The results obtained by using present approach is slightly lower than the analytical results due to mass loading of the fluid. Due to Bellman's observations, there is moderate agreement between the calculations and the experiments. The results tend to be less accurate due to the small number of elements for the higher modes.

A rectangular aluminum plate which has dimensions of $10\text{cm} \times 6\text{cm} \times 1\text{mm}$ is selected as the second example. One of the shorter edges of the plate is clamped and all the other edges are free and open to ambient pressure. Shift of the eigenvalues and damping ratios are listed in Table 4.8.

Table 4.8
Natural frequencies (Hz) and damping ratios of clamped-free-free-free rectangular plate for various fluid film thicknesses

Vacuum (Hz)	Present study (Hz)			
	$h_0 = 0.5\text{mm}$	$h_0 = 1\text{mm}$	$h_0 = 2\text{mm}$	$h_0 = 5\text{mm}$
84.47	85.27 $\zeta = 14.9\%$	84.54 $\zeta = 1.96\%$	84.48 $\zeta = 0.24\%$	84.47
311.5	311.5 $\zeta = 0.23\%$	311.5 $\zeta = 0.03\%$	311.5 $\zeta = 0.00\%$	311.5
526.8	525.9 $\zeta = 3.73\%$	526.3 $\zeta = 0.46\%$	526.7 $\zeta = 0.06\%$	526.8
1038.2	1038.1 $\zeta = 0.41\%$	1038.2 $\zeta = 0.05\%$	1038.2 $\zeta = 0.00\%$	1038.2
1461.5	1462.2 $\zeta = 1.21\%$	1461.6 $\zeta = 0.14\%$	1461.5 $\zeta = 0.02\%$	1461.5

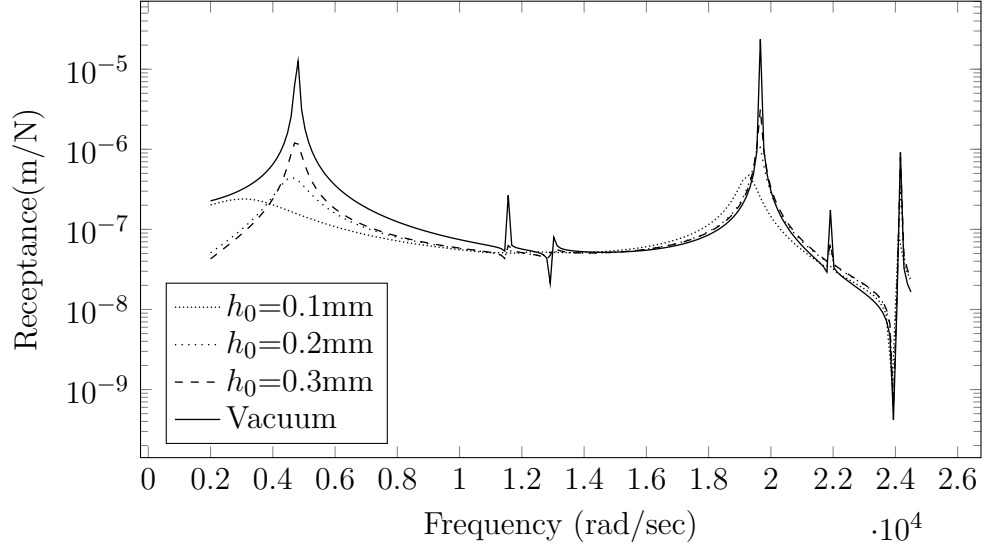


Figure 4.7: Frequency response function

The calculated eigenfrequency shifts are compared against the undamped natural frequency results. The sensitivities of the second and fourth modes to the gap thickness change are lesser than the others. This is due to the difference between the mass loading effects.

An aluminum 1cm thick rectangular plate which is pinned from the bottom corners is selected as the third example. The dimensions of the plate are selected as 25cm by 15cm. The frequency response function is calculated and shown in Figure 4.7 to emphasize the effect of film thickness on the dynamical behavior of the structure.

The shifts of the structural natural frequencies are dependent on the fluid film thickness as expected. Interestingly, the effect is not uniform and dependent upon the mode shape of the structure. The first and fourth receptance peak regions show that the amount of damping and shift is different for each case.

4.3.5 Example : Condenser microphone with stationary backplate

Microphone is an acoustic sensor that converts an incident pressure into a corresponding output voltage. The condenser or capacitive type of microphones are

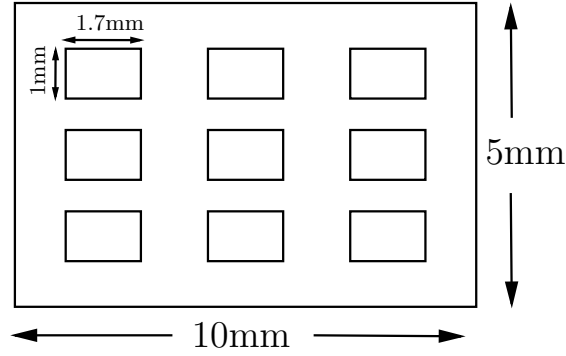


Figure 4.8: Microphone backplate

very popular among microphones due to high their sensitivity, excellent noise characteristics, good stability, and flat frequency response [73].

Capacitor or condenser microphones work on the same principle that *“one plate of a capacitor is accessible to the air while the other plate is fixed. As the air pressure changes, it causes the gap distance between the plates to change, thus changing the capacitance. The change in capacitance is instantly captured electronically and converted to a proportional voltage by the microphone’s electronic circuit.”*

For a condenser microphone, the principle components are the diaphragm, air and backplate. The diaphragm’s base material is a thin nonconductor plastic sheet with a molecularly thin coating of a conductor, such as gold, nickel or aluminum on back facing side.

An aluminum-mylar plastic diaphragm which has the first natural frequency of 12kHz is considered in this example. The diaphragm has 10mm width, 5mm height and 0.1mm thickness. The backplate has 6 holes which have dimensions of 1.7mm \times 1mm. and can be seen in Figure 4.8. The purpose of the holes is to reduce the effect of the air film on the diaphragm.

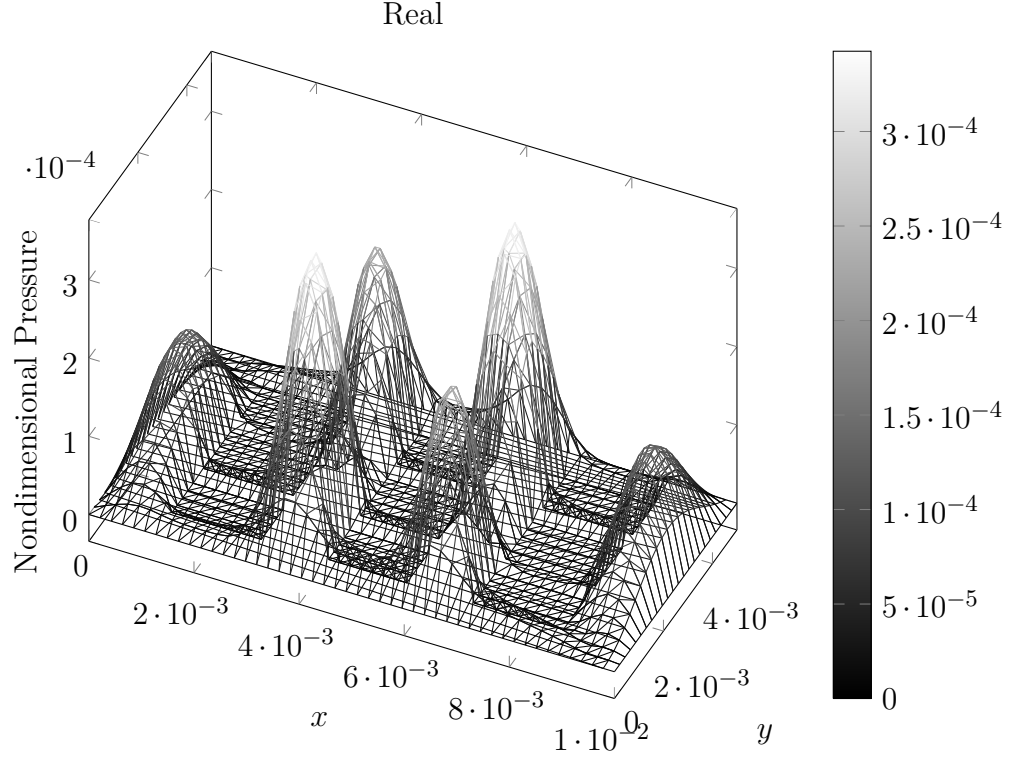


Figure 4.9: Nondimensional real pressure distribution underneath the microphone diaphragm

The resulting pressure distribution for 6kHz both in real and imaginary parts are shown in figures 4.9-4.10. As it can be seen from these figures, the holes are reducing the pressure underneath the microphone diaphragm which enhances the frequency range of the microphone.

The frequency response of the microphone diaphragm is a very important and effects the sensitivity of the microphone. For example, if a softer metal-polymer is selected as the diaphragm material, the deflection will be larger if the diaphragm is exposed to the same pressure, thus increasing the sensitivity. The calculated response both in vacuum and air is presented in Figure 4.11. As it can be seen from the figure, the mass loading is more severe than the stiffness effect which result in lower cutoff frequency. Moreover, the fluid trapped between the diaphragm and backplate injects damping which lowers the resonant response.

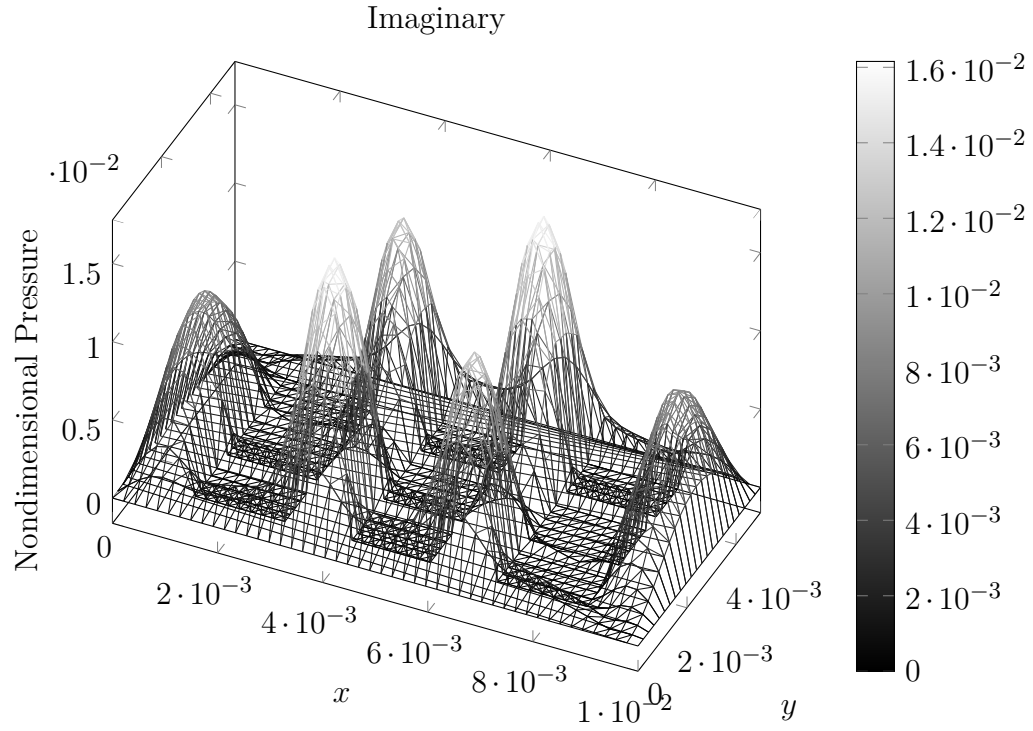


Figure 4.10: Nondimensional imaginary pressure distribution underneath the microphone diaphragm

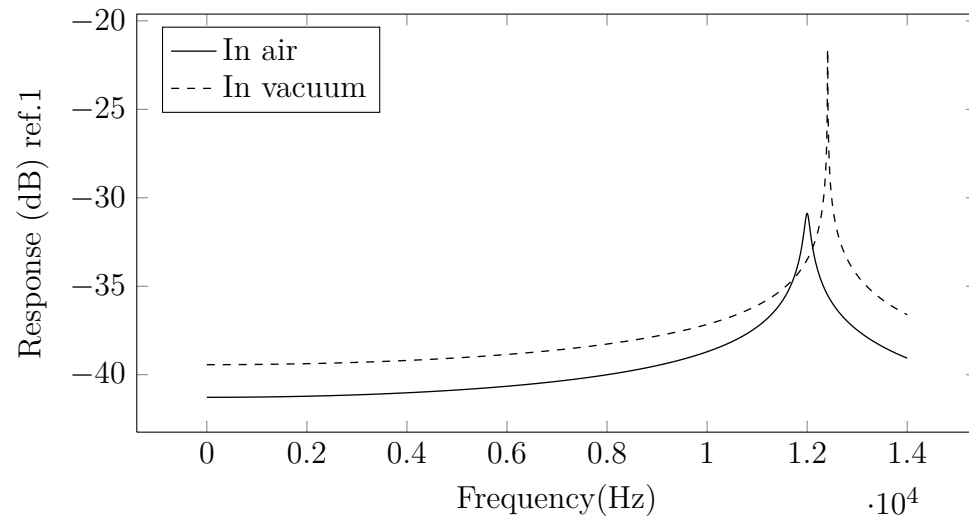


Figure 4.11: Frequency response of microphone diaphragm

5 Nonlinear analysis²

The non-homogeneous Helmholtz equations (3.8)-(3.10) can be solved using Green's functions exactly [23] for simple and uniform deflection profiles. In this section, more realistic plate deflection shapes are considered in calculations while carrying out the modal force approach. Once the first harmonic equation (3.8) is solved using Green's functions, Fourier series or using numerical methods, second harmonics problem which is presented at equation (3.9) can be solved using first harmonic solution. Moreover, higher harmonics can also be sequentially solved since all equations are non-homogeneous Helmholtz equations, of which the forcing term is always known. However, these sequential equation solutions become more complex with each harmonic and solution could be utilized by using a special software which has symbolic calculation capabilities such as Gnu Maxima [69].

5.1 Solution using Green's function

Darling et al. [23] demonstrated the usage of Green's function to solve linearized non-homogeneous Reynolds equation. Compact analytical models were also presented considering rigid uniform and tilting motion of the plate. This assumptions could be valid in very low frequencies where the plate oscillates as a rigid body i.e. the vibration frequency is very low compared to the first natural frequency of the plate. The later assumption can be interpreted as the connection stiffness of the plate is much softer than the transversal rigidity of the plate. However, the mode shapes of the rectangular plates are not considered. This present section is the extension of the solution to elastic models of plates considering nonlinear Reynolds equation.

The general solution to the linearized Reynolds equation (3.8) can be given using infinite series as

$$a_1(x, y) = \sum_{m=1}^{\infty} \sum_{n=1}^{\infty} b_{mn} f_m(x) g_n(y) \quad (5.1)$$

²The material contained in this section was previously published partly in M.M.A. Bicak and M.D. Rao, Analytical modeling of squeeze film damping for rectangular elastic plates using Green's functions, Journal of Sound and Vibration, Volume 329, Issue 22, 25 October 2010, Pages 4617-4633.

where $f_m(x)$ and $g_n(y)$ are harmonic functions of x and y respectively which satisfy boundary conditions, b_{mn} is a complex constant number. The derivative of $f_m(x)$ and $g_n(y)$ are

$$\frac{\partial^2 f_m(x)}{\partial x^2} = -m^2 \alpha^2 f_m(x) \text{ and } \frac{\partial^2 g_n(y)}{\partial y^2} = -n^2 \beta^2 g_n(y) \quad (5.2)$$

where m and n are the integer numbers that can be odd or even based on the boundary configuration, α and β are multipliers of x and y inside functions f_m and g_n . If the mode shape Φ of the plate is expanded to the same series such as

$$\Phi(x, y) = \sum_m^\infty \sum_n^\infty \epsilon_{mn} f_m(x) g_n(y) \quad (5.3)$$

If Eqs. (5.1) and (5.3) are put to the Eq. (3.8), the following relationship can be obtained as

$$b_{mn} = \frac{-j\sigma\delta}{m^2\alpha^2 + n^2\beta^2 + j\sigma} \epsilon_{mn} \quad (5.4)$$

If the same procedure is applied for the second harmonic considering the same $f_m(x)$ and $g_n(y)$ functions,

$$R(x, y) = \sum_m^\infty \sum_n^\infty r_{mn} f_m(x) g_n(y) \quad (5.5)$$

$$r_{nm} = \int_0^{L_y} \int_0^{L_x} R f_m(x) g_n(y) \quad (5.6)$$

where known forcing function R is

$$R = b_{mn} \left\{ (b_{mn} + 3\delta\epsilon_{mn}) (f_m'^2 g_n'^2 + f_m^2 g_n'^2 - \vartheta f_m^2 g_n^2) - 2j\sigma\delta\epsilon_{mn} f_m^2 g_n^2 \right\} \quad (5.7)$$

where f_m' and g_n' is the derivative with respect to its independent variable and $\vartheta = m^2\alpha^2 + n^2\beta^2$. In this case, the series turn into,

$$b_{mn} = \frac{r_{nm}}{m^2\alpha^2 + n^2\beta^2 + 2j\sigma} \quad (5.8)$$

The generalized solution to z^{th} harmonic solutions can also be given in the same form

$$a_z(x, y) = \sum_m^{\infty} \sum_n^{\infty} c_{mn} f_m(x) g_n(y) \quad (5.9)$$

where

$$c_{mn} = \frac{s_{mn}}{m^2 \alpha^2 + n^2 \beta^2 + z j \sigma} \quad (5.10)$$

where s_{mn} represents the coefficients of the residual known term expansion which is dependent upon the solutions of all harmonics up to z^{th} harmonic.

The pressure domain solution (5.4) can be represented in compact form using Green's function also as

$$p(x, y) = \int_0^{L_y} \int_0^{L_x} \Phi(\xi, \eta) G(x, y, \xi, \eta) d\xi d\eta \quad (5.11)$$

where G is the Green's function which is

$$G(x, y, \xi, \eta) = \sum_m^{\infty} \sum_n^{\infty} \epsilon_{mn} f_m(x) g_n(y) f_m(\xi) g_n(\eta) \quad (5.12)$$

where ϵ_{mn} is a multiplier which is dependent upon m , n , ω and σ .

Using the pressure solution, the modal force can be written as

$$N = \int_0^{L_y} \int_0^{L_x} \Phi(x, y) p(x, y) dx dy \quad (5.13)$$

If both mode shapes are selected as to be orthonormal, which satisfy

$$\int_0^{L_y} \int_0^{L_x} \rho \Phi(x, y) \Phi(x, y) dx dy = 1 \quad (5.14)$$

modal force is reduced to

$$N = \sum_m^{\infty} \sum_n^{\infty} \frac{-j \sigma \delta}{m^2 \alpha^2 + n^2 \beta^2 + j \sigma} \epsilon_{mn}^2 \quad (5.15)$$

5.2 Calculation of squeeze film stiffness and damping

According to the analysis of Langlois [22], and Griffin et al. [74], squeeze film air provides extra damping and stiffness force to the system. For a finite element modeled system, one can get mass, stiffness and damping matrices as

$$\mathbf{M}\ddot{x} + \mathbf{K}x = \mathbf{f}(x, \dot{x}) \quad (5.16)$$

Eq. (5.16) can be expressed in terms of modal vectors, $x(t) = \Phi\varphi(t)$ in which Φ represents modal vector as follows

$$\ddot{\varphi} + \omega_n^2\varphi = \Phi^T f(\Phi\varphi, \Phi\dot{\varphi}) \quad (5.17)$$

where ω_n and $\varphi(t)$ represent natural frequency and modal coordinates. For a continuous system, Eq. (5.17) can be written as

$$\ddot{\varphi} + \omega_n^2\varphi = \int_{\Omega_s} \Phi f(\Phi\varphi, \Phi\dot{\varphi}) d\Omega_s \quad (5.18)$$

where Ω_s represents solution domain. After the calculation of the modal forcing term, imaginary part can be converted into velocity component using the relationship $\dot{\varphi} = j\omega\varphi$.

The right hand side of the equation, the modal force provides two components in-phase and out-of-phase which can be decomposed as $\Phi^T f = -F_k\varphi - F_d\dot{\varphi}$. Considering a single degree of freedom system, damping ratio and natural frequency shift can be found as

$$\zeta = \frac{1}{2\omega_n} F_d \quad (5.19)$$

$$\Delta\omega = \sqrt{\omega_n^2 + F_k} - \omega_n \quad (5.20)$$

The mass normalized mode shapes are used in order to calculate modal damping and frequency shift using Eqs. (5.19) and (5.20). The other way to calculate the damping ratio and frequency shift is to use time integration technique and

calculating the phase difference. However, nonlinearity or higher harmonics can not be captured since the stiffness and damping are calculated based on the phase difference between velocity and pressure. Moreover, the sucking and squeezing motions create unequal fluctuations around ambient pressure. Other procedures for calculation of damping ratios and frequency shifts can be summarized as follows:

- An impact force is applied to the base structure, then the damping ratio can be calculated using decay response. For each time step, the displacements as well as the velocities acting on air film is applied to Reynolds equations. As a second step, nodal forces caused by pressure are applied back to the attached plate. This iteration process continues to the end of simulation time. This procedure can be implemented if the base structure model is already known.
- The attached plate motion is calculated for each time step with imposed initial displacements or velocities. The Reynolds equation is solved with calculated attached plate displacements, velocities, and surface velocities of the base structure. The damping ratio can be calculated using decay response as in previous case. This technique doesn't need a structural model of the base structure. Therefore, it can be applicable to experimental models directly. Generally, imposed initial displacements or velocities are selected as the mode shapes or a frequency response function for a selected frequency.
- Energy balance of the structure and the fluid domain can be used to calculate energy dissipation. So far only molecular level calculations are reported [25]. For the continuum region, the difficulty of this procedure is the determination of the heat transferred to the structure since Reynolds equation is an isothermal equation and temperature gradients along gap should be considered.

5.3 Examples

To illustrate the details of the pressure and modal force solution, transverse motion of a rectangular plate ($\beta = \pi/2$) is considered. The problem domain is selected as $0 \leq x \leq L_x$ and $0 \leq y \leq L_y$ corresponding to a rectangular plate of dimensions L_x, L_y . Proper Green's function is constructed and used for each different case.

Table 5.1
Mode Shapes

Configuration	Mode Shape $\Phi(x,y)$
CCCC	$\left(\cos \frac{2\pi x}{L_x} - 1\right) \left(\cos \frac{2\pi y}{L_y} - 1\right)$
CFCC	$\left(1 - \cos \frac{\pi x}{2L_x}\right) \left(\cos \frac{2\pi y}{L_y} - 1\right)$
FCFC	$\left(1 - \cos \frac{2\pi x}{L_x}\right)$
FSFS	$\left(\sin \frac{\pi x}{L_x}\right)$
CFFC	$\left(1 - \cos \frac{\pi x}{2L_x}\right) \left(1 - \cos \frac{\pi y}{2L_y}\right)$
FFFC	$\left(1 - \cos \frac{\pi x}{2L_x}\right)$

For structural modal solution, approximate mode shapes for Poisson's ratio is 0.25 which can be found in Ref. [75] are used. Tabulated mode shapes are calculated approximately using the Rayleigh method. In order to solve the problem defined by the Eq. (3.5), boundary conditions should be defined. For the boundary edges there are two different boundary conditions:

- Boundary point is open to ambient pressure $p = P_a$
- Pressure gradient is zero, or closed end $\frac{\partial p}{\partial n} = 0$ where n is the outwards normal vector at the boundary.

The structural boundary conditions for the plate edges are represented by four letters. For example, CFCS stands for Clamped-Free-Clamped-Simply supported plate for bottom ($y = 0$), right ($x = L_x$), upper ($y = L_y$) and left edge ($x = 0$). It is assumed that the pressure gradient is zero for simply supported and clamped edges, whereas boundary condition is open to ambient air for free edge. Investigated mode shapes are shown at the Table 5.1.

5.3.1 Exact solution for clamped boundary conditions (CCCC)

For the clamped boundaries case, approximate normalized mode shape [75] using Rayleigh method is given as

$$\Phi(x, y) = \left(\cos \frac{2\pi x}{L_x} - 1 \right) \left(\cos \frac{2\pi y}{L_y} - 1 \right) \quad (5.21)$$

The first order pressure a_1 can be written using Eq. (5.1) where

$$f(x) = \cos \frac{2\pi mx}{L_x} \quad g(y) = \cos \frac{2\pi ny}{L_y} \quad (5.22)$$

Since the mode shape can be represented by using only four terms of the entire series, the solution of the non-homogeneous Helmholtz equation yields only four terms. Using the solution, the modal force can be calculated as follows,

$$a_1(x, y) = \delta \left(-1 + \frac{j\sigma}{\alpha^2 + j\sigma} f(x) + \frac{j\sigma}{\beta^2 + j\sigma} g(y) - \frac{j\sigma}{(\alpha^2 + \beta^2) + j\sigma} f(x) g(y) \right) \quad (5.23)$$

where $\alpha = 2\pi/L_x$, $\beta = 2\pi/L_y$, $f(x) = \cos \alpha x$ and $g(y) = \cos \beta y$. And modal force can be obtained as using orthonormalized mode shape Eq. (5.21) as

$$N = -\frac{1}{3} \sqrt{\frac{L_x L_y}{\rho}} P_a \delta \left(2 + \frac{j\sigma}{\alpha^2 + j\sigma} + \frac{j\sigma}{\beta^2 + j\sigma} + \frac{1}{2} \frac{j\sigma}{\alpha^2 + \beta^2 + j\sigma} \right) \quad (5.24)$$

where ρ is the constant mass density per unit area of the plate.

Unlike the solution which is given by Darling et al. [23], which exhibits infinite series solution for uniform plate displacement, the solution to particular mode shape includes the first couple of terms of the entire series due to the expansion of mode shape. Darling concluded that the damping mechanism doesn't exist considering uniform motion. However, even if all the edges are closed, the pumping mechanism due to mode shape deflection exists which creates damping, which is plausible and can be understood by considering the imaginary part of Eq. (5.23).

5.3.2 Case: CFCC

Considering the same plate geometry as before, but a free edge at $y = L_y$, nondimensional pressure a_1 can be obtained as,

$$a_1(x, y) = \sum_m \frac{j\sigma \delta(-1)^{\frac{m-1}{2}} \epsilon_{mn}}{m\pi} \left(\frac{1}{A_1} - \frac{1}{A_2} \cos \frac{2\pi y}{L_y} \right) \cos \frac{m\pi x}{2L_x} \quad (5.25)$$

where $\epsilon_{mn} = \begin{cases} -\frac{\pi-4}{2} & m=1 \\ 4 & m>1 \end{cases}$ and $A_1 = \frac{m^2\pi^2}{4L_x^2} + j\sigma$, $A_2 = \frac{m^2\pi^2}{4L_x^2} + 4\frac{\pi^2}{L_y^2} + j\sigma$, $j = \sqrt{-1}$ for $m = 1, 3, 5, \dots$

After using the orthonormalized mode shape with a multiplier $\frac{1}{2}\sqrt{3L_xL_y\frac{3\pi-8}{\rho\pi}}$, modal force can be written as,

$$N = \sum_m \frac{-j\sqrt{L_xL_y}P_a\sigma\delta\epsilon_{mn}}{2\sqrt{3}\pi^2Sm^2\sqrt{\rho}} \left(\frac{1}{A_1} + \frac{1}{2A_2} \right) \quad (5.26)$$

where $\epsilon_{mn} = \begin{cases} \pi^2 - 8\pi + 16 & m=1 \\ 32 & m>1 \end{cases}$, and $S = \sqrt{\frac{3\pi-8}{\pi}}$.

5.3.3 Case: FCFC and FSFS

Considering the same plate geometry as before, but with the clamped edges which is zero flow condition expressed as at $x=0$ and $x=L_x$, and free edges at $y=0$ and $y=L_x$, the nondimensional pressure can be found as

$$a_1(x, y) = \sum_n \frac{4j\sigma\delta}{\pi n} \left(\frac{1}{A_1} - \frac{1}{A_2} \cos \frac{2\pi x}{L_x} \right) \sin \frac{n\pi y}{L_y} \quad (5.27)$$

where $A_1 = \frac{n^2\pi^2}{L_y^2} + j\sigma$ and $A_2 = \frac{4\pi^2}{L_x^2} + \frac{n^2\pi^2}{L_y^2} + j\sigma$ for $n = 1, 3, 5, \dots$

Using $\frac{1}{2} \left(\frac{6L_xL_y}{\rho} \right)^{1/2}$ as orthonormal scaling factor, one can find the modal force as,

$$N = \sum_n \frac{-4\sqrt{2}j\sqrt{L_xL_y}P_a\sigma\delta}{\sqrt{3}\pi^2n^2\sqrt{\rho}} \left(\frac{2}{A_1} + \frac{1}{A_2} \right) \quad (5.28)$$

If the simply supported mode shape is used then the pressure and modal force turn into

$$a_1(x, y) = \sum_m \sum_n \frac{8j\sigma\delta\epsilon_{mn}}{\pi^2(m^2-1)n\left(\frac{m^2\pi^2}{L_x^2} + \frac{n^2\pi^2}{L_y^2} + j\sigma\right)} \cos \frac{m\pi x}{L_x} \sin \frac{\pi ny}{L_y} \quad (5.29)$$

$$N = \sum_m \sum_n \frac{-32\sqrt{2}j\sqrt{L_x L_y} P_a \sigma \delta \epsilon_{mn}}{\pi^4(m^2-1)n^2\sqrt{\rho}\left(\frac{m^2\pi^2}{L_x^2} + \frac{n^2\pi^2}{L_y^2} + j\sigma\right)} \quad (5.30)$$

where $\epsilon_{mn} = \begin{cases} 1 & m=1 \\ 2 & m>1 \end{cases}$, and orthonormal scaling factor is $\sqrt{\frac{L_x L_y}{2\rho}}$ for $m=0, 2, 4, \dots$ and $n=1, 3, 5, \dots$

5.3.4 Case: FFFC

In this case, three edges where $x = L_x$, $y = 0$ and $y = L_y$ are considered as open to ambient air, and left edge is considered as zero flow condition at $x = 0$, nondimensional pressure is

$$a_1(x, y) = \sum_m \sum_n \frac{j\sigma\delta\epsilon_{mn}}{\pi^2 mn \left(\frac{m^2\pi^2}{4L_x^2} + \frac{n^2\pi^2}{L_y^2} + j\sigma\right)} \cos \frac{m\pi x}{2L_x} \sin \frac{\pi ny}{L_y} \quad (5.31)$$

where

$$\epsilon_{mn} = \begin{cases} \frac{\pi-4}{4} & m=1 \\ (-1)^{\frac{m+1}{2}} & m>1 \end{cases} \text{ for } m=1, 3, 5, \dots \text{ and } n=1, 3, 5, \dots$$

After using orthonormalized mode shape with multiplier $\sqrt{L_x L_y \frac{3\pi-8}{2\rho\pi}}$, modal force can be expressed as

$$N = \sum_m \sum_n \frac{-4\sqrt{2}j\sqrt{L_x L_y} P_a \sigma \delta \epsilon_{mn}^2}{\pi^4 \sqrt{\frac{3\pi-8}{\pi}} m^2 n^2 \sqrt{\rho} \left(\frac{m^2\pi^2}{4L_x^2} + \frac{n^2\pi^2}{L_y^2} + j\sigma\right)} \quad (5.32)$$

5.3.5 Case: CFFC

Considering the same plate as in FFFC case, but with the clamped edge at $y = 0$, the nondimensional pressure a_1 is

$$a_1(x, y) = \sum_m^{\infty} \sum_n^{\infty} \frac{-j\sigma\delta\epsilon_m\epsilon_n}{\pi^2 mn \left(\frac{m^2\pi^2}{4L_x^2} + \frac{n^2\pi^2}{4L_y^2} + j\sigma \right)} \cos \frac{m\pi x}{2L_x} \cos \frac{\pi ny}{2L_y} \quad (5.33)$$

where

$$\epsilon_m = \begin{cases} \frac{\pi-4}{4} & m=1 \\ (-1)^{\frac{m+1}{2}} & m>1 \end{cases} \text{ and } \epsilon_n = \begin{cases} \frac{\pi-4}{4} & n=1 \\ (-1)^{\frac{n+1}{2}} & n>1 \end{cases} \text{ for } m=1,3,5,\dots \text{ and } n=1,3,5,\dots$$

Modal force can be obtained after using the orthonormalized mode shape with multiplier $\frac{3\pi-8}{2}\sqrt{\frac{L_x L_y}{\rho\pi}}$ as

$$N = \sum_m^{\infty} \sum_n^{\infty} \frac{-32j\sqrt{L_x L_y} P_a \sigma \delta \epsilon_m^2 \epsilon_n^2}{\pi^3 (3\pi-8) m^2 n^2 \sqrt{\rho} \left(\frac{m^2\pi^2}{4L_x^2} + \frac{n^2\pi^2}{L_y^2} + j\sigma \right)} \quad (5.34)$$

5.4 Comparison of cases

5.4.1 Linear (First harmonic) comparisons

In this section, the pressure values and modal forces are compared for a square plate $L_x = L_y = 1m$, considering the orthonormalized mode shapes. One should divide the mode shapes with its multiplier to replicate the following results. The real and imaginary components of each modal force are plotted in Figure 5.1 and 5.2 as functions of the squeeze number σ defined by equation (3.11) and compared with the solution of Darling et al. [23] in which deflection is taken as uniform. While calculating the complex resistance force using Darling's formula, the total mode deflection is used as the uniform deflection amplitude. The mass density per unit area ρ is selected as $1kg/m^2$ in order to compare with the literature results. Moreover, the frequency shift and the damping ratio are also evaluated and plotted in Figure 5.3 for each case using Eqs. (5.19) and (5.20) considering ω is changed inside Eq. (3.11). The other parameters used in the calculations are

$$P_a = 100 \frac{kN}{m^2}, \quad \mu = 2 \times 10^{-5} \frac{Ns}{m^2}, \quad h_0 = 0.1mm \quad (5.35)$$

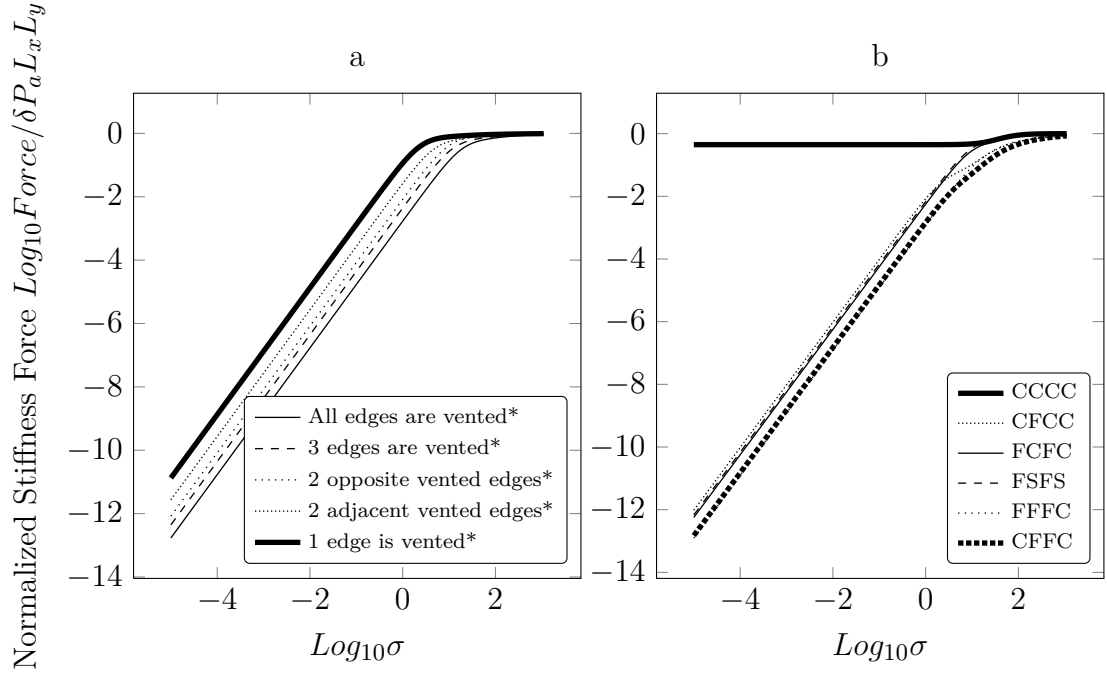


Figure 5.1: Normalized spring force for different boundary conditions of a square plate. (a) constant uniform deflection obtained by Darling et al. [23], (b) present study.

and $\sigma = \frac{\omega}{4} s / m^2$. The modified Reynolds number for the examples are $Re^* = \sigma / 400$, which validates the results up to $\sigma = 400 m^{-2}$ (2.6 in the Log scale).

The normalized stiffness force for different boundary conditions are presented with the literature results [23] in Figure 5.1. It is interesting to note that the stiffness force converges to 0.45 for the CCCC case and goes to 1 where the theoretical limit for high σ values. Figure 5.1(b) depicts that the normalized stiffness force remains constant for CCCC unlike vented cases, while vibration frequency ω is decreasing. This trend is clearly the same as in Figure 5.1(a) and the order of ventilation cases are the same. For the vented cases, the low frequency force exhibits a directly proportional relationship in the Log-Log scale and the following relationship can be extracted

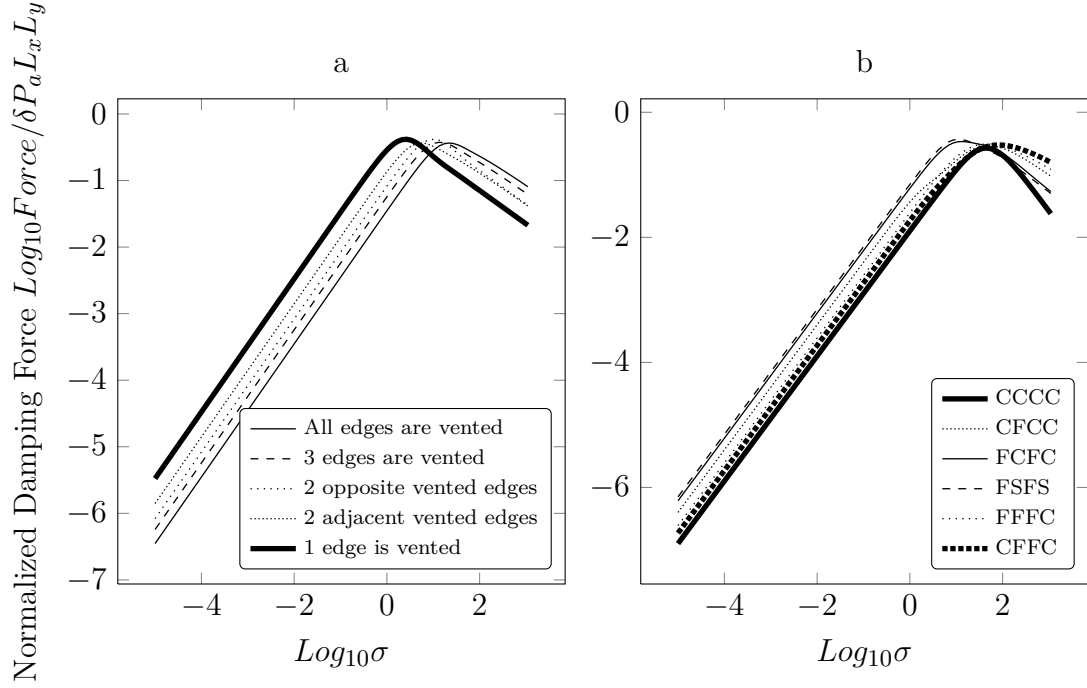


Figure 5.2: Normalized damping force for different boundary conditions of a square plate. (a) constant uniform deflection obtained by Darling et al. [23], (b) present study.

$$\log_{10} \frac{\text{Stiffness Force}}{\delta P_a L_x L_y} \simeq \log_{10} \sigma^2 \quad (5.36)$$

The normalized damping force for both the literature results [23] and the present study results are shown in Figure 5.2. It is observable that the damping force increases proportionally with σ values up to a maximum level then decreases gradually. The decreasing trend for the realistic cases in Figure 5.2(b) is not the same as for the uniform deflection case Figure 5.2(a) which is obtained from Darling et al.'s study [23]. However, the increasing trend in Figure 5.2(a) is nearly the same as in Figure 5.2(b).

The effects of ω and/or σ on the frequency shift and damping ratio can be seen in

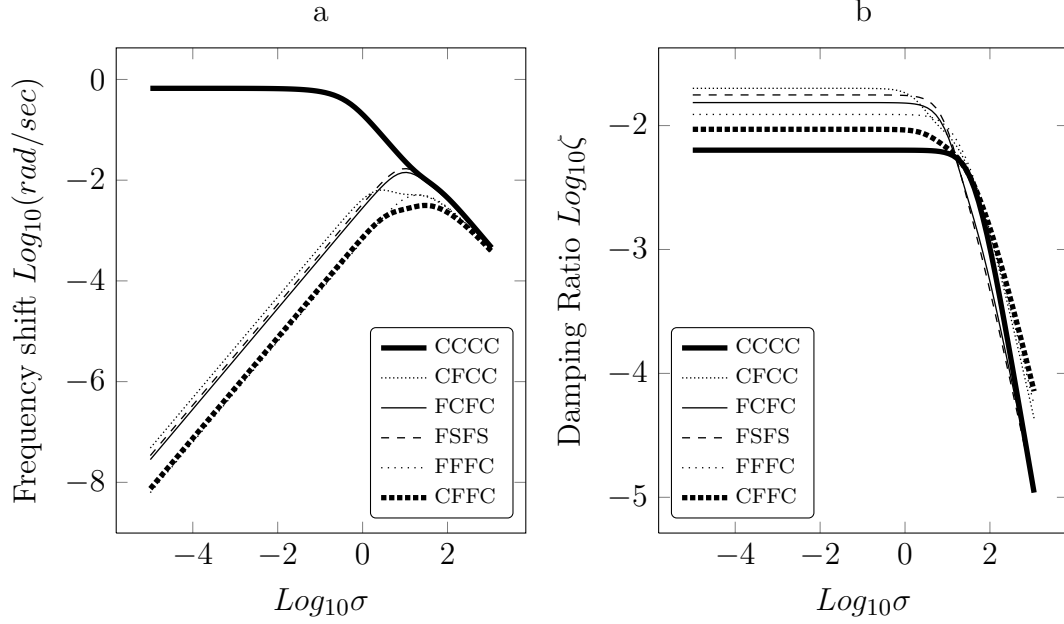


Figure 5.3: Frequency shift (a) and damping ratio (b) for various boundary conditions of the square plate

Figure 5.3. A Log axis is selected in order to capture the effects. Notice that the plate mode shape is assumed unchanged during the calculations of the frequency shift and damping ratio. It is interesting to point out that for all cases except the CCCC case, the frequency shift is directly proportional with σ for low values and inversely proportional for high values of σ . Since the stiffness or the real part of the reaction force reaches to steady state of which the impact of frequency shift is reduced. Moreover, unlike vented cases such as CFCC, FCFC, etc. the frequency shift of CCCC is constant up to $\sigma \approx 0.01\text{m}^{-2}$. For high values of σ air underneath the plate is getting squeezed, instead of escaping through boundaries which are open to ambient pressure. This phenomenon can also be seen in the damping ratio graph. For very small values of σ , the damping ratio stays constant, which means most of the air can be pumped unlike for high frequencies, at which the pumping effect is reduced and damping is said to be inversely proportional with frequency. These damping evaluations can also be used for the statistical energy analysis purposes under parabolic flow restriction.

The comparison between the viscothermal model [33] and the present study is

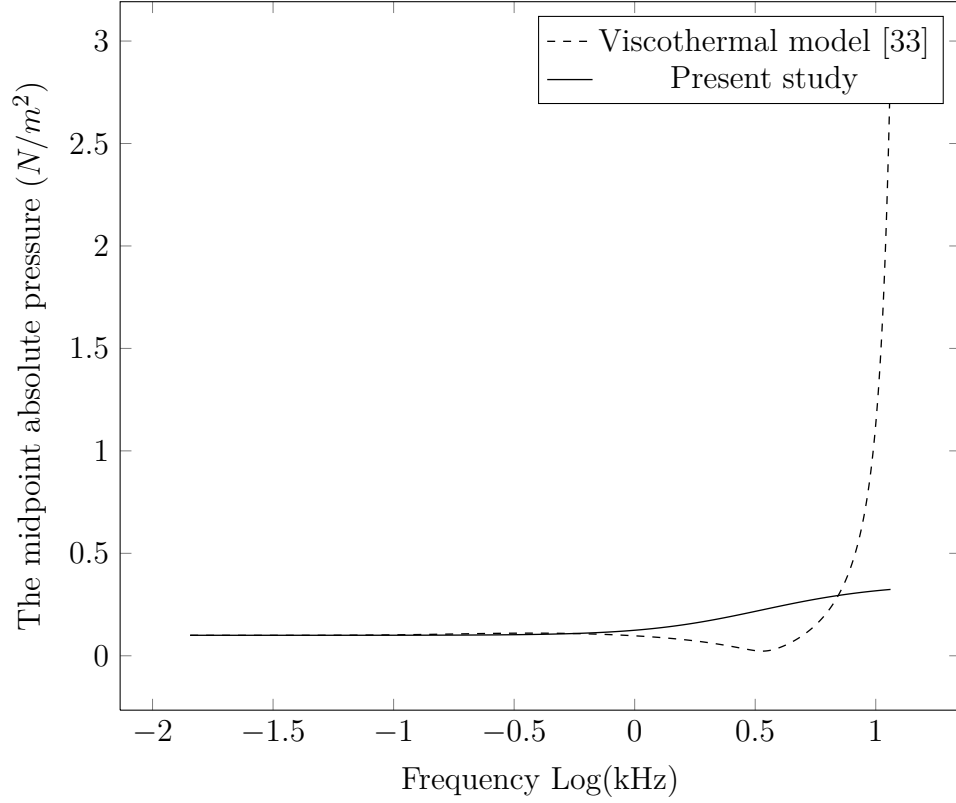


Figure 5.4: The midpoint ($x, y = 0.5m$) absolute pressure variation

presented in Figure 5.4. The variation of the normalized absolute pressure at the center point of the plate is plotted against frequency.

The pressure calculations become different starting from 100Hz, the Reynolds equation based model presented in this study is no longer capable of producing correct results beyond this frequency.

5.4.2 Nonlinear (Second harmonic) comparisons

The capability of the present analysis is further demonstrated by considering the nonlinear analysis of the plate which has the same physical properties as that specified for the previous linear problem. The three cases CCCC, CFCC, and

FCFC are investigated. The influence of the nondimensional deflection multiplier δ and σ on the total amount of force of the first and second harmonics are illustrated in Figure 5.5. The isopleth map is used to show the total force acting on the plate. As shown in Figure 5.5, the effect of the deflection δ on the total force is rather significant. When the σ values are low, the real part of the linear solution Figure 5.5(a) is proportionally increasing with increasing δ . The real part of the total force tends to shift for higher values of σ . The real part of the first harmonic total force is nearly directly proportional with the δ in the σ range investigated. However, the real part of the total force due to the second harmonic $Re(Fa_2)$, presents a different distribution. $Re(Fa_2)$ is nearly directly proportional with δ for high values of σ , but nearly constant for the lower values. It can be concluded that the nonlinearity of the real part of the total force is rather important for the high values of σ for this case. This phenomenon can also be observed on the imaginary part. Moreover, the optimal damping force of the first and second harmonics in Figure 5.5(b,d), can be achieved by adjusting the σ values around $50m^{-2}$.

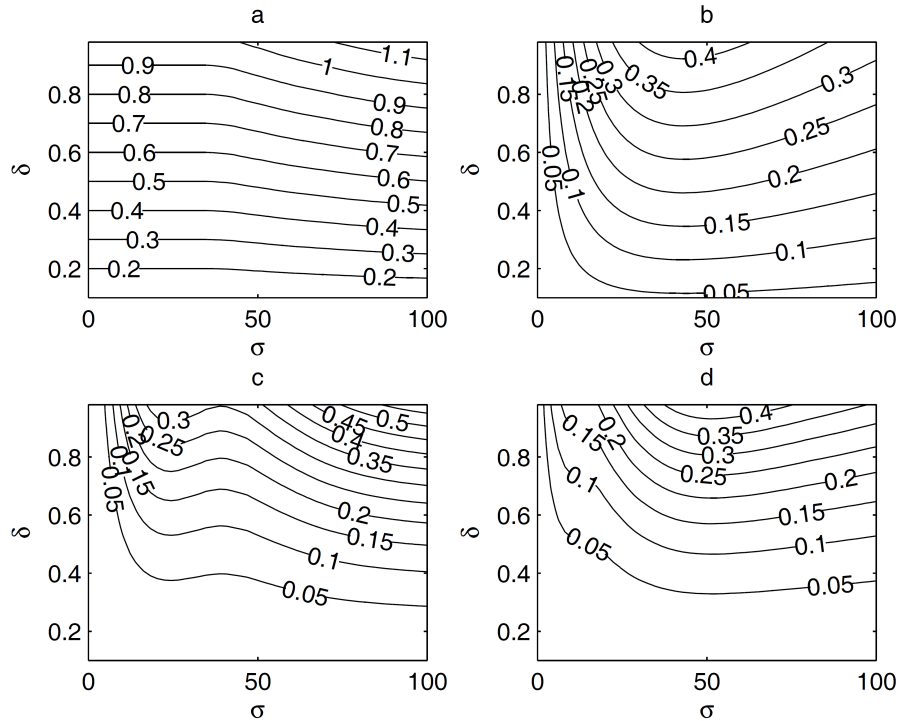


Figure 5.5: Total force acting to the plate for CCCC case, real part of $a_1 = Re(a_1)$ (a), imaginary part of $a_1 = Im(a_1)$ (b), $Re(a_2)$ (c), $Im(a_2)$ (d)

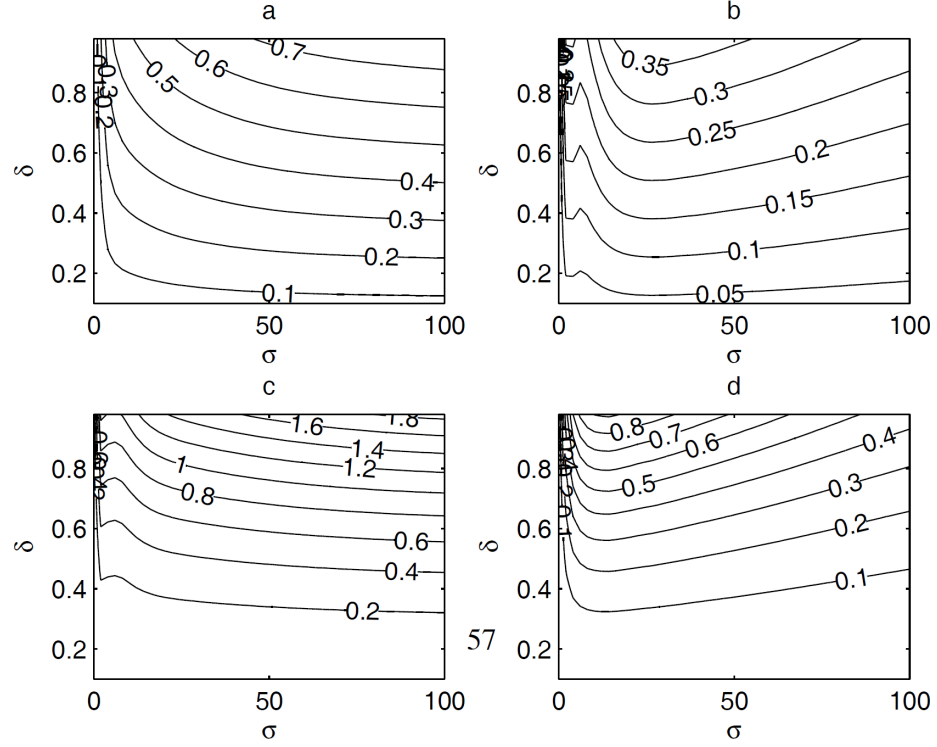


Figure 5.6: Total force acting to the plate for CFCC case, $Re(a_1)$ (a), $Im(a_1)$ (b), $Re(a_2)$ (c), $Im(a_2)$ (d)

The plate with CFCC boundary conditions shows different contour lines in Figure 5.6. In this case, $Re(Fa_1)$ and $Re(Fa_2)$ show similar contour profiles except the magnitudes of the contours. The increase of the second harmonic force $Re(Fa_2)$, is more than that of the $Re(Fa_1)$ for high σ values. The imaginary parts $Im(Fa_1)$ and $Im(Fa_2)$ exhibit local extrema around $\sigma = 10m^{-2}$ and gradually increase for high values of σ . Unlike in the CCCC case, the stiffness and the damping force increase of the second harmonic due to high values of δ is more than the increase of the first harmonic. It can therefore be concluded, that the nonlinearity is more severe than that in the CCCC case.

The results of the plate with FCFC boundary conditions are presented in Figure 5.7. The real forces $Re(Fa_1)$ and $Re(Fa_2)$, show similar contour profiles but the

amplitudes of the contours are different as in the previous case. However, the stiffness force nonlinearity is lower compared to the CFCC case. This can also be observed in the damping forces in Figure 5.7(b,d).

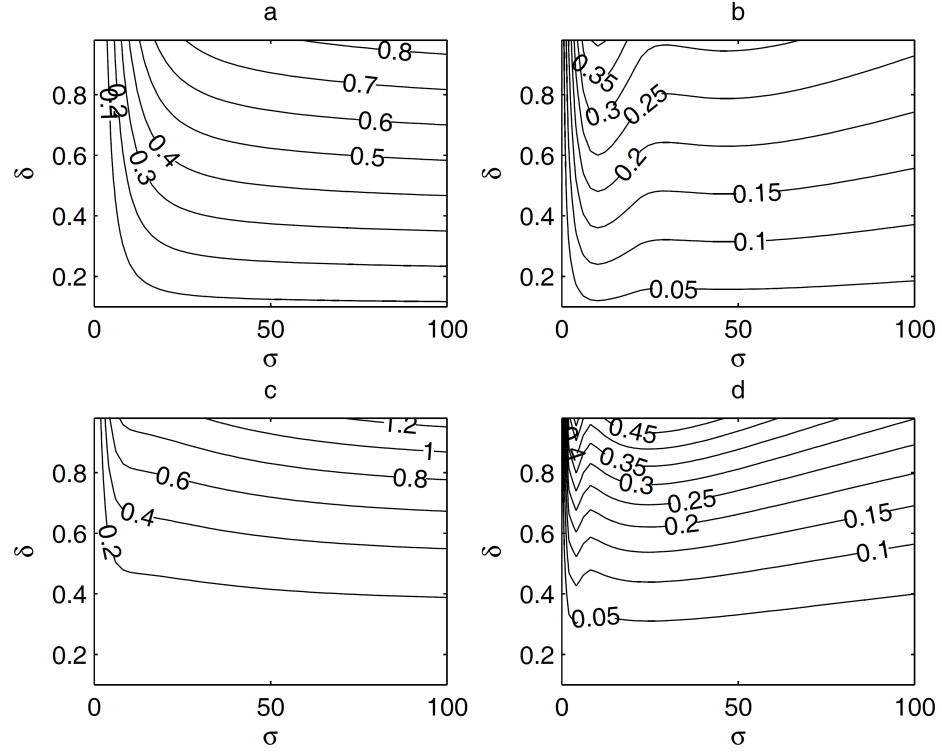


Figure 5.7: Total force acting to the plate for FCFC case, $Re(a_1)$ (a), $Im(a_1)$ (b), $Re(a_2)$ (c), $Im(a_2)$ (d)

6 Experimental investigation of SFD

In this section, experimental investigation of squeeze film dampers are presented. Many experiments are designed from vibration and noise perspective and carried out in the Modal laboratory of Department of Mechanical Engineering-Engineering Mechanics in Michigan Technological University. This section is partitioned into three sections, correlation of SFD modeling with vibrational experiments, nonlinear investigation of SFD performance and the comparison of SFD against viscoelastic dampers.

In order to validate current approach to model the SFD, a rectangular plate attached to a main plate which simulates the main structure is selected as a reference problem (Figure 6.1). Suppose that a machine has a surface, needs to be treated to minimize vibration or noise generated by the machine.

The acceleration and the velocity are measured on the plate using accelerometers at various locations to get the surface vibration behavior. Since it is easier to find damping at natural frequencies of the main structure, the resonance frequencies are selected as driving frequencies.

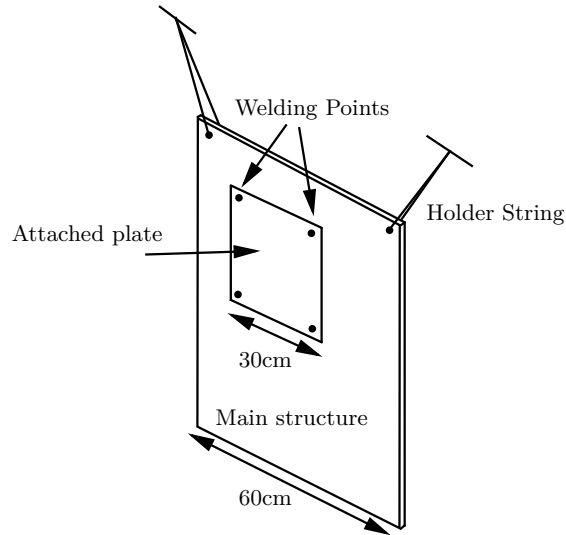


Figure 6.1: Reference problem experimental setup

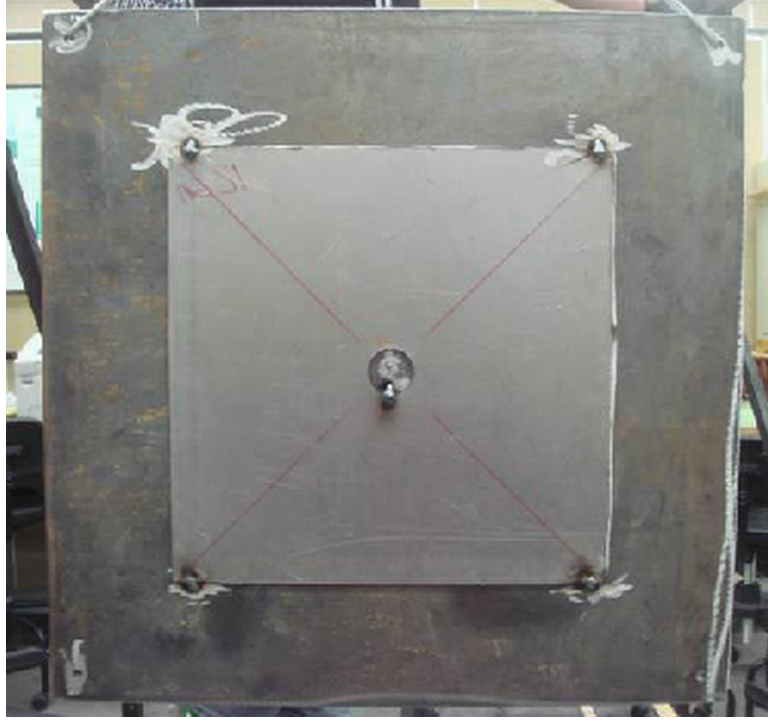


Figure 6.2: Physical plate with welded attached plate

The attached plate is selected to have 30x30cm edges and welded to the main plate which has 60x60cm edge lengths as shown in Figure 6.2. Moreover, 1mm thick rectangular neodymium magnets [76] are used to put a gap of 1mm precisely. However, a flat surface is difficult to obtain due to the initial curvature of the attached plates.

6.1 Correlation of FEA model

The effectiveness of the SFD is tested as the first experiment. Two different boundary configurations for the attached plate are considered, plate attached at four corner points and plate attached at the center only. The attached plate is placed at the center of the main structure. The experiment is carried out using a shaker and PCB [77] accelerometers (Type 352C65). The experiments showed (Figure

Table 6.1

Comparison of simulation and experiment for corner and center supported SFD plate

Mode No	Simulation (Hz)	Experiment (Hz)
1	37.16 (4.78%)	36.25 (4.63%)
2	41.28 (3.17%)	40.74 (3.23%)
3	49.84 (3.04%)	51.59 (3.67%)
4	63.31 (0.41%)	64.13 (0.37%)
5	73.26 (0.55%)	75.57 (0.61%)

6.3) that for the selected natural frequencies, the plate attached at the center reduces the acceleration magnitudes about 18 dB which is better than the reduction obtained from plate attached at corners. However, no reduction effect is observed for the 213Hz. This example shows the importance of the design of the attached plate. Another important issue is the shift of the natural frequencies, this is positive for 233Hz, negative or zero for the others. The negative shift corresponds to mass loading which is neglected at the analysis stage on the natural frequency.

The additional stiffness originated from fluid film can also be seen in third mode apparently. The time domain data for the damped case and undamped case explains the basic features of the squeeze film damping effect. For large displacements the damping is proportional with 3rd order of displacement, however for small displacements the damping is said to be proportional with velocity of the plate.

Another vibration experiment is designed with neodymium magnets which give better control on the gap thickness. In this experiment, the plate is supported from corners with magnets. Moreover, another magnet is put to the center of the plate due to the rattling of the plate center during experiments.

The simulation results as well as experimental results are shown at Table 6.1.

The results show that the simulation is well representing the experiments. However, a modal updating can be done in order to get better FEM models. First two mode shapes as well as pressure distribution under the plates can be seen in Figure 6.4.

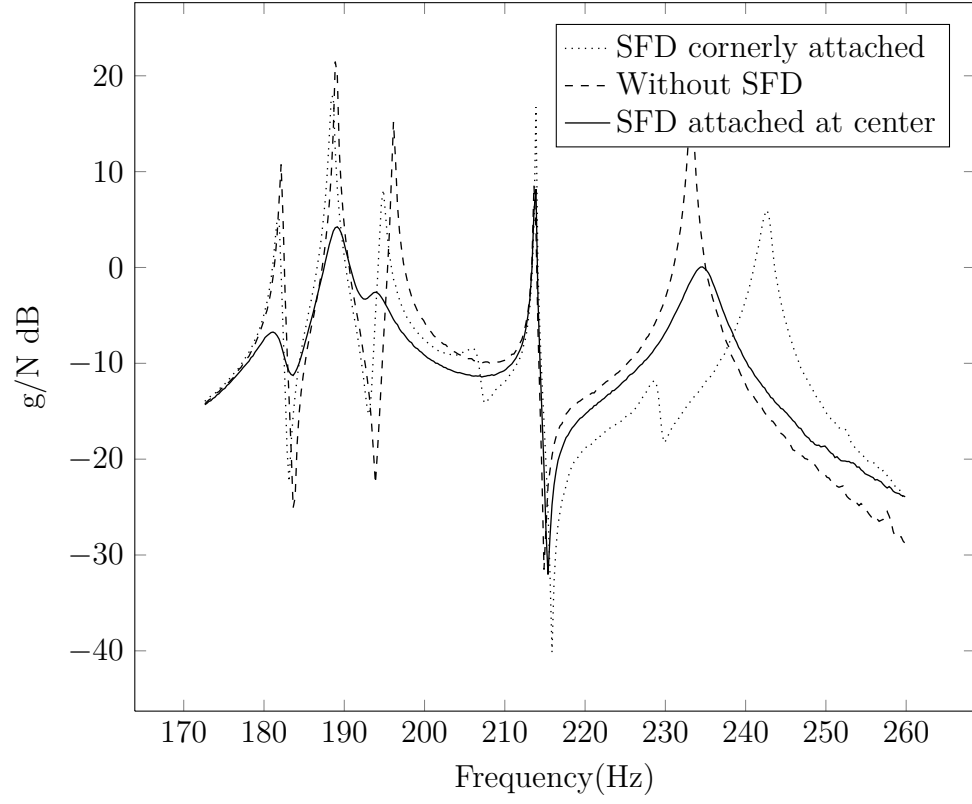


Figure 6.3: Comparison of frequency response functions

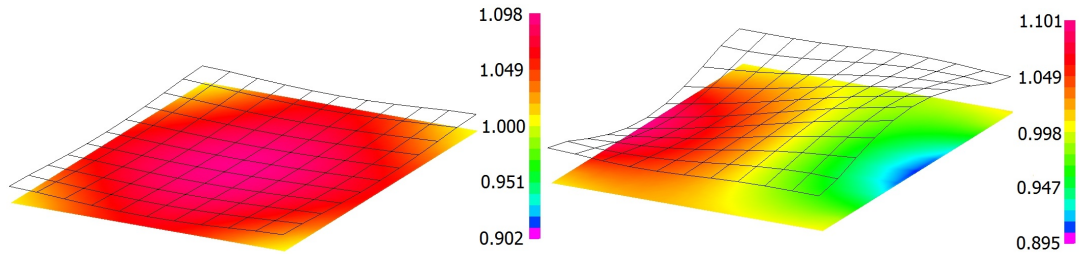


Figure 6.4: First (left), second modes (right) and normalized pressure distribution underneath the plate (p/p_a), where p_a : Ambient Pressure = 101325 N/m^2)

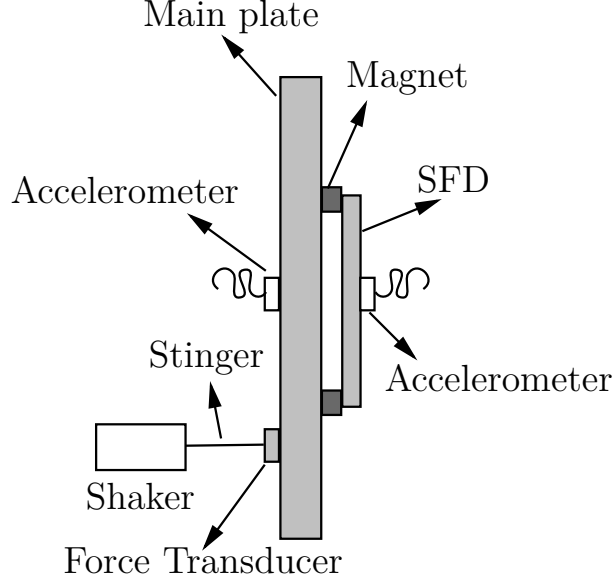


Figure 6.5: Experimental setup

6.2 Nonlinear region

The nonlinear response of SFD is investigated using the previous experimental setup used in linear analysis. A sketch of the experimental setup can be seen in Figure 6.5. The shaker (Modal Shop 2025E) used in experiments can produce maximum output force of 57N for sinusoidal excitation.

In this experiment, the center support is removed to allow the plate to vibrate freely around this region in order to increase the sensitivity of the SFD to the vibrational energy input. The damping of the SFD for the first mode (umbrella) with respect to force input level which is measured by force transducer, is investigated. For this purpose, the level of energy flowing through the shaker is controlled by an amplifier. The level of force is controlled and increased step by step, then the vibration level of the SFD and plate are measured simultaneously. The shaker is driven with a sinusoidal signal and the excitation frequency is selected 40Hz in order to avoid electrical ground related problems.

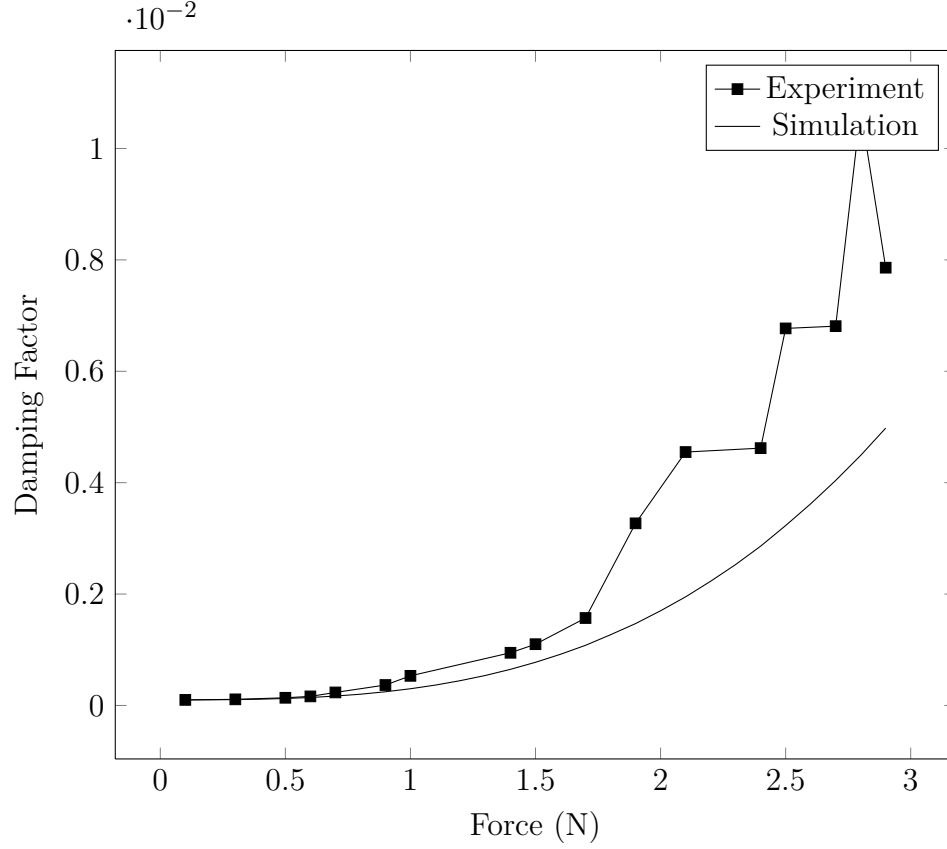


Figure 6.6: Nonlinear response of the square plate exposed to sinusoidal excitation

The measured response is presented in Figure 6.6. As it can be seen from the trend, the damping factor which is calculated based on half power point approach is increasing with the excitation force. The experiment is stopped due to the rattling of the SFD plate due to the sliding of support magnets. The simulation formulation is based on the sum of first and second harmonic damping force calculations based on the derivation in section 5. It can be stated that the damping is nonlinear for and can be approximated with second order calculations approximately. The error tend to be larger with the level of vibration. However, the lower vibration level zone is captured and the results start to deviate around 1N excitation.

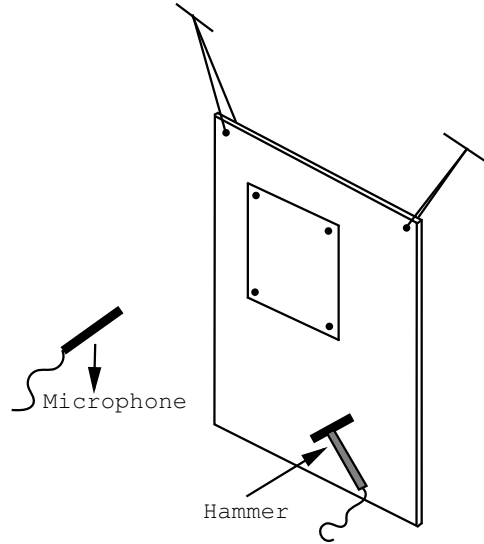


Figure 6.7: Impact noise measurement testing

6.3 SFD against viscoelastic treatments

In this section the squeeze film damper performance is compared against conventional damping treatments. These treatments include spectrum spray which is a polymer spray that converts vibratory energy into heat energy via shear stress dissipation, and viscoelastic damper. Using four different cases,

- Untreated plate
- Viscoelastic film (Spectrum spray)
- Viscoelastic damper (Isodamp C-2003)
- Squeeze film damper (1mm gap)

the damping levels are compared using an impact to excite the plate. The resulting vibration related noise is measured with a microphone which is shown in Figure 6.7.

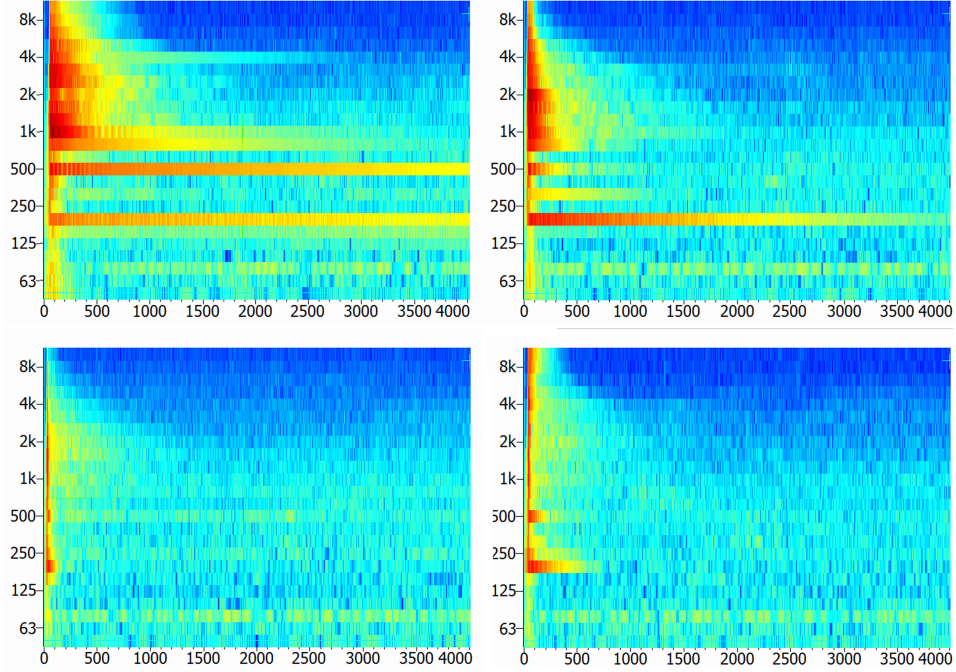


Figure 6.8: Comparison of SFD against viscoelastic damping treatments (Topleft: untreated plate, toprigh: viscoelastic film, bottomleft: viscoelastic damper, bottomright:SFD)

The experiment results are presented in Figure 6.8 using specgrams. The effectivity of SFD is close to the viscoelasticly treated plate with 1mm gap and is better and the viscoelastic film damping treatment. The damping levels can be increased using a SFD with larger surface area or lower gap thickness. However, there could be a problem due to the clashing of two surfaces in later case.

7 Conclusions and future work

Almost every structure undergoes fluid loading effects which alter their dynamic behavior. In MEMS, the presence of fluid loading could be dominant and prevents the structure to operate. The effects of the fluid loading should be determined in advance to prevent any irreversible effect on the structure. One of the famous examples is the Tacoma Narrows bridge which is a pair of twin suspension bridges in the U.S. state of Washington. The Tacoma Narrows bridge collapsed four months later after opening due to excessive vibrations which were created by wind gusts. In this study, theoretical investigation of squeeze film effects on dimensionally reducible structures is investigated.

The previous sections have outlined the effects of fluid loading on two dimensional structures. It has been shown that the fluid film can be a very important parameter on the dynamic behavior of vibrating structures. The stiffness, damping and mass loading effects are the resulting effects of the fluid film. The conclusions can be summarized as follows

- In linear regime, the coupled vibrations of Kirchhoff plates with squeeze fluid film can be solved by using boundary characteristic orthogonal polynomials used for both fluid and structure domains. The coupled vibration equations of skew plates are based on the two nondimensional parameters ϵ and κ which affect the solution directly. Several cases of rectangular plates and two cases of skew plates are investigated. The damped eigenvalues related to the structure are obtained by using the determinant property of partitioned matrices. These examples can be taken to further considering elliptical or more complex geometries which could be beneficial. In conclusion, the present linear coupled analysis provides an efficient and robust technique to obtain the eigenvalues of skew and rectangular plates coupled with squeeze fluid films which are governed by linearized isothermal Reynolds equation.
- In order to extend the prior efforts for simple geometries, the effects of squeeze film damping for complex shaped structures which undergo transversal motion have been investigated secondly. An isoparametric finite element model for two dimensional Reissner-Mindlin plate theory coupled with isothermal

Reynolds equation is developed. The two way coupling is provided using boundary forces, and structural velocities on the boundary. The derivation of numerical model using four noded isoparametric finite elements which is capable of modeling both structural and fluid domain is presented. An alternative solution method to the calculation of coupled eigenvalues and eigenvectors is demonstrated. The effects of fluid film thickness, ambient pressure and fluid viscosity on the frequency response function are investigated using given examples and it has been shown that the influence of the fluid film thickness on the damping is dependent upon the structural mode shape. It is observed that the ambient pressure has no significant direct effect on the frequency responses whereas it is an important factor on the damping force of MEMS systems. However, since the change in the ambient pressure effects the other parameters such as viscosity, density and speed of sound, the effect of nondimensional parameters should be recalculated based on these change before any judgment. However, in general the drop in ambient pressure decreases the loading effect on the structure. A condenser type microphone is investigated to expose the fluid which is trapped between the diaphragm and backplate. The drop on the usable frequency range is obtained. The finite element matrix formulation for the partial coverage SFDs is derived and the determination of the optimal connection point locations for the partial coverage SFDs is discussed.

- The nonlinear regime of Reynolds equation is investigated further as the next logical step after investigation of linear regime. Compact analytical models for computing the effects of compressible SFD are developed using Green's function approach in order to calculate pressure distribution as well as damping ratio and frequency shift. The presented Green's function approach allows rapid calculation of reaction forces using infinite series which includes expansion of approximate mode shapes on eigenfunctions. Truncation of infinite series to first few terms can also be represented, which is useful for system simulations. Several tabulated examples can be expandable to cover more complicated and higher mode shapes. In conclusion, the present Green's function analysis provides an efficient and rapid technique for investigating the nonlinear effects of SFD on rectangular elastic plates.

Moreover, it also provides a powerful, compact and convenient tool to identify the modal damping and frequency shift as well as pressure distribution underneath plates in practice considering that the structure modes remain unaffected by fluid loading.

- The experimental validation of proposed approaches mentioned before is done using in-house experiments as well as the experiments done in literature. It has been shown that the proposed methods can represent the experimental dynamic behavior both in linear and nonlinear regimes. Moreover, the comparison of squeeze film dampers against conventional dampers are presented. It is concluded that the squeeze film dampers are as capable as viscoelastic dampers in terms of vibration suppression and noise abatement. And they're superior due to their usage in harsh environments such as elevated temperature and toxic environments.

The future work as the continuation of the present analysis can be listed as

- The limitations of Reynolds equation can be lifted or extended by considering viscothermal effects. Since viscothermal model can be reduced to Reynolds equation for low frequencies, the half of the extension work can be thought of completed.
- Another important contribution to this field can be the investigation of fully coupled fluid-structure equation considering nonlinear Reynolds equation. This extension can bring the understanding of nonlinear effects to another level since it will consider full coupling.
- Consideration of nonparallel fluid film thickness can extend the current approach to nonuniform thicknesses.
- Another interesting theoretical extension can be the investigation of squeeze film damping in rotating and accelerating frames, which enables to analyze the effects of squeeze film dampers in helicopter, compressor or turbine blades.
- Acoustical response away from the SFD can be calculated using the vibration of the SFD surface as the input to the non-homogeneous Helmholtz equation.

References

- [1] C. Massalas, Thermoelastic vibrations of a semi-infinite strip, *Journal of Sound and Vibration* **104** (1986) 337–341.
- [2] M. Ishimoto, H. Numakura, M. Wuttig, Magnetoelastic damping in Fe-Ga solid-solution alloys, *Materials Science and Engineering: A* **442** (2006) 195–198. Proceedings of the 14th International Conference on Internal Friction and Mechanical Spectroscopy.
- [3] A. Nashif, D. Jones, J. Henderson, Vibration damping, John Wiley and Sons, New York, 1985.
- [4] M. Louroza, N. Roitman, C. Magluta, Vibration reduction using passive absorption system with Coulomb damping, *Mechanical Systems and Signal Processing* **19** (2005) 537–549.
- [5] T. Koizumi, Y. Saito, The damping capacity of a flat surface to roller contact, *Wear* **63** (1980) 347–357.
- [6] W. Beltman, Viscothermal wave propagation including acousto-elastic interaction, part I: theory, *Journal of Sound and Vibration* **227** (1999) 555–586.
- [7] R. Mangiarotty, Acoustic radiation damping of vibrating structures, *The Journal of the Acoustical Society of America* **35** (1963) 369–377.
- [8] H. Sodano, J. Bae, D. Inman, W. Belvin, Improved concept and model of Eddy current damper, *Journal of Vibration and Acoustics* **128** (2006) 294–302.
- [9] M. Bicak, H. Belek, A. Goksenli, Vibration damping of a new ionic liquid under electric field effect, *Acta Polytechnica* **45** (2005) 68–72.
- [10] L. Nikitin, R. Talipov, A. Kazakov, G. Stepanov, Mechanical and magnetic properties of polydisperse magnetoelastics, *Solid State Phenomena* **152-153** (2009) 155–158.
- [11] V. Noresson, N. Ohlson, M. Nilsson, Design of electrorheological dampers by means of finite element analysis: theory and applications, *Materials and Design* **23** (2002) 361–369.

- [12] C. Spelta, F. Previdi, S. Savaresi, G. Fraternale, N. Gaudio, Control of magnetorheological dampers for vibration reduction in a washing machine, *Mechatronics* **19** (2009) 410–421.
- [13] K. Lee, K. Park, Optimal robust control of a contactless brake system using an Eddy current, *Mechatronics* **9** (1999) 615–631.
- [14] Audi A1 project quattro available from, <http://audiusa.com/>, 2011.
- [15] N. Hoang, Y. Fujino, P. Warnitchai, Optimal tuned mass damper for seismic applications and practical design formulas, *Engineering Structures* **30** (2008) 707–715.
- [16] F. Ricciardelli, A. Occhiuzzi, P. Clemente, Semi-active tuned mass damper control strategy for wind-excited structures, *Journal of Wind Engineering and Industrial Aerodynamics* **88** (2000) 57–74.
- [17] T. Wakahara, T. Ohyama, K. Fujii, Suppression of wind-induced vibration of a tall building using tuned liquid damper, *Journal of Wind Engineering and Industrial Aerodynamics* **43** (1992) 1895–1906.
- [18] J. Ebert, Multi-frequency vibration controller using fluid-filled cantilever beam for vibration excitation & absorption, U.S. Patent No. 4470121, 1981.
- [19] A. Lord, G. Martyn, Vibration damping apparatus for a helicopter rotor system, United Kingdom Patent No. GB2420395A, 2006.
- [20] O. Reynolds, On the theory of lubrication and its application to Mr. Beauchamp Tower’s experiments, including an experimental determination of the viscosity of olive oil, *Philos. Trans. R. Soc.* **177** (1886) 157–234.
- [21] Y. Peter, W. Jung, Single-crystal-silicon continuous membrane deformable mirror array for adaptive optics in space-based telescopes, *IEEE Journal of Selected Topics in Quantum Electronics* **13** (2007) 162–167.
- [22] W. Langlois, Isothermal squeeze films, *Quarterly Applied Mathematics* **20** (1962) 131–150.

- [23] R. Darling, C. Hivick, Compact analytical modeling of squeeze film damping with arbitrary venting conditions using a Green's function approach, *Sensors and Actuators A: Physical* **70** (1998) 32–41.
- [24] M. Bıçak, M. Rao, Analytical modeling of squeeze film damping for rectangular elastic plates using Green's functions, *Journal of Sound and Vibration* **329** (2010) 4617 – 4633.
- [25] H. Yang, M. Bao, Squeeze film air damping in MEMS, *Sensors and Actuators :A Physical* **136** (2007) 3–27.
- [26] J. Starr, Squeeze-film damping in solid-state accelerometers, in: Solid-State Sensor and Actuator Workshop, 4th Technical Digest, IEEE, pp. 44–47.
- [27] A. Stiffer, M. Sadd, Squeeze film dampers: amplitude effects at low squeeze numbers, *J. Eng. Ind. Trans. ASME, Ser. B* **97** (1975) 1366–1370.
- [28] U. Ingard, A. Akay, On the vibration damping of a plate by means of a viscous fluid layer, *ASME Journal of Vibration, Acoustics, Stress and Reliability in Design* **109** (1987) 178–184.
- [29] L. Chow, R. Pinnington, Practical industrial method of increasing structural damping in machinery, I: Squeeze-film damping with air, *Journal of Sound and Vibration* **118** (1987) 123–139.
- [30] G. Maidanik, E. Ungar, Panel loss factors due to gas-pumping at structural joints, 1967.
- [31] T. Onsay, Dynamic interactions between the bending vibrations of a plate and a fluid layer attenuator, *Journal of Sound and Vibration* **178** (1994) 289–313.
- [32] M. Fox, P. Whitton, The damping of structural vibrations by thin gas films, *Journal of Sound and Vibration* **73** (1980) 279–295.
- [33] P. V. der Hoogt, W. Beltman, Implementation and experimental validation of a new viscothermal acoustic finite element for acousto-elastic problems, *Journal of Sound and Vibration* **216** (1998) 159–185.

- [34] T. Basten, P. V. D. Hoogt, On the acousto-elastic behaviour of double-wall panels with a viscothermal air layer, *Journal of Sound and Vibration* **243** (2001) 699–719.
- [35] A. Akrout, L. Hammami, Vibro-acoustic behaviour of laminated double glazing enclosing a viscothermal fluid cavity, *Applied Acoustics* **70** (2009) 82–96.
- [36] C. Lei, R. White, Three-dimensional viscous finite element formulation for acoustic fluid-structure interaction, *Computer Methods in Applied Mechanics and Engineering* **197** (2008) 4160–4172.
- [37] C. Karra, A. Akrout, Viscothermal fluid effects on vibro-acoustic behaviour of double elastic panels, *International Journal of Mechanical Sciences* **50** (2008) 764–773.
- [38] S. Mohite, V. Sonti, R. Pratap, A compact squeeze-film model including inertia, compressibility, and rarefaction effects for perforated 3-D MEMS structures, *Journal of Microelectromechanical Systems* **17** (2008) 709–723.
- [39] A. Pandey, R. Pratap, A comparative study of analytical squeeze film damping models in rigid rectangular perforated MEMS structures with experimental results, *Microfluidics and Nanofluidics* **4** (2008) 205–218. 10.1007/s10404-007-0165-4.
- [40] S. Gabriele, W. Gerhard, Physically based modeling of squeeze film damping by mixed-level system simulation, *Sensors and Actuators A: Physical* **97-98** (2002) 193 – 200.
- [41] A. Lundbladh, S. Berlin, M. Skote, C. Hildings, J. Choi, J. Kim, D. Henningson, An Efficient Spectral Method for Simulation of Incompressible Flow Over a Flat Plate, Technical Report, 1999.
- [42] V. Ostasevicius, R. Dauksevicius, R. Gaidys, A. Palevicius, Numerical analysis of fluid-structure interaction effects on vibrations of cantilever microstructure, *Journal of Sound and Vibration* **308** (2007) 660 – 673. Vibro-Impact Systems.

- [43] T. Veijola, A. Lehtovuori, Numerical and analytical modelling of trapped gas in micromechanical squeeze-film dampers, *Journal of Sound and Vibration* **319** (2009) 606 – 621.
- [44] N. Joly, Finite Element Modeling of Thermoviscous Acoustics on Adapted Anisotropic Meshes: Implementation of the Particle Velocity and Temperature Variation Formulation, *Acta acustica united with acustica* **96** (2010) 102–114.
- [45] GNU Octave, <http://www.octave.org/>, 2010.
- [46] C. Navier, Memoire sur les lois du mouvement des fluides, *Mem. Acad. Sci. Inst. France* **6** (1822) 389–440.
- [47] G. Stokes, On the theories of the internal friction of fluids in motion, *Trans. Cambridge Phil. Soc.* **8** (1845) 287–305.
- [48] L. Arkeryd, On the Boltzmann equation, *Archive for Rational Mechanics and Analysis* **45** (1972) 1–16. 10.1007/BF00253392.
- [49] A. Beskok, G. Karniadakis, W. Trimmer, Rarefaction and compressibility effects in gas microflows, *Journal of Fluids Engineering-Transactions of the ASME* **118** (1996) 448–456.
- [50] M. Knudsen, Die gesetze der molecular stromung und die inneren reibungstromung der gase durch rohren, *Ann. Phys. (Leipzig)* **28** (1909) 75 – 130.
- [51] H. Kuisma, T. Veijola, Equivalent-circuit model of the squeezed gas film in a silicon accelerometer, *Sensors and Actuators A: Physical* **48** (1995) 239–248.
- [52] G. Domoto, Y. Hsia, An experimental investigation of molecular rarefaction effects in gas lubricated bearing at ultra-low clearance, *J. Tribol. Trans. ASME* **105** (1983) 120–130.
- [53] H. Seidel, U. Fritsch, R. Gottinger, G. Schuster, U. Nothelfer, H. Riedel, W. Kupke, R. Voss, Piezoresistive silicon accelerometer for automotive applications, in: Proceedings Sensors, volume **2**, pp. 271–278.
- [54] A. Burgdorfer, The influence of the molecular mean free path on the performance of hydrodynamic gas lubricated bearings, *Journal of Basic Engineering* **81** (1959) 94–99.

- [55] Y. Mitsuya, Modified reynolds equation for ultra-thin film gas lubrication using 1.5-order slip-flow model and considering surface accommodation coefficient, *Journal of Tribology* **115** (1993) 289–294.
- [56] C. Chen, J. Yao, Damping control of MEMS devices using structural design approach, in: Solid state sensors and actuator tech. digest, pp. 72–75.
- [57] S. Fukui, R. Kaneko, Analysis of ultra-thin gas film lubrication based on linearized boltzman equation: first report derivation of a generalized lubrication equation including thermal creep flow, *Journal of Tribology* **110** (1988) 253–262.
- [58] T. Veijola, Gas damping in vibrating MEMS structures, in: Handbook of Silicon Based MEMS Materials and Technologies (First edition), William Andrew Publishing, Boston, first edition edition, 2010, pp. 259 – 279.
- [59] W. Gross, Gas Film Lubrication, John Wiley, New York, 1962.
- [60] G. Kirchhoff, Über das gleichgewicht und die bewegung einer elastischen scheibe, *Crelles J.* **40** (1850) 51–88.
- [61] E. Reissner, The effect of transverse shear deformation on the bending of elastic plates, *Journal of Applied Mechanics* **12** (1945) 69–77.
- [62] R. Mindlin, Influence of rotary inertia and shear on flexural vibrations of isotropic, elastic plates, *Journal of Applied Mechanics* **18** (1951) 31–38.
- [63] J. Reddy, Theory and Analysis of Elastic Plates and Shells, CRC Press, New York, 2006.
- [64] F. Zhu, Rayleigh-Ritz method in coupled fluid-structure interacting systems and its applications, *Journal of Sound and Vibration* **186** (1995) 543–550.
- [65] B. Singh, S. Chakraverty, Flexural vibration of skew plates using boundary characteristic orthogonal polynomials in two variables., *Journal of Sound and Vibration* **173** (1994) 157–178.
- [66] K. Liew, K. Lam, Application of two-dimensional orthogonal plate functions to flexural vibration of skew plates., *Journal of Sound and Vibration* **139** (1990) 241–252.

- [67] R. Bhat, Natural frequencies of rectangular plates using characteristic orthogonal polynomials in Rayleigh-Ritz method., *Journal of Sound and Vibration* **102** (1985) 493–499.
- [68] M. Bicak, M. Rao, Coupled squeeze film analysis by Reissner-Mindlin plate elements., *Journal of Vibration and Control* (2011,(In press)).
- [69] Maxima, a computer algebra system. version 5.18.1, <http://maxima.sourceforge.net/>, 2009.
- [70] R. Taylor, T. Hughes, A simple efficient finite element for plate bending, *Int. J. Num. Meth. Eng.* **12** (1977) 1059–1079.
- [71] Y. Saad, Numerical Methods for Large Eigenvalue Problems, Manchester University Press, Manchester, 1992.
- [72] R. Blevins, Formulas for Natural Frequency and Mode Shape, Van Nostrand Reinhold, New York, 1979.
- [73] C. Tan, J. Miao, Design optimization of condenser microphone: A design of experiment perspective, *The Journal of the Acoustical Society of America* **125** (2009) 3641–3649.
- [74] W. Griffin, H. Richardson, A study of fluid squeeze-film damping, *ASME J. Basic Eng* **0** (1966) 451–456.
- [75] A. Leissa, Vibration of Plates, 1969.
- [76] Neodymium magnets, <http://www.kjmagnetics.com/>, 2011.
- [77] PCB Electronics, Accelerometer 352C65, <http://www.pcb.com/>, 2011.
- [78] A. Ferreira, MATLAB Codes for Finite Element Analysis: Solids and Structures, Springer, New York, 2008.
- [79] R. Lehoucq, D. Sorensen, C. Yang, ARPACK Users Guide: Solution of Large-Scale Eigenvalue Problems with Implicitly Restarted Arnoldi Methods, SIAM, Philadelphia, 1998.

A Appendices

A.1 Exact solutions of coupled rectangular domain

In this section, the exact solutions of coupled rectangular domain are given.

A.1.1 CCCC

Table A.1

Damped eigenvalues for the first mode of square CCCC plate with open boundary conditions (Vacuum : 35.436)

$\log \epsilon \kappa$	$\log \kappa = -5$	-4	-3	-2
-5	35.99	35.99	35.99	35.99
-3	35.99	35.99	35.99	35.99
-1	35.99	35.99	35.99	35.99
1	-0.25 ± 35.99	-0.25 ± 35.99	-0.25 ± 35.99	-0.25 ± 35.99
2	-2.48 ± 35.90	-2.48 ± 35.90	-2.48 ± 35.90	-2.49 ± 35.90
3	-24.91 ± 26.04	-24.92 ± 26.05	-24.97 ± 26.06	-25.55 ± 26.09

Table A.2

Damped eigenvalues for the second mode of CCCC plate with open boundary conditions (Vacuum:72.312)

$\log \epsilon \kappa$	$\log \kappa = -5$	-4	-3	-2
-5	73.40	73.40	73.40	73.40
-3	73.40	73.40	73.40	73.40
-1	73.40	73.40	73.40	73.40
1	$-0.10 \pm 73.40j$	$-0.10 \pm 73.40j$	$-0.10 \pm 73.40j$	$-0.10 \pm 73.40j$
2	$-1.00 \pm 73.39j$	$-1.00 \pm 73.39j$	$-1.00 \pm 73.39j$	-1.00 ± 73.41
3	$-9.98 \pm 72.72j$	$-9.98 \pm 72.73j$	$-9.98 \pm 72.74j$	$-10.02 \pm 72.87j$

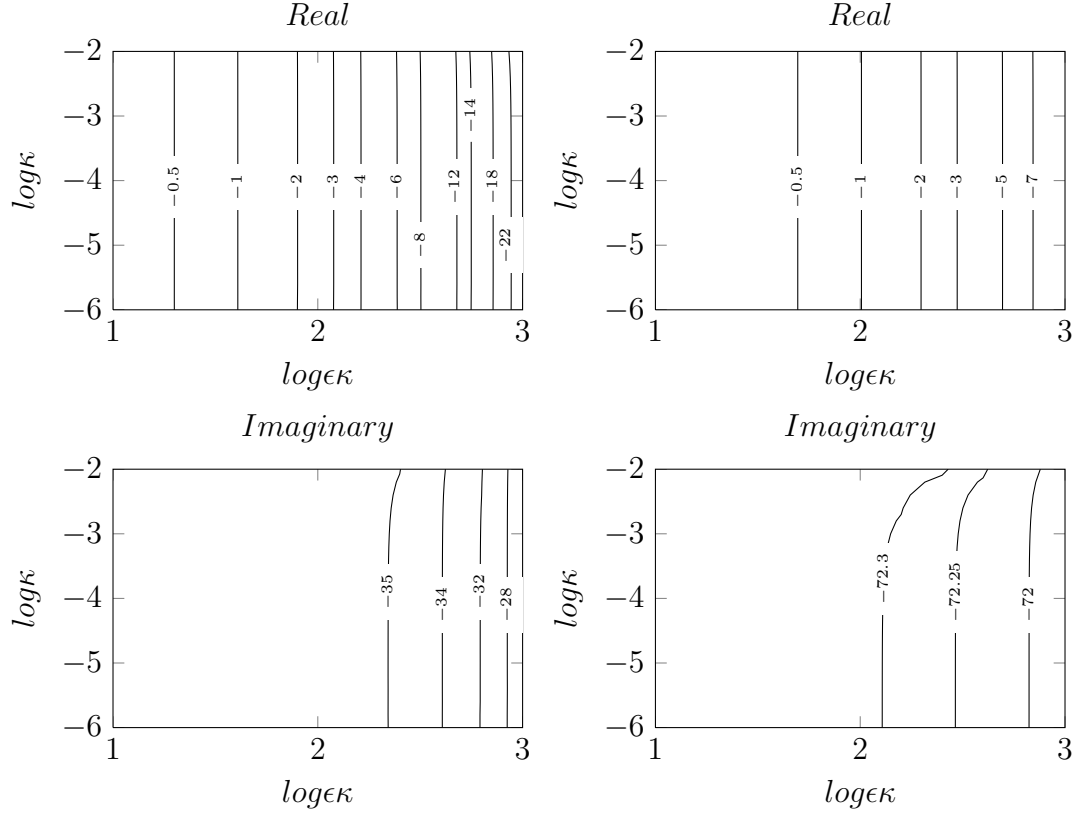


Figure A.1: Real and imaginary parts of the first (left) and second (right) eigenvalues for the rectangular CCCC plate with Dirichlet fluid boundary conditions

A.1.2 CCFC

The eigenvalues of the first two modes for the CCFC plate with closed-closed-open-closed (Neumann-Neumann-Dirichlet-Neumann) fluid boundary are presented at Tables A.3-A.4.

Table A.3

Damped eigenvalues for the first mode of square CCFC plate with closed-closed-open-closed boundary conditions (Vacuum : 23.96)

$\log \epsilon \kappa$	$\log \kappa = -5$	-4	-3	-2
-5	23.91	23.91	23.91	23.91
-3	24.39	23.96	23.91	23.91
-1	27.61	26.29	24.39	23.96
1	$-0.01 \pm 27.84j$	$-0.01 \pm 27.82j$	$-0.01 \pm 27.61j$	$-0.02 \pm 26.29j$
2	$-0.11 \pm 27.84j$	$-0.11 \pm 27.84j$	$-0.11 \pm 27.82j$	$-0.12 \pm 27.62j$
3	-1.00 ± 28.15	-1.00 ± 28.15	-1.00 ± 28.15	-1.00 ± 28.15

Table A.4

Damped eigenvalues for the second mode of CCFC plate with closed-closed-open-closed boundary conditions (Vacuum:40.02)

$\log \epsilon \kappa$	$\log \kappa = -5$	-4	-3	-2
-5	39.42	39.41	39.41	39.41
-3	40.62	39.53	39.42	39.41
-1	71.23	50.83	40.62	39.53
1	$-0.23 \pm 72.49j$	$-0.23 \pm 72.40j$	$-0.24 \pm 71.23j$	$-0.08 \pm 50.83j$
2	$-2.35 \pm 72.49j$	$-2.35 \pm 72.49j$	$-2.35 \pm 72.42j$	$-2.38 \pm 71.41j$
3	$-26.70 \pm 72.07j$	$-26.72 \pm 72.10j$	$-26.79 \pm 72.39j$	$-26.72 \pm 75.59j$

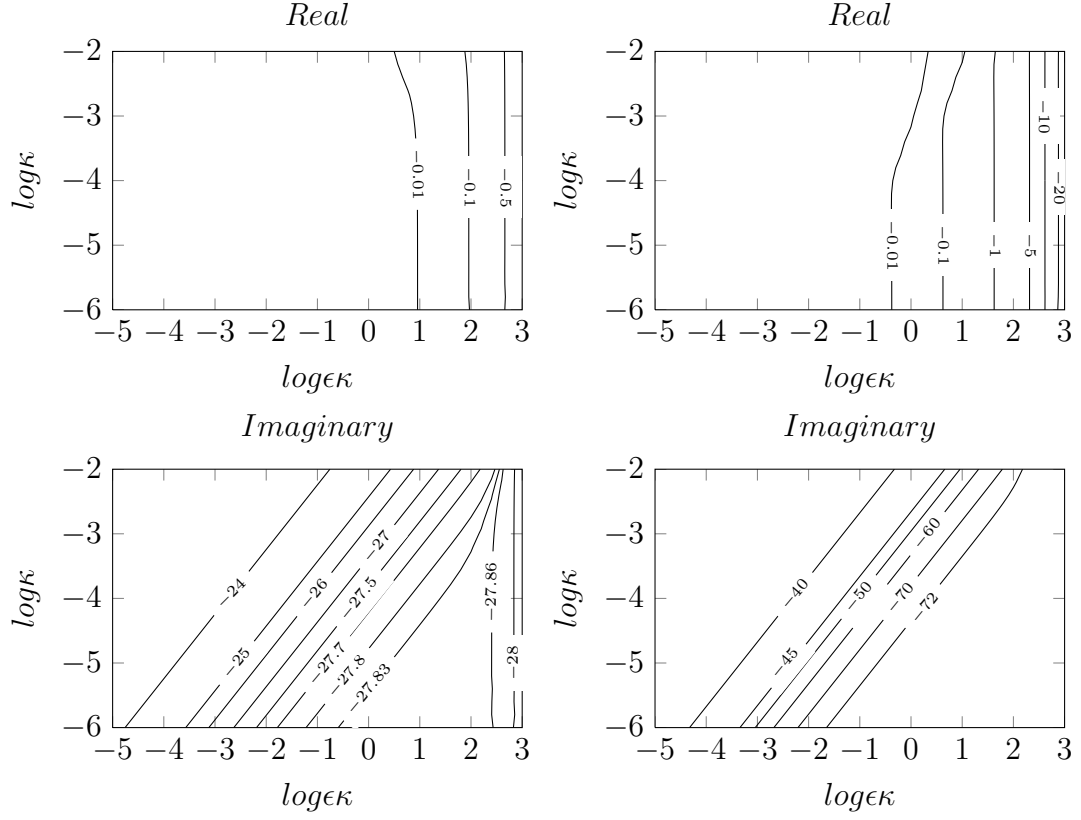


Figure A.2: Real and imaginary parts of the first and second eigenvalues for the rectangular CFCC plate

A.1.3 CCFF

The eigenvalues of the first two modes for the CCFF plate with closed-closed-open-open (Neumann-Neumann-Dirichlet-Dirichlet) fluid boundary are presented at Tables A.5-A.6.

Table A.5

Damped eigenvalues for the first mode of square CFCF plate with closed-open-closed-open boundary conditions (Vacuum : 22.223)

$\log \epsilon \kappa$	$\log \kappa = -5$	-4	-3	-2
-5	22.37	22.37	22.37	22.37
-3	22.37	22.37	22.37	22.37
-1	22.37	22.37	22.37	22.37
1	$-0.32 \pm 22.37j$	$-0.32 \pm 22.37j$	$-0.32 \pm 22.37j$	$-0.32 \pm 22.38j$
2	$-3.20 \pm 22.17j$	$-3.20 \pm 22.17j$	$-3.21 \pm 22.18j$	$-3.22 \pm 22.24j$
3	$-8.79 \pm 0.00j$	$-8.79 \pm 0.00j$	$-8.78 \pm 0.00j$	$-8.69 \pm 0.00j$

Table A.6

Damped eigenvalues for the second mode of square CFCF plate with closed-open-closed-open boundary conditions (Vacuum : 26.556)

$\log \epsilon \kappa$	$\log \kappa = -5$	-4	-3	-2
-5	26.52	26.52	26.52	26.52
-3	26.52	26.52	26.52	26.52
-1	26.52	26.52	26.52	26.52
1	$-0.07 \pm 26.52j$	$-0.07 \pm 26.52j$	$-0.07 \pm 26.52j$	$-0.07 \pm 26.52j$
2	$-0.70 \pm 26.51j$	$-0.70 \pm 26.51j$	$-0.70 \pm 26.51j$	$-0.70 \pm 26.51j$
3	$-7.06 \pm 25.63j$	$-7.06 \pm 25.63j$	$-7.07 \pm 25.63j$	$-7.08 \pm 25.66j$

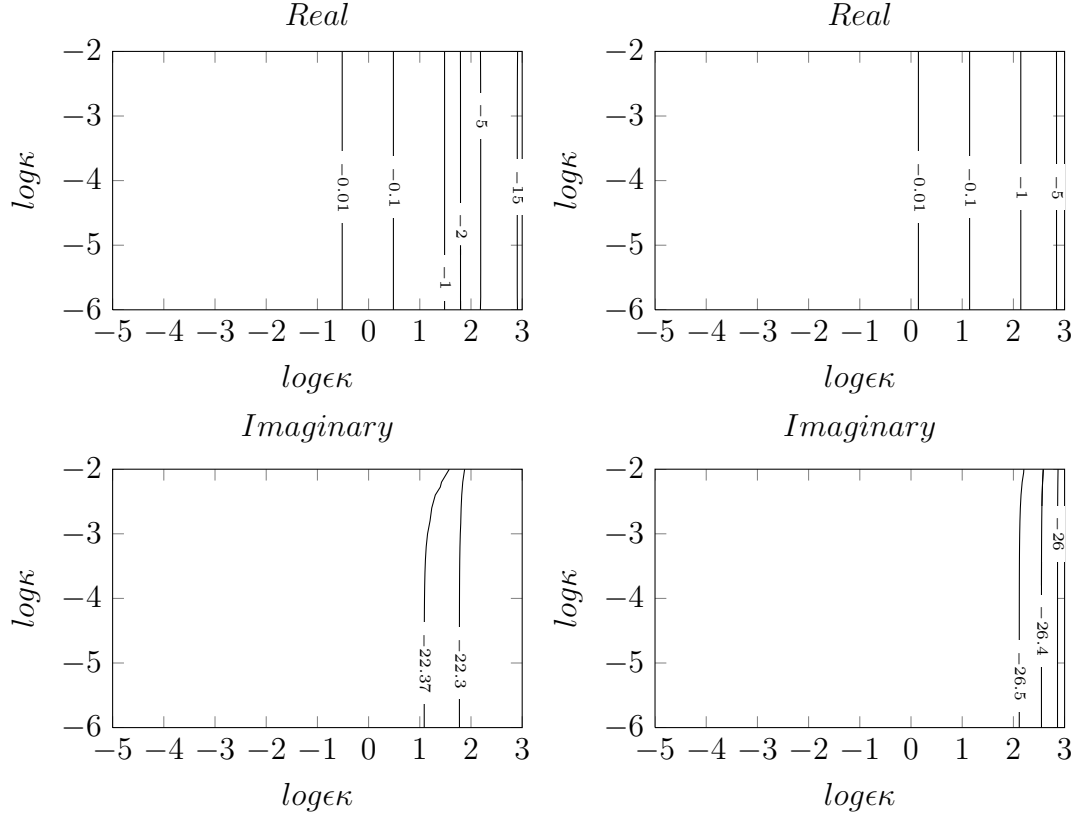


Figure A.3: Real and imaginary parts of the first and second eigenvalues for the rectangular CCFF plate

A.1.4 CFFF

The eigenvalues of the first two modes for the CFFF plate with closed-open-open-open (Neumann-Dirichlet-Dirichlet-Dirichlet) fluid boundary are presented at Tables A.7-A.8.

Table A.7

Damped eigenvalues for the first mode of square CFFF plate with closed-open-open-open boundary conditions (Vacuum : 3.4864)

$\log \epsilon \kappa$	$\log \kappa = -5$	-4	-3	-2
-5	3.52	3.52	3.52	3.52
-3	3.52	3.52	3.52	3.52
-1	3.52	3.52	3.52	3.52
1	$-0.13 \pm 3.51j$	$-0.13 \pm 3.51j$	$-0.13 \pm 3.51j$	$-0.13 \pm 3.51j$
2	$-1.33 \pm 3.27j$	$-1.33 \pm 3.27j$	$-1.33 \pm 3.27j$	$-1.33 \pm 3.28j$
3	$-0.47 \pm 0.00j$	$-0.47 \pm 0.00j$	$-0.47 \pm 0.00j$	$-0.47 \pm 0.00j$

Table A.8

Damped eigenvalues for the second mode of square FFFC plate with open-open-open-closed boundary conditions (Vacuum : 8.5443)

$\log \epsilon \kappa$	$\log \kappa = -5$	-4	-3	-2
-5	8.52	8.52	8.52	8.52
-3	8.52	8.52	8.52	8.52
-1	8.52	8.52	8.52	8.52
1	$-0.05 \pm 8.52j$	$-0.05 \pm 8.52j$	$-0.05 \pm 8.52j$	$-0.05 \pm 8.52j$
2	$-0.54 \pm 8.50j$	$-0.54 \pm 8.50j$	$-0.54 \pm 8.50j$	$-0.54 \pm 8.50j$
3	$-5.58 \pm 6.57j$	$-5.58 \pm 6.58j$	$-5.58 \pm 6.58j$	$-5.58 \pm 6.58j$

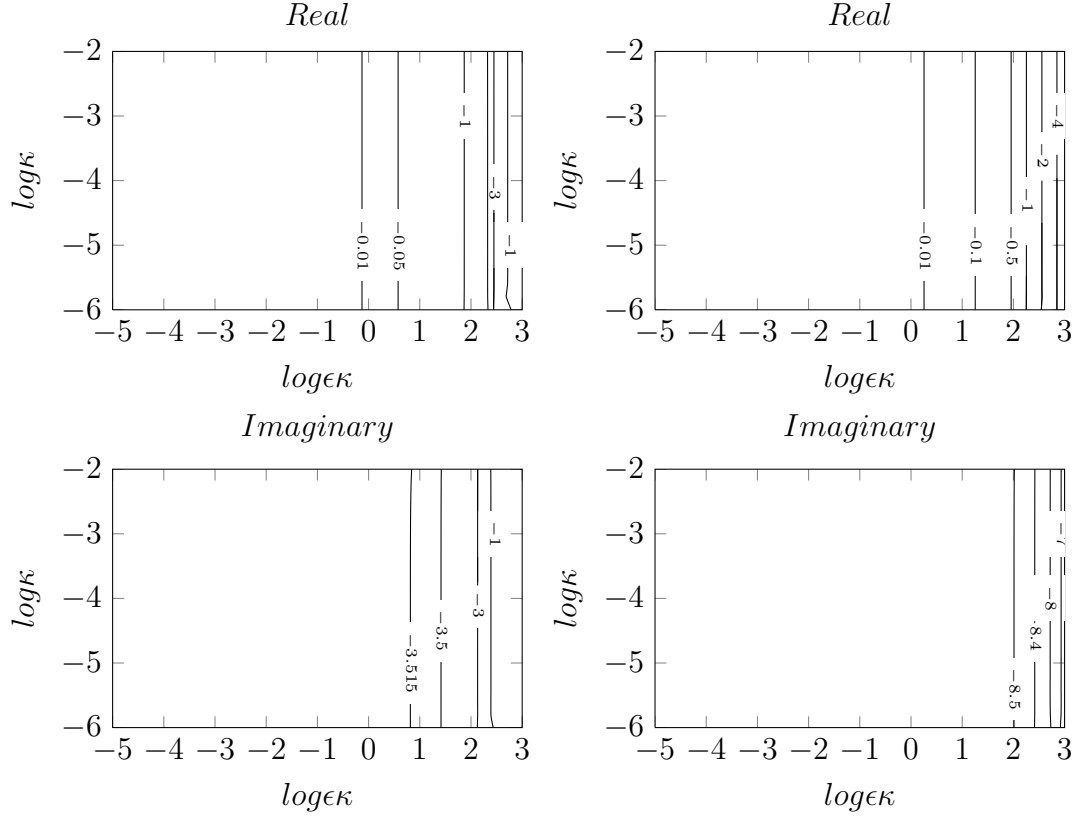


Figure A.4: Real and imaginary parts of the first and second eigenvalues for the rectangular CFFF plate

A.1.5 CFCF

The eigenvalues of the first two modes for the CFFF plate with closed-open-open-open (Neumann-Dirichlet-Dirichlet-Dirichlet) fluid boundary are presented at Tables A.9-A.10.

Table A.9

Damped eigenvalues for the first mode of square CCFF plate (Vacuum : 6.9365)

$\log \epsilon \kappa$	$\log \kappa = -5$	-4	-3	-2
-5	7.10	7.10	7.10	7.10
-3	7.10	7.10	7.10	7.10
-1	7.10	7.10	7.10	7.10
1	$-0.12 \pm 7.10j$	$-0.12 \pm 7.10j$	$-0.12 \pm 7.10j$	$-0.12 \pm 7.10j$
2	$-1.25 \pm 7.04j$	$-1.25 \pm 7.04j$	$-1.25 \pm 7.04j$	$-1.25 \pm 7.05j$
3	$-1.94 \pm 0.00j$	$-1.94 \pm 0.00j$	$-1.94 \pm 0.00j$	$-1.93 \pm 0.00j$

Table A.10

Damped eigenvalues for the second mode of square CCFF plate (Vacuum : 23.948)

$\log \epsilon \kappa$	$\log \kappa = -5$	-4	-3	-2
-5	24.83	24.83	24.83	24.83
-3	24.83	24.83	24.83	24.83
-1	24.83	24.83	24.83	24.83
1	$-0.02 \pm 24.82j$	$-0.02 \pm 24.82j$	$-0.02 \pm 24.82j$	$-0.02 \pm 24.82j$
2	$-0.49 \pm 24.69j$	$-0.49 \pm 24.69j$	$-0.49 \pm 24.69j$	$-0.49 \pm 24.69j$
3	$-5.74 \pm 24.18j$	$-5.74 \pm 24.18j$	$-5.74 \pm 24.18j$	$-5.75 \pm 24.21j$

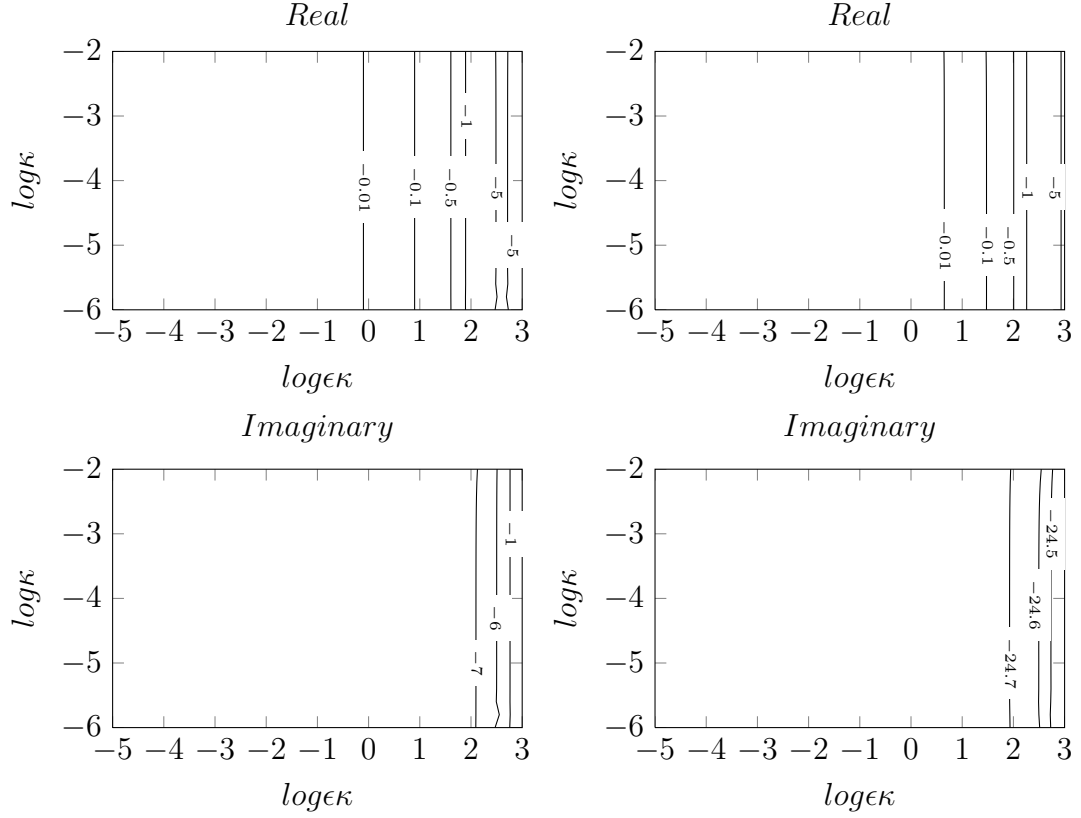


Figure A.5: Real and imaginary parts of the first and second eigenvalues for the rectangular CFCF plate

A.2 Gnu Octave Scripts

The following scripts are adapted from Ref. [78] which provides well-known thin plate stiffness and matrix calculations.

A.2.1 Fluid stiffness matrix \mathbf{K}_f calculation

The following Gnu Octave script can calculate and assemble the element matrices to form global fluid stiffness matrix.

```
function [K] = formFLUID_Kf (...
```



```

GDof,numberElements,elementNodes,numberNodes,nodeCoordinates,...
C_shear,C_bending,thickness,I)
% computation of stiffness matrix
% for quadrilateral fluid element
% K : stiffness matrix
K = spalloc(GDof,GDof,10*GDof);
% Gauss quadrature for bending part
[gaussWeights,gaussLocations] = gaussQuadrature('complete');
% cycle for element
for e = 1:numberElements
% indice : nodal condofectivities for each element
% elementDof: element degrees of freedom
indice = elementNodes(e,:);
elementDof = [indice];
ndof = length(indice);      % cycle for Gauss point
for q = 1:size(gaussWeights,1)
GaussPoint = gaussLocations(q,:);
xi = GaussPoint(1);
eta = GaussPoint(2);
% shape functions and derivatives
[shapeFunction,naturalDerivatives] = shapeFunctionQ4(xi,eta);
% Jacobian matrix, inverse of Jacobian,
% derivatives w.r.t. x,y
[Jacob,invJacobian,XYderivatives] = Jacobian(...
nodeCoordinates(indice,:),naturalDerivatives);
ke = XYderivatives(:,1)*XYderivatives(:,1)' + ...
XYderivatives(:,2)*XYderivatives(:,2)';
%stiffness matrix
K(elementDof,elementDof) = K(elementDof,elementDof)+ ...
ke*gaussWeights(q)*det(Jacob);
end % Gauss point
end % element
end

```

A.2.2 Fluid mass matrix M_f calculation

The following Gnu Octave script can calculate and assemble the element matrices to form global fluid mass matrix.

```
function [mass]=formFUID_Mf(...
GDof,numberElements,elementNodes,numberNodes,nodeCoordinates)
% computation of mass matrix
% for quadrilateral fluid element
% mass : mass matrix
mass = spalloc(GDof,GDof,10*GDof);
% Gauss quadrature
[gaussWeights,gaussLocations] = gaussQuadrature('complete');
% cycle for element
for e = 1:numberElements
% indice : nodal condofectivities for each element
indice = elementNodes(e,:);
ndof = length(indice);
% cycle for Gauss point
for q = 1:size(gaussWeights,1)
GaussPoint = gaussLocations(q,:);
xi = GaussPoint(1);
eta = GaussPoint(2);
% shape functions and derivatives
[shapeFunction,naturalDerivatives] = shapeFunctionQ4(xi,eta);
% Jacobian matrix, inverse of Jacobian,
% derivatives w.r.t. x,y
[Jacob,invJacobian,XYderivatives] = Jacobian(...
nodeCoordinates(indice,:),naturalDerivatives);
% mass matrix
mass(indice,indice) = mass(indice,indice) + ...
shapeFunction*shapeFunction'*gaussWeights(q)*det(Jacob);
end % Gauss point
end % element
end
```

A.2.3 Fluid forcing matrix Q_f calculation

The following Gnu Octave script can calculate and assemble the element matrices to form global fluid forcing matrix.

```
function [Qf] = formFLUID_Qf(GDof,numberElements,...
    elementNodes,numberNodes,nodeCoordinates)
% computation of fluid force coupling matrix
% for quadrilateral fluid element
Qf = spalloc(GDof,3*GDof,10*GDof);
% Gauss quadrature for bending part
[gaussWeights,gaussLocations] = gaussQuadrature('complete');
% cycle for element
for e = 1:numberElements
% indice : nodal condofectivities for each element
indice = elementNodes(e,:);
ndof = length(indice);
% cycle for Gauss point
for q = 1:size(gaussWeights,1)
GaussPoint = gaussLocations(q,:);
xi = GaussPoint(1);
eta = GaussPoint(2);
% shape functions and derivatives
[shapeFunction,naturalDerivatives] = shapeFunctionQ4(xi,eta);
% Jacobian matrix, inverse of Jacobian,
% derivatives w.r.t. x,y
[Jacob,invJacobian,XYderivatives] = Jacobian(...
    nodeCoordinates(indice,:),naturalDerivatives);
% Qf matrix
Qf(indice,indice) = Qf(indice,indice) + ...
    shapeFunction*shapeFunction'*gaussWeights(q)*det(Jacob);
Qf(indice,indice+numberNodes) = Qf(indice,indice+numberNodes) + ...
    shapeFunction*shapeFunction'*gaussWeights(q)*det(Jacob);
Qf(indice,indice+2*numberNodes) = Qf(indice,indice+2*numberNodes)+...
```

```

shapeFunction*shapeFunction'*gaussWeights(q)*det(Jacob);
end % Gauss point
end % element
end

```

A.2.4 Structural stiffness matrix K calculation

The following Gnu Octave script can calculate and assemble the element matrices to form global structural stiffness matrix.

```

function [K,KS] = formStruc_K(...
GDof,numberElements,elementNodes,numberNodes,...
nodeCoordinates,C_shear,C_bending,thickness,I)
% computation of stiffness matrix
% for Mindlin plate element
% K : stiffness matrix
% KS : stiffness matrix due to shear
K = spalloc(GDof,GDof,10*GDof);
KS = spalloc(GDof,GDof,10*GDof);
% Gauss quadrature for bending part
[gaussWeights,gaussLocations] = gaussQuadrature('complete');
% cycle for element
% cycle for element
for e = 1:numberElements
% indice : nodal connectivities for each element
% elementDof: element degrees of freedom
indice = elementNodes(e,:);
elementDof = [indice indice+numberNodes indice+2*numberNodes];
ndof = length(indice);
% cycle for Gauss point
for q = 1:size(gaussWeights,1)
GaussPoint = gaussLocations(q,:);
xi = GaussPoint(1);
eta = GaussPoint(2);

```

```

% shape functions and derivatives
[shapeFunction,naturalDerivatives] = shapeFunctionQ4(xi,eta);
% Jacobian matrix, inverse of Jacobian,
% derivatives w.r.t. x,y
[Jacob,invJacobian,XYderivatives] = ...
Jacobian(nodeCoordinates(indice,:),naturalDerivatives);
% [B] matrix bending
B_b = zeros(3,3*ndof);
B_b(1,ndof+1:2*ndof) = XYderivatives(:,1)';
B_b(2,2*ndof+1:3*ndof) = XYderivatives(:,2)';
B_b(3,ndof+1:2*ndof) = XYderivatives(:,2)';
B_b(3,2*ndof+1:3*ndof)= XYderivatives(:,1)';
% stiffness matrix bending
K(elementDof,elementDof) = K(elementDof,elementDof) + ...
B_b'*C_bending*B_b*gaussWeights(q)*det(Jacob);
end % Gauss point
end % element
% shear stiffness matrix
% Gauss quadrature for shear part
[gaussWeights,gaussLocations] = gaussQuadrature('reduced');
% cycle for element
% cycle for element
for e = 1:numberElements
% indice : nodal connectivities for each element
% elementDof: element degrees of freedom
indice = elementNodes(e,:);
elementDof = [indice indice+numberNodes indice+2*numberNodes];
ndof = length(indice);
% cycle for Gauss point
for q = 1:size(gaussWeights,1)
GaussPoint=gaussLocations(q,:);
xi = GaussPoint(1);
eta = GaussPoint(2);
% shape functions and derivatives

```

```

[shapeFunction,naturalDerivatives] = shapeFunctionQ4(xi,eta);
% Jacobian matrix, inverse of Jacobian,
% derivatives w.r.t. x,y
[Jacob,invJacobian,XYderivatives] = Jacobian(...
nodeCoordinates(indice,:),naturalDerivatives);
% [B] matrix shear
B_s = zeros(2,3*ndof);
B_s(1,1:ndof) = XYderivatives(:,1)';
B_s(2,1:ndof) = XYderivatives(:,2)';
B_s(1,ndof+1:2*ndof) = shapeFunction;
B_s(2,2*ndof+1:3*ndof) = shapeFunction;
% stiffness matrix shear
KS(elementDof,elementDof) = KS(elementDof,elementDof) + ...
B_s'*C_shear*B_s*gaussWeights(q)*det(Jacob);
end % gauss point
end % element
end

```

A.2.5 Structural mass matrix M calculation

The following Gnu Octave script can calculate and assemble the element matrices to form global structural mass matrix.

```

function [mass]=formStruc_M(GDof,numberElements,
elementNodes,numberNodes,nodeCoordinates,thickness,rho,I)
% computation of mass matrix
% for Mindlin plate element
% mass : mass matrix
mass = spalloc(GDof,GDof,10*GDof);
massshear = spalloc(GDof,GDof,10*GDof);
% Gauss quadrature for bending part
[gaussWeights,gaussLocations] = gaussQuadrature('complete');
% cycle for element
for e = 1:numberElements

```

```

% indice : nodal connectivities for each element
indice = elementNodes(e,:);
ndof = length(indice);
% cycle for Gauss point
for q = 1:size(gaussWeights,1)
GaussPoint = gaussLocations(q,:);
xi = GaussPoint(1);
eta = GaussPoint(2);
% shape functions and derivatives
[shapeFunction,naturalDerivatives] = shapeFunctionQ4(xi,eta);
% Jacobian matrix, inverse of Jacobian,
% derivatives w.r.t. x,y
[Jacob,invJacobian,XYderivatives] = Jacobian(...
nodeCoordinates(indice,:),naturalDerivatives);
mass(indice,indice) = mass(indice,indice) + ...
shapeFunction*shapeFunction'*gaussWeights(q)*det(Jacob);
massshear(indice+numberNodes,indice+numberNodes) = ...
massshear(indice+numberNodes,indice+numberNodes) + ...
shapeFunction*shapeFunction'*gaussWeights(q)*det(Jacob);
massshear(indice+2*numberNodes,indice+2*numberNodes) = ...
massshear(indice+2*numberNodes,indice+2*numberNodes) + ...
shapeFunction*shapeFunction'*gaussWeights(q)*det(Jacob);
end % Gauss point
end % element
mass = mass + massshear;
end

```

A.2.6 Structural forcing matrix Q calculation

The following Gnu Octave script can calculate and assemble the element matrices to form global structural forcing matrix.

```

function [Q] = formStruct_Q(...
GDof,numberElements,elementNodes,numberNodes,nodeCoordinates)

```

```

% computation of forcing matrix
% for Mindlin plate element
% Q : forcing matrix
Q = spalloc(3*GDof,GDof,10*GDof);
% Gauss quadrature for bending part
[gaussWeights,gaussLocations] = gaussQuadrature('complete');
% cycle for element
for e = 1:numberElements
% indice : nodal connectivities for each element
indice = elementNodes(e,:);
ndof = length(indice);
% cycle for Gauss point
for q = 1:size(gaussWeights,1)
GaussPoint = gaussLocations(q,:);
xi = GaussPoint(1);
eta = GaussPoint(2);
% shape functions and derivatives
[shapeFunction,naturalDerivatives] = shapeFunctionQ4(xi,eta);
% Jacobian matrix, inverse of Jacobian,
% derivatives w.r.t. x,y
[Jacob,invJacobian,XYderivatives] = Jacobian(...
nodeCoordinates(indice,:),naturalDerivatives);
% Q matrix
Q(indice,indice) = Q(indice,indice) + ...
shapeFunction*shapeFunction'*gaussWeights(q)*det(Jacob);
Q(indice+numberNodes,indice) = Q(indice+numberNodes,indice) + ...
shapeFunction*shapeFunction'*gaussWeights(q)*det(Jacob);
Q(indice+2*numberNodes,indice) = Q(indice+2*numberNodes,indice) + ...
shapeFunction*shapeFunction'*gaussWeights(q)*det(Jacob);
end % Gauss point
end % element
end

```


A.2.7 Eigen solution of coupled problem

The following Gnu Octave script can calculate the global coupled matrices and solve complex eigenvalue problem using ARPACK [79] eigenproblem solver.

```
function Damped = solveeig(KS,MS,KF,MF,...
G,U,E,thickness,rho,poisson)
% Solves and returns the nondimensional eigenvalues
% of the coupled problem

[m,n]=size(MS); % size of structural matrices
[mf,nf]=size(MF); %size of fluid matrices

% Converting the problem into
%  $MM*dX/dt = KK*X$ 

% global coupled dX/dt multiplier
MM = [MS zeros(m,n) zeros(m,nf);...
      zeros(m,n) eye(m,n) zeros(m,nf);...
      zeros(mf,n) zeros(mf,n) MF ];

% global coupled X multiplier
KK = [zeros(m,n) KS -G;...
      -eye(m,n) zeros(m,n) zeros(m,nf);...
      U zeros(mf,n) KF];

numberOfModes = 5;
% Solution for the first numberOfModes
% considering complex conjugates
[VV,DD] = eigs(KK,MM,2*numberOfModes,'sm');

% damped eigenvalues
damped = diag(DD);
```

```
% Converting into non-dimensional form
Damped = damped / (sqrt(E*thickness^3/(...
12*rho*thickness*(1-poisson^2)))/L^2) ;
```

A.3 Second harmonic nonlinear solution

A.3.1 Case CCCC

Considering

$$a_1(x, y) = \sum_{m=0}^2 \sum_{n=0}^2 c_{mn} \cos \frac{m\pi x}{L_x} \cos \frac{n\pi y}{L_y} \quad (\text{A.1})$$

and

$$a_2(x, y) = \sum_{m=0}^4 \sum_{n=0}^4 e_{mn} \cos \frac{m\pi x}{L_x} \cos \frac{n\pi y}{L_y} \quad (\text{A.2})$$

the second harmonic complex coefficients are

$$\begin{aligned} e_{00} &= -\frac{\delta}{4} (c_{22} - 2c_{20} - 2c_{02} + 4c_{00}) \\ e_{20} &= -\frac{(6\delta c_{20} + c_{02}c_{22} + 2c_{00}c_{20} - 2\delta c_{22})\pi^2}{i\sigma L_x^2} + \frac{\delta}{2} (c_{22} - 2c_{20} - c_{02} + 2c_{00}) \\ e_{40} &= \frac{-(3\delta c_{22} - 6\delta c_{20} + 2c_{20}^2 + c_{22}^2)\pi^2}{iL_x^2\sigma} + \frac{2c_{20} - c_{22}}{4}\delta \\ e_{02} &= -\frac{(-2c_{00} + c_{20} + 2c_{02} - c_{22})i\delta\sigma L_y^2 + 2(-3\delta c_{22} + c_{22}c_{20} + 2c_{00}c_{02} + 6\delta c_{02})\pi^2}{4\pi^2 + 2iL_y^2\sigma} \\ e_{04} &= \frac{(2c_{02} - c_{22})\frac{1}{4}i\sigma\delta L_y^2 + (6\delta c_{02} - 2c_{02}^2 - c_{22}^2 - 3\delta c_{22})\pi^2}{iL_y^2\sigma + 8\pi^2} \\ e_{22} &= -\frac{(c_{00} - c_{20} + c_{22} - c_{02})i\delta L_y^2\sigma + (c_{00}c_{22} + c_{02}c_{20} - 3\delta c_{20} + 3\delta c_{22})2\pi^2\left(\frac{L_y^2}{L_x^2} + 1\right)}{2\pi^2 + iL_y^2\sigma} \\ e_{42} &= -\frac{(c_{20} - c_{22})L_x^2L_y^2i\delta\sigma + (6\delta c_{20}L_y^2 - 6\delta c_{22}L_y^2 + 4c_{20}c_{22}L_y^2 + c_{20}c_{22}L_x^2 - 3\delta c_{22}L_x^2)2\pi^2}{2L_x^2(2\pi^2 + iL_y^2\sigma)} \\ e_{24} &= -\frac{(c_{02} - c_{22})L_x^2L_y^2i\delta\sigma + (c_{02}c_{22}L_y^2 - 3\delta c_{22}L_y^2 + 4c_{02}c_{22}L_x^2 - 6\delta c_{22}L_x^2 + 6\delta c_{02}L_x^2)2\pi^2}{2L_x^2(iL_y^2\sigma + 8\pi^2)} \\ e_{44} &= -c_{22} \frac{(c_{22}L_y^2 + 3\delta L_y^2 + c_{22}L_x^2 + 3\delta L_x^2)4\pi^2 + i\sigma\delta L_x^2L_y^2}{4L_x^2(iL_y^2\sigma + 8\pi^2)} \end{aligned} \quad (\text{A.3})$$

A.3.2 Case CFCC

Considering the first harmonic solution as

$$a_1(x, y) = \sum_m \left(c_m + d_m \cos \frac{2\pi y}{L_y} \right) \cos \frac{m\pi x}{2L_x} \quad (\text{A.4})$$

and the second harmonic,

$$a_2(x, y) = \sum_m \left(e_m + f_m \cos \frac{2\pi y}{L_y} + g_m \cos \frac{4\pi y}{L_y} \right) \cos \frac{m\pi x}{2L_x} \quad (\text{A.5})$$

the second harmonic coefficients are

$$e_m = \sum_n \frac{(1+8nm) \frac{i\sigma\delta}{4\pi} - \frac{3mn\pi\delta}{8L_x^2} (1-n^2-m^2)}{a(n\pm 1\pm m)} (d_m - 2c_m) + \frac{3\pi\delta mn}{32aL_x^2} (d_m - 2c_m) - \sum_n \frac{\pi m^2}{8aL_x^2 n} (2c_m^2 + d_m^2) \quad (\text{A.6})$$

where $a = \frac{-16\pi L_x^2}{m^2\pi^2 + 8iL_x^2\sigma}$,

$$(n \pm 1 \pm m) = (n+1+m)(n+1-m)(n-1+m)(n-1-m) \quad (\text{A.7})$$

and m, n are odd numbers.

$$f_m = b \sum_n \left\{ \left(\frac{1}{4}i\sigma + \frac{3\pi^2}{32L_x^2} m^2 \right) (c_m - d_m) - \frac{3\pi^2}{2L_y^2} d_m \right\} \delta(-1)^{\frac{m+1}{2}} - \frac{\frac{4}{L_y^2} + \frac{n}{4L_x^2}}{4m^2 - n^2} \pi m^2 c_m d_m + \frac{\left(\frac{3\pi}{8L_x^2} (m^2 - 1 + n^2) + \frac{2}{\pi} i\sigma \right) (c_m - d_m) - \frac{12\pi}{L_y^2} d_m}{(m \pm 1 \pm n)} mn\delta \quad (\text{A.8})$$

where $b = \frac{-32L_x^2 L_y^2}{8i\sigma L_x^2 L_y^2 + m^2\pi^2 L_y^2 + 16\pi^2 L_x^2}$.

$$h_m = c \sum_n \left(\frac{1}{8} i\sigma + \frac{3\pi^2}{2L_y^2} + \frac{3\pi^2}{64L_x^2} m^2 \right) \delta(-1)^{\frac{m+1}{2}} d_m - \frac{\frac{n^2+4m^2}{16L_x^2} + \frac{4}{L_y^2}}{n(4m^2-n^2)} m^2 \pi d_m^2 + \frac{\frac{i\sigma}{\pi} + \frac{3\pi}{16L_x^2} (n^2+m^2-1) + \frac{12\pi}{L_y^2}}{(m \pm 1 \pm n)} mn \delta d_m \quad (\text{A.9})$$

$$\text{where } c = \frac{-32L_x^2 L_y^2}{8i\sigma L_x^2 L_y^2 + m^2 \pi^2 L_y^2 + 64\pi^2 L_x^2}$$

A.3.3 Case FCFC

Considering the first harmonic solution as

$$a_1(x, y) = \sum_m \left(c_m + d_m \cos \frac{2\pi x}{L_x} \right) \sin \frac{m\pi y}{L_y} \quad (\text{A.10})$$

and the second harmonic,

$$a_2(x, y) = \sum_m \left(e_m + f_m \cos \frac{2\pi x}{L_x} + h_m \cos \frac{4\pi x}{L_x} \right) \sin \frac{m\pi y}{L_y} \quad (\text{A.11})$$

the coefficients of the second harmonic can be found as

$$e_m = a \left\{ i\sigma + \frac{3\pi^2}{2L_y^2} m^2 \right\} \delta(d_m - 2c_m) - a \sum_{n,g} \frac{(d_g d_n - 2c_g c_n) + c_n (g^2 + n^2 - m^2) (c_g + \frac{1}{2} d_g)}{(n \pm g \pm m)} \frac{\pi}{L_y^2} gmn \quad (\text{A.12})$$

where $a = \frac{L_y^2}{(2i\sigma L_y^2 + m^2 \pi^2)}$ and n, g are odd numbers.

$$f_m = b \left(2i\sigma + \frac{3}{L_y^2} m^2 \pi^2 \right) \delta(d_m - c_m) + \frac{12b}{L_x^2} \pi^2 \delta d_m + 8b\pi \sum_{n,g} \frac{\frac{1}{2L_y^2} (g^2 + n^2 - m^2) c_g d_n - 2(g^2 + n^2) - \frac{4}{L_x^2} c_g d_n}{(n \pm g \pm m)} gmn \quad (\text{A.13})$$

where $b = \frac{L_x^2 L_y^2}{(2i\sigma L_x^2 L_y^2 + 4\pi^2 L_y^2 + m^2 \pi^2 L_x^2)}$

$$h_m = c \left(i\sigma + \frac{12}{L_x^2} \pi^2 + \frac{3m^2}{2L_y^2} \pi^2 \right) \delta d_m - 2c\pi \sum_{n,g} \frac{\frac{1}{L_y^2} (g^2 + n^2 - m^2) - \left(\frac{16}{L_x^2} + \frac{2}{L_y^2} \right)}{(n \pm g \pm m)} g m n d_g d_n \quad (\text{A.14})$$

where $c = \frac{L_x^2 L_y^2}{2i\sigma L_x^2 L_y^2 + 16\pi^2 L_y^2 + m^2 \pi^2 L_x^2}$

A.3.4 Case FSFS

Considering the first harmonic solution as

$$a_1(x, y) = \sum_m \sum_n c_{mn} \cos \frac{m\pi x}{L_x} \sin \frac{n\pi y}{L_y} \quad (\text{A.15})$$

and the second harmonic solution,

$$a_2(x, y) = \sum_r \sum_s d_{rs} \cos \frac{r\pi x}{L_x} \sin \frac{s\pi y}{L_y} \quad (\text{A.16})$$

the coefficients of the infinite series can be found as

$$d_{rs} = \sum_a d_{rs}^{(a)} \quad (\text{A.17})$$

where

$$\begin{aligned}
d_{rs}^{(1)} &= \frac{\pi}{L_x^2} \sum_{m,n,g,h} \frac{4m^2ng^2hrsc_{mn}c_{gh}}{(s\pm n\pm h)(r\pm m\pm g)} \\
d_{rs}^{(2)} &= 3\delta \frac{\pi}{L_x^2} \sum_{m,n} \frac{m^2c_{mn}(r^2+1-m^2)}{(n+s)(r\pm m\pm 1)} \\
d_{rs}^{(3)} &= 3\delta \sum_{m,n} \frac{m^2c_{mn}(1-r^2-m^2)}{\pi(n+s)(\pm r+m\pm 1)} \\
d_{rs}^{(4)} &= -\frac{\pi^2}{L_x^2} \sum_{m,n,g,h} \frac{2rgmnhs g^2 c_{mn}c_{gh}}{(\pm s+n\pm h)(\pm r+m\pm g)} \\
d_{rs}^{(5)} &= \frac{3\delta}{L_y^2} \sum_{m,n,g,h} \frac{-ngshc_{mn}c_{gh}(s^2-h^2-n^2)(m^2+r^2-g^2)}{(s\pm n\pm h)(r\pm m\pm g)} \\
d_{rs}^{(6)} &= 3\delta \frac{\pi}{L_y^2} \sum_{m,n} \frac{n^2c_{mn}(+m^2+r^2-1)}{(n+s)(\pm r\pm 1+m)} \\
d_{rs}^{(7)} &= -\frac{\pi^2}{L_y^2} \sum_{m,n,g,h} \frac{-2c_{mn}h^2c_{gh}(nhs)(m)}{(s\pm n\pm h)(r\pm m+g)} \\
d_{rs}^{(8)} &= -2j\sigma\delta \sum_{m,n} \frac{-c_{mn}(-1+m^2+r^2)}{\pi(n+s)(r\pm 1\pm m)}
\end{aligned} \tag{A.18}$$

and m, g, r are even numbers, n, h, s are odd numbers.

A.3.5 Case CFFC

Considering the first harmonic solution as

$$a_1(x, y) = \sum_m \sum_n c_{mn} \cos \frac{m\pi x}{2L_x} \cos \frac{n\pi y}{2L_y} \tag{A.19}$$

and the second harmonic solution,

$$a_2(x, y) = \sum_r \sum_s d_{rs} \cos \frac{r\pi x}{2L_x} \cos \frac{s\pi y}{2L_y} \tag{A.20}$$

the coefficients of the infinite series can be found as $d_{rs} = \sum_a d_{rs}^{(a)}$

where

$$\begin{aligned}
d_{rs}^{(1)} &= \sum_{m,n,g,h} \frac{mnghrsc_{mn}c_{gh} \left(\frac{m^2-g^2-r^2}{L_x^2} + \frac{n^2-h^2-s^2}{L_y^2} \right)}{(\pm s+n\pm h)(\pm r+m\pm g)} (-1)^{\frac{s+n+h+r+m+g-6}{2}} \\
d_{rs}^{(2)} &= -3\delta \sum_{m,n} \frac{mnrrsc_{mn}(-1)^{\frac{m+n+r+s-4}{2}}}{(\pm 1+n\pm s)(\pm r+m\pm 1)} \left(\frac{1+m^2-r^2}{L_x^2} + \frac{1+n^2-s^2}{L_y^2} \right) \\
d_{rs}^{(3)} &= -\frac{3\pi\delta}{4L_x^2} \sum_{m,n} \frac{mnrc_{mn}(1+m^2-r^2)(-1)^{\frac{m+r+n-3}{2}}}{(n+s)(\pm r+m\pm 1)} \\
d_{rs}^{(4)} &= -\frac{3\pi\delta}{4L_y^2} \sum_{m,n} \frac{mnsc_{mn}(n^2+1-s^2)(-1)^{\frac{s+n+m-3}{2}}}{(m+r)(\pm s\pm 1+n)} \\
d_{rs}^{(5)} &= -\frac{3\delta}{4L_x^2} \sum_{m,n} \frac{4mn(m^2+n^2)c_{mn}(-1)^{\frac{m+n+s-3}{2}}}{(\pm 1\pm m+r)(\pm 1+n\pm s)} \left(\frac{s}{m+r} + \frac{r}{n+s} \right) \\
d_{rs}^{(6)} &= -\sum_{m,n} \frac{mn\delta \left(\frac{2j\sigma}{\pi} + \frac{3\pi}{4L_x^2} (m^2+n^2) \right) c_{mn}(-1)^{\frac{m+n-2}{2}}}{(m+r)(n+s)} \left(\frac{1}{\pm 1\pm m+r} + \frac{1}{\pm 1\pm s+n} \right) \\
d_{rs}^{(7)} &= 8j\sigma\delta \sum_{m,n} \frac{mnc_{mn}(-1)^{\frac{r+m-2}{2}}}{\pi^2(\pm 1\pm s+n)(\pm 1\pm r+m)} \left(\frac{r}{s+n} + \frac{s}{m+r} \right)
\end{aligned} \tag{A.21}$$

and m, n, r, s are odd numbers.

A.3.6 Case FFFC

Considering the first harmonic solution as

$$a_1(x, y) = \sum_m \sum_n c_{mn} \cos \frac{m\pi x}{2L_x} \sin \frac{n\pi y}{L_y} \tag{A.22}$$

and the second harmonic solution,

$$a_2(x, y) = \sum_r \sum_s d_{rs} \cos \frac{r\pi x}{2L_x} \sin \frac{s\pi y}{L_y} \tag{A.23}$$

the coefficients of the infinite series can be found as $d_{rs} = \sum_a d_{rs}^{(a)}$

where

$$\begin{aligned}
d_{rs}^{(1)} &= \frac{1}{L_x^2} \sum_{m,n,g,h} \frac{mnghrsc_{mn}c_{gh}(m^2-r^2-g^2)}{(\pm s+n\pm h)(r\pm m\pm g)} (-1)^{\frac{r+m+g-3}{2}} \\
d_{rs}^{(2)} &= \frac{2}{L_y^2} \sum_{m,n,g,h} \frac{nhrsc_{mn}c_{gh}(n^2+h^2-s^2)(m^2+g^2-r^2)}{(\pm s+n\pm h)(\pm r+m\pm g)} (-1)^{\frac{r+m+g-3}{2}} \\
d_{rs}^{(3)} &= -\frac{8}{L_y^2} \sum_{m,n,g,h} \frac{mn^3ghrsc_{mn}c_{gh}}{(s\pm n\pm h)(\pm r\pm m\pm g)} (-1)^{\frac{r+m+g-3}{2}} \\
d_{rs}^{(4)} &= 3\delta \frac{\pi}{4L_x^2} \sum_{m,n} \frac{mrc_{mn}(m^2+1-r^2)}{(\pm r\pm 1+m)(n+s)} \\
d_{rs}^{(5)} &= -3\delta \frac{\pi^2}{4L_x^2} \sum_{m,n} \frac{2r(m+r)+(\pm 1+m\pm r)}{\pi(m+r)(n+s)(\pm 1+m\pm r)} sm^3c_{mn} (-1)^{\frac{m+r-2}{2}} \\
d_{rs}^{(6)} &= -3\delta \frac{\pi^2}{L_y^2} \sum_{m,n} \frac{(\pm 1+m\pm r)\frac{\pi}{2}+2m(m+r)(-1)^{\frac{m+r-2}{2}}}{\pi(m+r)(n+s)(\pm 1+m\pm r)} n^2rsc_{mn} \\
d_{rs}^{(7)} &= -2j\sigma\delta \sum_{m,n} \frac{2r(m+r)+(\pm 1+m\pm r)\frac{\pi}{2}}{\pi(m+r)(n+s)(\pm 1+m\pm r)} smc_{mn} (-1)^{\frac{r+m-2}{2}}
\end{aligned} \tag{A.24}$$

and m, n, g, h, r, s are odd numbers.

A.4 Thermal conductivities

Table A.11
Thermal conductivities of several materials

Materials	Thermal conductivity W/mK	Normalized Thermal conductivity w.r.t Air Air (20°C)
Air (0°C)	0.024	0.96
Air (20°C)	0.025	1.0
Air (40°C)	0.0262	1.0480
Aluminium, pure	205 - 237	8200 - 9480
Bronze	42 - 50	1680 - 2000
Copper, pure	353.1 - 386.0	14124 - 15440
Glass	0.8 - 0.93	32 - 37.2
Iron, pure	71.8 - 80.4	2872 - 3216
Lead, pure	34.7 - 35.3	1388 - 1412
Plastic, fiber-reinforced	0.23 - 1.06	9.2 - 42.4
Polymer, High-Density	0.33 - 0.52	13.2 - 20.8
Polymer, Low-density	0.04 - 0.33	1.6 - 13.2
Rubber (92%)	0.16	6.4
Silicon dioxide, pure	1	40
Stainless steel	16.3	652
Steel(normal)	50.2	2008
Titanium Alloy	5.8	224